ROMA TRE
UNIVERSITÀ DEGLI STUDI

Reduced-order wake inflow models for rotors in ground-effect

Dipartimento di Ingegneria

Dottorato di Ricerca in Ingegneria Meccanica ed Industriale – XXXII Ciclo

Candidate

Claudio Pasquali

Thesis Advisor

Prof. Massimo Gennaretti

Coordinator

Prof. Edoardo Bemporad

November 2019

Thesis not yet defended

Reduced-order wake inflow models for rotors in ground-effect
Ph.D. thesis. University Roma Tre

This thesis has been typeset by LaTeX .

Author's email: claudio.pasquali@uniroma3.it | pasquali.cl@gmail.com

Acknowledgments

This research was performed within the Roma Tre University participation in the University of Maryland/U.S.Naval Academy Vertical Lift Research Center of Excellence.

Contents

"Ci sono due tipi di problemi nella vita. Quelli senza soluzione e quindi è inutile preoccuparsi e quelli che una soluzione ce l'hanno e quindi è inutile preoccuparsi."

Chapter 1

Introduction

Helicopter operations frequently require long duration hovering flight over inclined or moving surfaces (for instance, over hillsides or ship decks) or, more generally, low-altitude, near-ground flight. Naval operations, in particular, are among the most dangerous duties that an helicopter may fulfill [1], as proven by several accident reports [2, 3]. Especially, landing over a fixed platform or a moving deck represent severe threats to airworthiness. This is due to several factors including the relatively small size of the flight deck, strong atmospheric wind and wind shear, turbulence due to the wake released by ship or platform superstructures, as well as deck roll, pitch and heave motion induced by waves.

Moving from pioneering works published during 1970-1980 decade [4, 5], analysis and control of such a complex problem [6, 7, 8, 9], as well as development of dedicated avionics and ship design [10, 11], are now receiving growing interest, thanks to the improvement in helicopter comprehensive simulation tools. This should lead to extending Ship-Helicopter Operating Limits (SHOLs), with advantages in terms of safety.

Nonetheless, the determination of the ship deck effects on landing helicopter dynamics is still one of the open and most challenging modeling problems. In principle, these may be divided into two main categories: those deriving from the impingement of turbulent flow generated by the ship superstructure during motion, and those deriving from the presence of the deck below the vehicle that alters the rotor wake dynamics (and particularly, the corresponding rotor wake inflow) through the so-called ground effect[1].

On first approximation, ship's air-wake turbulence and helicopter rotor downwash effects may be superimposed (thus neglecting coupling phenomena). The estimation of the ship turbulent air-wake effect on the helicopter dynamics could be accom-

[1] Note that, helicopter capability to hovering makes near-ground operations not limited to ship landing and take off, but also includes other tasks, like search and rescue operations (SAR).

plished either through a control equivalent turbulence input approach, when suited experimental flight data are available (see, for instance, Ref. [12]), or taking advantage of dedicated numerical simulations of the flow-field of ship's air-wake shed from the superstructure (see, for instance Refs. [13, 14, 15] where some methods for air-wake-downwash turbulence modelling are proposed, starting from suitable CFD databases). Instead, the effects of the presence of the deck in flight dynamics simulations may be suitably considered by including its influence on the rotor dynamic wake inflow model to be used in the blade aerodynamic loads formulation, for instance, such models could be also conveniently applied in other critical helicopter flight conditions, like low level flight or takeoff/landing on a slope. Among these, the adaptation of the well-known Peters [16] and He's [17] dynamic inflow model including the effect of a surface below the rotor has been proposed by including a specular pressure perturbation represented by a mirrored rotor with respect to the ground, [18, 19, 20, 21, 22]. These approaches are of particular interest for the rotorcraft manufacturer/research community in that, due to their simplicity and reduced computational effort, the use of dynamic inflow models coupled with two-dimensional airfoil aerodynamics still remains a widely-used approach. Despite the aforementioned advantages, these models suffers from the accuracy limitations of analytical or semi-analytical models, that may be particularly critical when dealing with complex interaction phenomena or non-conventional operating conditions. Hence, accurate dynamic inflow models are required in order to have the support of computationally efficient and, at the same time, reliable simulations of the complex aerodynamic environment in which rotors operate. Recently, a lot of research activities have dealt with the development of simulation-based dynamic inflow models for maneuvering helicopter rotors in open air (isolated), [23, 24, 25], as well as for ground case, [26, 27]. The accurate evaluation of in-ground-effect dynamic inflow for arbitrary flight conditions is a very challenging task that requires the support of high-fidelity numerical aerodynamic tools (particularly, when finite-dimension and moving ship decks are considered). However, a prerequisite to developing flight dynamics models under these operational conditions is the understanding of the complex fluid dynamics of the problem, which is particularly affected by the wake shape evolution in proximity of the ground (like in all those situations -BVI, ground effect, near obstacle- when the wake directly impacts with bodies). The effect of ground presence on rotor/helicopter aerodynamics, has been studied by several authors in the past decades, starting with the pioneering experimental work of Wiesner and Kohler [28], Yeager, Young and Mantay [29] and that of Empey and Ormiston [30], that was followed by the studies presented by Curtiss et al. [31], Hanker and Smith [32], Cimbala et al. [33], Light [34] and in the recent years also by Milluzzo [35].

Hence, rotor wake modeling is clearly one of the most challenging tasks in rotor aerodynamic numerical applications, in particular for the simulation of ground effect. Due to the complexity of the problem, in order to well capture the wake deformation dynamics, a lot of free-wake algorithms have been implemented with several different solution strategies, [36, 37, 38]. More recently, the problem of the ground effect has been examined also through dedicated numerical models [39, 40, 41] and validated with experimental data [42].
Focusing the attention on rotor configurations in ground effect (IGE), the objective of this thesis is twofold: development of an efficient high-fidelity aerodynamic solver, followed by the definition of a state-space dynamic inflow modelling technique that, based on the high-fidelity aerodynamic simulation tool, is capable of taking into account arbitrary rotor-ground relative kinematics. This work is part of University Roma Tre activity as partner of the University of Maryland/U.S. Naval Academy Vertical Lift Rotorcraft Center of Excellence (VLRCOE) [43].

1.1 The steady IGE aerodynamic problem

The ground effect problem is one of the most important wake-obstacle-interference problems in rotor aerodynamics, hence for the helicopter community. Under an engineering point of view the main effect of the phenomena related to this interaction are those regarding the increased thrust for a given (induced) power, conversely the reduced (induced) power for a specific thrust production. Quantitative effects of the ground on helicopter hovering performance are depicted in figure 1.1, where the thrust augmentation is given as a function of the non-dimensional rotor height from the ground itself. In particular it has been found that the induced power reduction is much more evident than the corresponding total power, [44], the viscous drag can not be indeed influenced by ground presence. Recalling that the relationship between thrust and torque involves the axial induced velocity resulting from the momentum conservation law on the rotor disc, the effect of ground has to be due to a reduction in the averaged induced velocity, hence to a reduction in the inflow local angle as discussed by Prouty in [45].

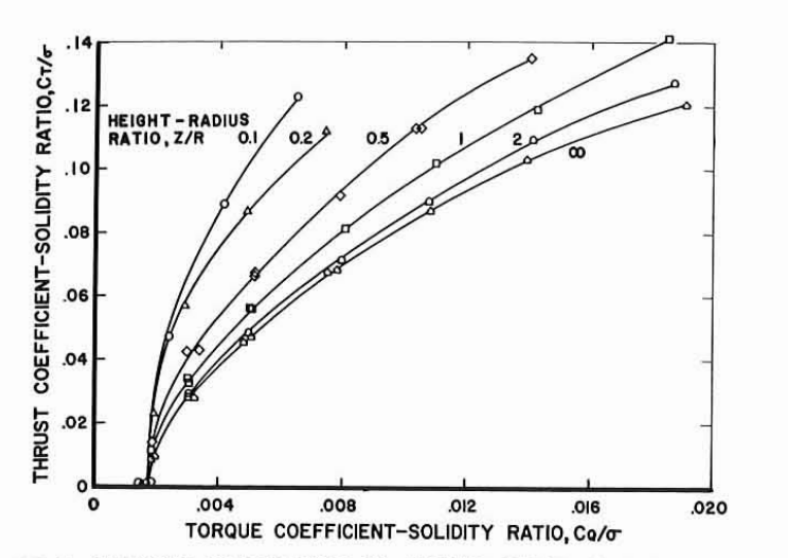

Figure 1.1. Ground effect on helicopter performance: thrust coefficient (C_T) as function of torque coefficient (C_Q), made dimension-less with the rotor solidity (σ), for different rotor heights from the ground, [46].

A deep comprehension of the aerodynamics of the problem is not yet full-filled. Experimental works carried out in the past exploited smoke visualization, [46], and shadow-graph technique, [34], trying to correlate the performance effects with the variation in the flow-field surrounding the rotor. Different heights from the ground and different disk load condition were analyzed and the tip vortex position measured, these characterizations of the flow-field between rotor and ground have shown that it is defined by two regions. The inner part (close to the rotation axis) has a very low-velocity air extending from the ground upward to a point above the rotor depending on the distance between rotor and ground. As proven by Milluzzo in recent years [35], also the relative angle between the disc plane and the ground has a considerable influence on this low-velocity region. Indeed, it determines the afore-mentioned region shape and position strongly enough to make, in the case of high inclination angle, this confined to a very small region in the neighborhood of the rotor hub (as it will be shown in chapter 3). Generally, the recirculation zone in the inner part, described above, causes the occurrence of an annular jet of high-velocity curved flow going outward from the rotation axis. These modifications in the wake shape change the relative vortex-blade position, hence the wake induced velocity (wake inflow), leading in particular to a reduction of the inflow as the rotor comes close to ground. Enlarging the analysis of this particular but common flight condition, characterized by the complex interaction between, rotor, rotor-wake and ground, the real nature of the problem clearly appears: a highly-unsteady, three-dimensional aerodynamic problem which affects not only the static or quasi-static performance of the machine

but also its handling qualities.
Nowadays, due to the continuous improvement of the computational available resources, the numerical simulations of such problems are seeing a growing interest. Different aerodynamic solvers were developed exploiting different analytical approaches. CFD solvers were validated against experimental data showing a good accordance both in the flow-field prediction and in performance evaluation [42] and [47], nevertheless to obtain a good accuracy a considerable computational effort is required. The calculations performed in [47], for instance, are carried out with a RANS-CFD[2] solver which required more than eleven hours wall clock time to evaluate one rotor revolution.
More computationally efficient aerodynamics solvers based on various vortex-method applications were successfully compared with experimental data in [41], [48] and [49]. The crucial issue in the simulation of ground-wake interaction is demonstrated to be the enforcing of the impermeability condition at the ground surface and, hence, the correct wake shape evaluation. In [49] it is believed that having the no-slip and non-penetration boundary conditions is critical for the simulation of rotorcraft wake near the ground and the obstacle. Therefore, a viscous boundary model, suitable for complex geometries, such as ground and buildings, was developed by considering the no-slip and non-penetration boundary conditions based on a vorticity sheet concept. Boundary Element Method (BEM) aerodynamic solver based on potential flows theory are also particularly suitable for free-wake rotor aerodynamic simulations, [50, 51]. They generally do not require huge computational resources and are easily extendible to ground effect simulations. In [38] a free-wake panel method is validated against experimental data of a helicopter hovering over a ground-obstacle with good accuracy, the ground was modelled by a mirror boundary condition in order to ensure the impermeability condition at ground surface.

1.2 Dynamic wake inflow

One of the most fundamental factors affecting the performance of rotorcraft systems is the induced influence of the main rotor wake on rotor air-loads and related performance. It is well known that the induced-flow field associated with a lifting rotor responds in a dynamic fashion to changes in either blade pitch (*i.e., pilot inputs*) or rotor flapping angles (*i.e., rotor or body dynamics*), thus severely influences the helicopter dynamic attitude and response. In figure 1.2 a sketch of a widely used helicopter aerodynamic-structural-dynamic loop is presented, the intrinsic coupling and complexity of the problem is clearly shown, as well as the

[2] Reynolds-averaged Navier-Stokes equation based aerodynamic solver.

importance of a correct simulation of the wake induced inflow dynamic for a realistic prediction of the helicopter response.
The ability of a flight simulator to accurately predict the behavior of an helicopter using information only from its physical characteristics would be highly desirable as it would allow manufacturers to get an early feedback from pilots on any design decision (concerning, for instance, handling qualities, rotorcraft-pilot coupling proneness, etc.). However, despite the complexity and the accuracy reached by the modules in modern simulators, they are not yet able to provide a fully coherent representation of reality. Moreover, with the aim of correcting some sub-optimal behavior in specific flight conditions and to respect the tolerances needed for the validation of a flight model, a certain amount of artificial tuning is often applied on top of the physical model. These modifications are often not justified from an engineering or physical standpoint and, while improving simulations for particular operating conditions, they may have an adverse effect on other parts of the flight envelope. The need to tune the model can often be related to the deficiencies of the mathematical model describing the helicopter dynamics.

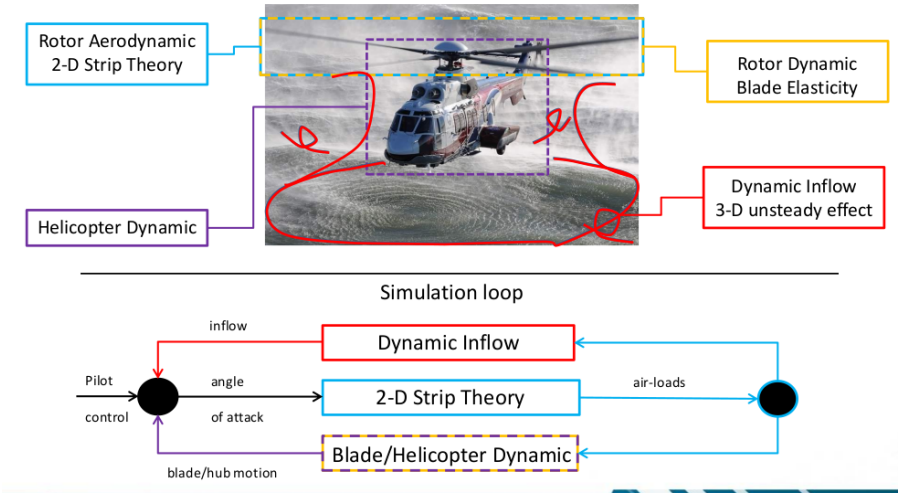

Figure 1.2. Helicopter comprehensive simulation tool main ingredients, sketch of the solution loop.

The physics involved is indeed the result of the coupling of complex phenomena like the nonlinear structural dynamics of the slender main rotor blades, the complex rotor aerodynamic environment resulting from the combination of blade motion and inflow induced by wake vorticity remaining in close proximity of the rotor disk, the interaction of the air flow with the fuselage, the main and tail rotors mutual interactions, the interaction with ground and surrounding obstacles, the dynamics of

engine and actuators, the effects of control systems. Obviously, real-time simulation of these phenomena requires a suitable trade-off between modeling accuracy and computational efficiency.

In this context the wake inflow dynamics, which would represent a surrogate of the wake three-dimensional unsteady effect over the blade, is a crucial element for an accurate and computational efficient helicopter simulation tool. In the past four decades, starting from the pioneeristic work of Pitt and Peters [16, 52], who presented an analytical simplified model relating a linear approximation of the velocity induced by the wake over the rotor disk with thrust, pitch and roll aerodynamic force and moments in a first-order time differential system, the knowledge and simulation capability of the problem has been strongly improved. Correlations between experimental flight data and simulations allowed an in-depth comparison which has shown limits and peculiarities of this simplified model: suited for flight dynamics applications (*i.e., low-frequency range of interest*) the Pitt-Peters model fails in the wake inflow frequency spectrum reconstruction for the frequencies involved in rotor aeroelasticity problem. Thus, a more complex models has been proposed considering more accurate description of the spatial distribution of the inflow over the rotor disk as well as a different and more accurate approximation of the pressure field over the disk, hence of the aerodynamic loads, [53, 54, 55]. Namely, the Peters-He generalized wake theory, which is a model that (starting from the three-dimensional potential flows equations) includes all the harmonics and all the radial distribution of inflow at arbitrary wake skew angle. It is a closed form theory, easy to implement and the correlation with experimental flight data has shown a very good agreement [56]. In addition, it is worth noting that the Peters-He model contains the Pitt model as a special simplified case.

Nevertheless all these models, directly derived from the physics governing law, are blind to the wake distortion effects. Indeed, it is well recognized that the wake distortion effects are the primary source of the off-axis response behaviour observed in maneuvering flight as well as in all those cases when the helicopter is operating near the ground or near generic obstacles. To improve the prediction of the effect of wake distortion in dynamic inflow model, a lot of work has been done, considering the mean distortion of the whole wake as adjunctive variables (*i.e., skew angle, wake curvature, wake distortion*), some corrective terms have been added to the original model, [57, 58], and their accuracy has been validated against experimental flight data, furthermore Prasad [59] has developed a dynamic model considering the wake distortion variables as adjunctive states for the system, hence characterized by their own first order dynamics with time.

Nowadays, advanced aerodynamic computational tools such as free-wake models and computational fluid dynamics, (CFD)-based numerical procedures are widely

used for detailed modeling and accurate prediction of the flow fields around generic rotary-wing configurations in various flight regimes. While such modern tools include fewer theoretical limitations and approximations than the classical and simplified schemes, especially CFD ones, they are impractical or impossible to be directly applied to many simulation tasks and flight dynamics problems, as they are not formulated in a state-space form and are often computationally intensive. However, starting from aerodynamic high-fidelity simulation, low-order inflow models could be extracted. Different methodologies, that will be capable of utilizing the accuracy provided by advanced tools to improve linear inflow models and subsequently provide more realistic flight dynamics calculations, have been developed from vortex lattice solvers, [26, 27, 60], or from BEM solvers, (Boundary Element Method), [23, 61]. All these simulation-based models have to simulate first a steady flight condition, then after arbitrary perturbation of the desired variables (in [26] the aerodynamic loads whereas in [23] directly the pilot input variables are perturbed) the relative perturbed inflow numerically evaluated by the aerodynamic high-fidelity solver and lastly the corresponding linear state-space models are identified. Moreover, the application of a three-dimensional complete aerodynamic solver allows the capability to predict rotor-induced inflow velocities away from the rotor, which is important for the calculation of aerodynamic interference effects at aircraft components such as the fuselage, wing, tail rotor, and empennage surfaces.

1.3 Thesis structure and novel contributions

Firstly, the extension to the ground simulation of the Boundary Element Method potential-based aerodynamic solver here applied and presented in chapter 2 is performed. The principal issue to be solved is the numerical imposition of the impermeability condition at the ground surface, two different techniques are implemented and compared. The computational efficiency of the algorithm is improved through the introduction of a novel wake structure allowing for a considerable reduction in the number of calculations required to evaluate the flow-field and, hence of the pressure-field, over the rotor blades (as it will be shown in section 2.2). The proposed solutions for the aerodynamic simulations of the ground effect condition are then compared and validated with experimental data proving their accuracy, specifically the capability to exploit this solver to simulate the wake inflow due to arbitrary input perturbation is proven. A deep comparison between experimental data and numerical predictions of the performance and of the flow-field in the whole wake region of rotors operating in ground effect has been carried out. Furthermore, ground surface not parallel to rotor disc has been considered in the analysis characterizing

also this extreme but common flight condition.
Thus, starting from the dynamic inflow model identification procedures recently developed for out-of-ground-effect analysis [23, 62, 63] the identification of a state-space representation of the wake inflow dynamics of an hovering rotor in ground effect is proposed. The complexity of the problem and the numerical instabilities those arise when part of the wake is re-ingested by rotor disk (due to the ground presence) have required the definition of a new identification technique. Very long-time perturbations and various test are necessary to make the identified transfer functions smoother and more coherent, thus a very efficient vortex-lattice-like solver is derived from the BEM one.
The two methodologies are applied to study a mid-weight hovering helicopter and the corresponding dynamic inflow models implemented in a comprehensive simulation tool, *Helistab*, developed in the past within the ARISTOTEL research european project [64]. Specifically the influence of the ground on helicopter aeromechanics in terms of response and stability is assessed.

The text is organized as follows:

- In Chapter 2 the proposed aerodynamic solver suited for ground effect simulation is presented. It is a BEM, three dimensional, free-wake aerodynamic solver suited for rotor simulation, even for the case of strong interaction between bodies and wake. Here it is extended to the ground effect cases, in particular, the critical hovering condition over an infinite flat ground has been simulated and correlated with experimental data both for a parallel and inclined surface with respect to the rotor disc. Two different simulation strategies for modelling the ground effect are compared. The comparisons include tip vortices traces, rotor loads measurements and flow-fields visualizations;

- In Chapter 3 the dynamic wake inflow models for helicopter simulation are presented. Three models and their applications to ground effect are presented. The first two are based on a kinematic-inputs perturbations simulated through the BEM solver, hence inflow/rotor DOFs (Degree-Of-Freedoms) and inflow/air-loads models are extracted. The third instead, is an inflow/load model based on vorticity perturbations performed with a free-wake vortex-lattice-like solver;

- In Chapter 4 the numerical results concerning the identification of the identified dynamic inflow models are presented for different rotor heights from the ground

and different ground inclination angle. The accuracy of the models is validated by comparison with the predictions directly provided by the time-marching high-fidelity solver. In the last section of the chapter in-ground-effect and out-of-ground-effect state-space inflow models are applied for helicopter response and stability analyses, and the corresponding results are compared to discuss the influence of ground on helicopter aeromechanics.

Finally, in the last chapter the conclusion of this three years of work are drawn and some future possible development depicted.

Chapter 2

A Boundary Element Method Approach for In-Ground-Effect Rotor Aerodynamics

"Cómo marcha el reloj sin darse prisa
con tal seguridad que se come los años:
los días son pequeñas y pasajeras uvas,
los meses se destiñen descolgados del tiempo."
P. N.

In this chapter the boundary element method (BEM) solver for the aerodynamic simulation of hovering rotors in-ground-effect (IGE) is presented. Different in-ground-effect conditions are analyzed and compared by the correlation of the corresponding simulations with experimental data, in particular hovering over parallel and inclined flat surfaces.
The computational tool developed and used at Roma Tre University is based on a boundary integral equation approach for unsteady potential flows around lifting bodies in arbitrary motion, and is capable of dealing with flight conditions where strong body-vortex interactions occur [51]. Further improved in [65], it has been extensively validated and successfully applied to aerodynamic and aeroacoustic analyses of helicopter rotors, [63, 66, 67, 68].
Two methodologies for the simulation of the effects of the ground below the rotor are applied and their capabilities to predict wake evolution and rotor loads are compared, outlined in the following sections the two are:

- the bounded-domain method (BDM) which exploits the inclusion of an additional boundary surface modeled with a distribution of sources and doublets;
- the mirror-image method (MIM) that, considering the ground as a reflection plane, includes a specular rotor-wake in the formulation.

The experimental data used for validation are partly obtained from the available literature [34], but most of them derive from the recent campaign of measurements performed at the U.S. Naval Academy[1] [35]. The analysis will include tip vortices traces, rotor loads measurements and flow fields visualizations.

2.1 The IGE Aerodynamic Solver

The aerodynamic solver used here was directly derived from the Gennaretti and Bernardini [51] extension of Morino's BEM for aerodynamic applications [69]. The effectiveness of potential theory derives from the fact that vortical regions in many high-Reynolds-number flows of aeronautical interest are very thin (though not zero) and can be approximated by zero-thickness vortex structures. However, the numerical application of the potential theory, with its singular representation of vortical regions, would not yield the proper solution in the case of close wake-body interactions. Indeed, the numerical formulation based on [50] shows instabilities when the wake panels come too close to or directly impinge the body. The modified

[1] Data available through the participation to the Vertical Lift Rotorcraft Center of Excellence, VLRCOE [43].

formulation is a potential-based BEM in which a wake simulated as a vortex lattice is included in a direct panel method for potential flows, [51], moreover this formulation has required a reformulation of the Bernoulli theorem that is used for the evaluation of the pressure over the bodies and blades [70]. It is inspired by the observation that the instabilities (arising in the numerical formulation when wake panels are too close to or impinge on the body) would be eliminated by replacing the wake influence coefficients, given in terms of doublet layers, with equivalent finite core vortices. Indeed, the velocity field induced by a zero-*th* order doublet distribution of uniform intensity over an arbitrary surface S equals that induced by a (closed) vortex filament located on the boundary of the surface, also of the same constant intensity (see, for instance, [71] in which the more general equivalence between nonuniform doublet layers and vortex layers is proven). Then, if the vortex is assumed to have a finite core in which the induced velocity remains bounded, it yields a regular influence, even at body or wake points that approach it.

2.1.1 Aerodynamic formulation

Considering incompressible, potential flows such that $\vec{v} = \nabla\varphi$, the rotor aerodynamics formulation applied here assumes the potential field, φ, to be given by the superposition of an incident field, φ_I, and a scattered field, φ_S (*i.e.* $\varphi = \varphi_I + \varphi_S$). The scattered potential is determined by sources and doublets distributions over the surfaces of the blades, S_B, and by doublets distributed over the wake portion that is very close to the trailing edge from which it is emanated (near wake, S_W^N). The incident potential field is associated to doublets distributed over the complementary wake region that composes the far wake S_W^F. The wake surface partition is such that the far wake is the only wake portion that may come in contact with bodies (blades and/or ground). The incident potential is discontinuous across S_W^F, whereas the scattered potential is discontinuous across S_W^N and is represented by the following integral expression [51]

$$\varphi_S(\vec{x},t) = \int_{S_B} \left[G\,(v_n - u_n) - \varphi_S \frac{\partial G}{\partial n} \right] \mathrm{d}S(\vec{y}) - \int_{S_W^N} \Delta\varphi_S \, \frac{\partial G}{\partial n} \, \mathrm{d}S(\vec{y}) \tag{2.1}$$

where $G = -1/(4\pi\, r)$ is the unit-source solution of the three-dimensional Laplace equation, with $r = \|\vec{y} - \vec{x}\|$, while $\Delta\varphi_S$ is the potential jump across the wake surface, known from past history of potential discontinuity at the blade trailing edge through the Kutta-Joukowski condition [72, 73]. In addition, $v_n = \vec{v}_B \cdot \vec{n}$, with $\vec{v}_B$ representing the body velocity and $\vec{n}$ its outward unit normal, whereas $u_n = \vec{u}_I \cdot \vec{n}$, with $\vec{u}_I$ denoting the velocity induced by the far wake (see, for instance, equation 2.2).

For the numerical solution of the flow field, the integral formulation in Eq. 2.1 is discretized by a zero-th order BEM, for which body and wake surfaces are divided into quadrilateral panels. Velocity potential and velocity potential jump are assumed to be uniformly distributed over them, with values equal to those at the centroids of the elements. The solving algebraic system[2] is determined by imposing that the integral equation be satisfied at the centroid of each body element (collocation method).

Considering the far wake contribution discretized into panels with constant potential jump, and recalling the equivalence between surface distribution of doublets and vortices [71], the incident velocity field is evaluated through the Biot-Savart law applied to the vortices having the shape of the panel contours. In particular each single panel contribution in terms of doublet integral (recalling equation A.5 of App.A)

$$\vec{u}_I^k(x,t) = \Delta\varphi_S(y_{W_k}^{TE}, t-\tau_k)\nabla_x \int_{S_W^F} \frac{\partial G}{\partial n} dS(y) \tag{2.2}$$

becomes:

$$\vec{u}_I^k(x,t) = \Delta\varphi_S(y_{W_k}^{TE}, t-\tau_k) \int_{\partial S_W^F} \nabla_x G \times d\mathbf{y} \tag{2.3}$$

where ∂S_W^F represents the panel contour hence the shape vortex.

In order to assure a regular distribution of the induced velocity within the vortex core, and thus a stable and regular solution even in blade/ground-vortex impact conditions, a Rankine finite-thickness vortex model is introduced in the Biot-Savart law, [51], including also the vortex stretching and diffusion effects on core radius dimensions. In this formulation, the incident potential affects the scattered potential through the induced-velocity, while the scattered potential affects the incident potential by its trailing-edge discontinuity convected along the wake and yielding the intensity of the far wake vortices [51]. The shape of the wake surface is determined as part of the solution, as resulting from the history of the flow field induced by wakes and bodies. Once the potential field is known, the adapted Bernoulli theorem yields the pressure distribution (see, for instance, the appendix A of [65]) from which, in turn, blade and rotor loads can be readily evaluated.

In this work, the outlined formulation is extended/adapted to be capable of suitably taking into account, as efficiently as possible, the presence of ground below the rotor disk. Two approaches are applied and compared: one considers the ground as an impermeable boundary of the fluid domain (bounded-domain method, BDM), whereas the other simulates the effect of an infinite-size ground by including a specular rotor-wake configuration in the integral formulation (mirror-image method, MIM, for which the ground corresponds to the symmetry plane of the resulting

[2] In Appendix A the solving system is pointed out.

flow field [41, 74]). Note that, the BDM method is the most general one, in that it is capable of considering arbitrary ground shape, extension and even arbitrary motion.

2.1.2 The MIM approach for IGE analysis

In the MIM approach the effects of the ground are modeled by including a specular rotor-wake configuration in the integral formulation. Indeed, the impermeability boundary condition is automatically satisfied over the symmetry plane that, therefore, represents an exact simulation of the ground presence[3]. The application of this method, which is widely used in several aeronautic and nautical applications [75], corresponds to the solution of the following integral formulation

$$\begin{aligned}\varphi_S(\vec{x},t) = &\int_{S_B}\left[G\left(v_n-u_n\right)-\varphi_S\frac{\partial G}{\partial n}\right]\mathrm{d}S(\vec{y})-\int_{S_W^N}\Delta\varphi_S\,\frac{\partial G}{\partial n}\,\mathrm{d}S(\vec{y})\\ &+\int_{S_{B,m}}\left[G\left(v_n-u_n\right)-\varphi_S\frac{\partial G}{\partial n}\right]\mathrm{d}S(\vec{y})-\int_{S_{W,m}^N}\Delta\varphi_S\,\frac{\partial G}{\partial n}\,\mathrm{d}S(\vec{y})\end{aligned}\tag{2.4}$$

where $S_{B,m}$ and $S_{W,m}^N$ denote the surface of the mirrored rotor and that of the mirrored near wake, respectively. The velocity potential over the body surfaces and the velocity potential discontinuity over the wakes are assumed to be the same for the rotor and its mirrored image. Figure 2.1 shows a sample rotor blade-hub geometry with its specular image, with the red plane (line) representing the symmetry plane that simulates a ground surface parallel to the rotor disk.

[3] Considering for instance a source posed at certain distance z^* over an infinite flat surface (ground), the impermeability condition states that the normal component of the velocity has to be zero at the surface. Neglecting for a while the surface below the source and considering a control point on the source footprint, the source itself will induce a velocity having an normal component $v_{n_1}^* < 0$ if the positive normal direction is from the surface inward to the fluid domain. A specular source (*i.e., same intensity but opposite z^* from the surface*) will induce, on the same control point, an opposite but equal $v_{n_2}^*$ (positive if projected over the aforementioned normal), which combined with the former one will automatically satisfies the impermeability condition over the infinite flat surface at the considered control point, $v \cdot n = v_{n_1}^* - v_{n_2}^* = 0$. It can be demonstrated that the mirroring of the source is equivalent to the evaluation of the half-space Green function one can write for this kind of fluid-domain (namely an half-region delimited by an infinite flat surface).

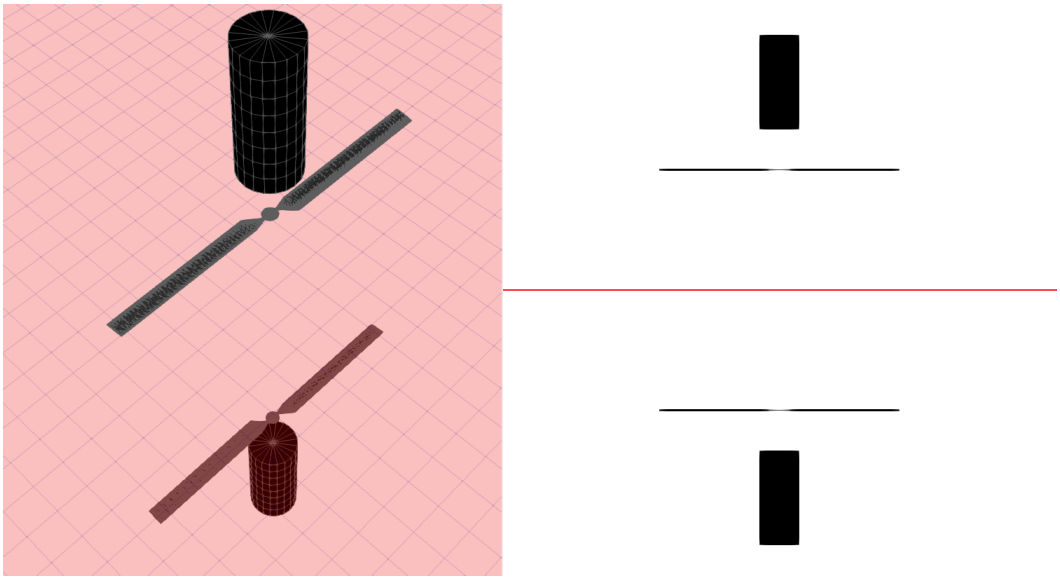

Figure 2.1. Rotor/mirrored-rotor sample.

It is worth noting that, in principle, the BEM-MIM approach is capable of simulating only the presence of an infinite flat surface. It has been shown that it can be extended to the case of arbitrarily shaped grounds through the *generalized image method*, which consists of the combination of multiple-sequential applications of the MIM technique to a set of flat surfaces that suitably envelope the ground surface, [76].

2.1.3 The BDM approach for IGE analysis

In the BDM approach, instead, the ground below the rotor is modeled as an additional boundary of the fluid domain. This approach is totally general and the boundary could have any arbitrary shape (e.g.: additional body, ground with obstacle, ship deck, ecc...). Thus the boundary integral formulation describes its effects as a superposition of sources and doublets distribution as follows

$$\varphi_S(\vec{x},t) = \int_{S_B}\left[G\,(v_n-u_n)-\varphi_S\frac{\partial G}{\partial n}\right]\mathrm{d}S(\vec{y}) - \int_{S_W^N}\Delta\varphi_S\,\frac{\partial G}{\partial n}\,\mathrm{d}S(\vec{y}) + \int_{S_G}\left[G\,\frac{\partial \varphi_S}{\partial n}-\varphi_S\frac{\partial G}{\partial n}\right]\mathrm{d}S(\vec{y}) \tag{2.5}$$

where S_G denotes the surface of the ground below the rotor, where the impermeability boundary condition yields

$$\frac{\partial \varphi_S}{\partial n} = \vec{v}_G\cdot\vec{n}-u_n \tag{2.6}$$

for $\vec{v}_G$ representing the ground velocity[4]. Past numerical investigations have proven that the satisfaction of such a boundary condition may be a complex numerical task, depending on the ground geometry, [49]. In appendix C a numerical-semi-empirical strategy to enforce the impermeability condition is presented and briefly discussed.

2.2 Wake Modeling for Computational Efficient Ground Effect Simulation

The aerodynamic BEM solver of Section 2.1, exploiting the identity between a zero-th order discretized thin surface doublets distribution (see for instance App.A) and a net of vortices having the shape of the panel contours, actually transforms a full classic boundary element formulation [72] in a sort of hybrid vortex-net/BEM aerodynamic solver. This effectively allows redefining the far-wake contribution in the potential integral formulation in such a way that a regular solution is obtained even in the case of strong body-vortex interaction be it blade-vortex (BVI) or ground/obstacle-wake interaction (*i.e., IGE operation*). Nevertheless, due to the long wake ages needed for ground effect simulation (typically more than ten wake spires), in order to improve the computational efficiency of the code a new wake solution algorithm has been implemented.
A lattice of discrete vortex elements like this is literally seeing the vorticity released at blade trailing edge decomposed in two different components, the first (trailed vorticity) related to the spatial derivative of the blade bound circulation, whereas the latter (shed vorticity) is related to the time (azimuthal) derivative. Even if a real (physical) distinction between these two components (trailed and shed) does not exist, but considering the experimental evidence of less time resilience of the shed vorticity, the key point of this novel algorithm stands in neglecting the shed vorticity for the wake older than a certain wake age, it is indeed well known that only the near blade portion of the wake needs to be well discretized in order to capture all the dynamic features of the air-load (*i.e. high-harmonic component*) [36, 77].

[4] In the whole research activity of this thesis the ground has been considered fix (*i.e.*,$\vec{v}_G = 0$), the extension to moving ground will be addressed in the future.

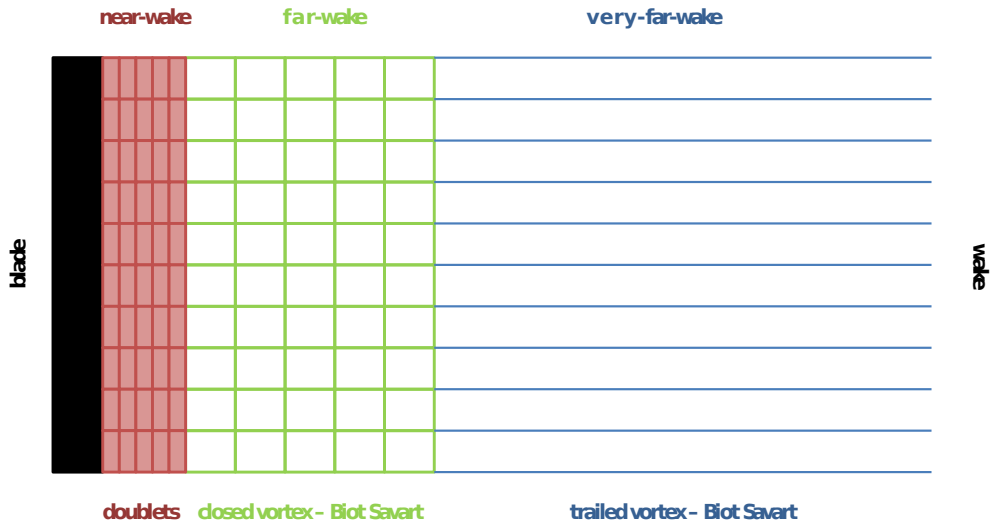

Figure 2.2. Sketch of the proposed wake partitioning.

In the implemented wake algorithm, thus, the shed contribution after a certain wake age Ψ^* is neglected and the vortex lattice is transformed into a vortex-filament-like wake model. The hybrid aerodynamic solver so obtained can have up to three wake parts (see figure 2.2):

Near-Wake the wake region closer to the blade, modeled as a thin layer of doublets (*e.g.:* $\Psi_{wake} \leq 45°$), directly contributes to equation 2.5 (doublet integral over S_W^N);

Far-Wake the following region where the wake is modeled like a vortex lattice surface (*e.g.:* $45° \leq \Psi_{wake} \leq 720°$), which influences the boundary condition of equation 2.5, $\vec{u}_I$ evaluation ;

Very-Far-Wake the last region (*e.g.:* $\Psi_{wake} > 720°$), far from the rotor the only trailed vortex filaments survive and, again, influence the boundary condition of equation 2.5, $\vec{u}_I$ evaluation.

IGE simulation usually require more than 10 wake revolutions, with this approach for the evaluation of the wake contribution the computational effort is reduced of about 30% with respect to the classical wake algorithm.

2.2.1 Preliminary results

A two-bladed, untwisted, untapered rotor has been chosen as test rotor, table 2.1 summarizes the main characteristic of the blade. In the following figures the proposed more computationally efficient wake solver is compared with the results obtained thanks to the original algorithm, the simulation has been performed for an hovering condition and the wake was set free.

Radius	0.408 m
Chord	0.0448 m
Root-Cut-Out	0.05 m
Airfoil	NACA 0012
Collective Pitch	6°
Angular Velocity	219.9 rad/s

Table 2.1. Characteristics of two-bladed rotor.

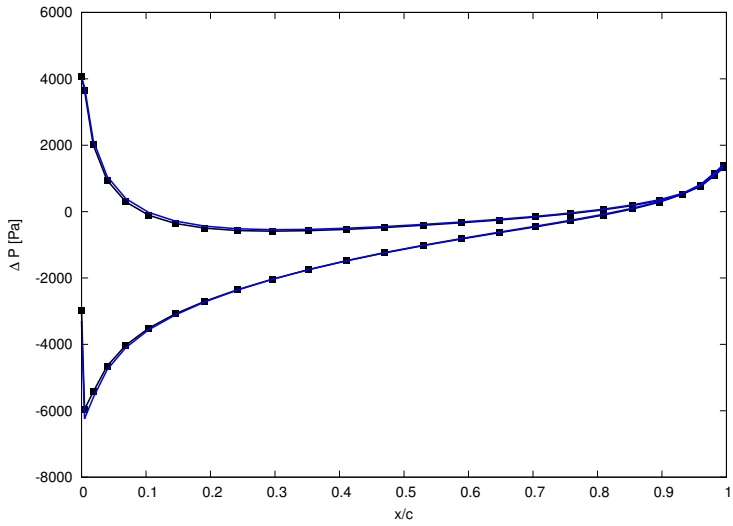

Figure 2.3. Averaged pressure coefficient, radial station $0.8\,x/R$. ■ vortex-lattice, — vortex-filament (only trailed).

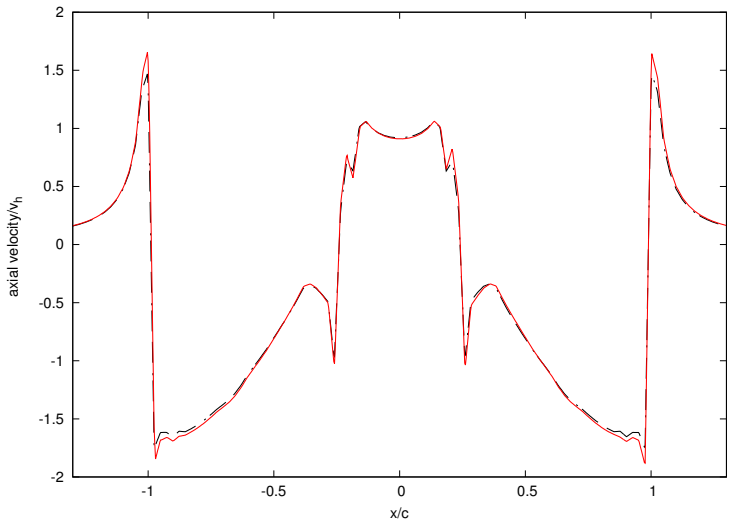

Figure 2.4. Averaged inflow, – – – vortex-lattice, ——— vortex-filament (only trailed).

Figures 2.3 and 2.4 show the averaged pressure coefficient for a section at $x/R = 0.8$ and the wake induced inflow over the blade, very good agreement can be seen between the two solution algorithm confirming the validity of the hypothesis. Looking at global quantities like thrust and power there is less than 1% of error in thrust evaluation (underestimate) and less than 2% in induced losses (underestimate). Figure 2.5, depicts the time history of the trailing edge discontinuity $\Delta\varphi$ for four blade element, the very close behaviour between the two series of curves confirms the good quality of the vortex-filament approach for the far-wake.

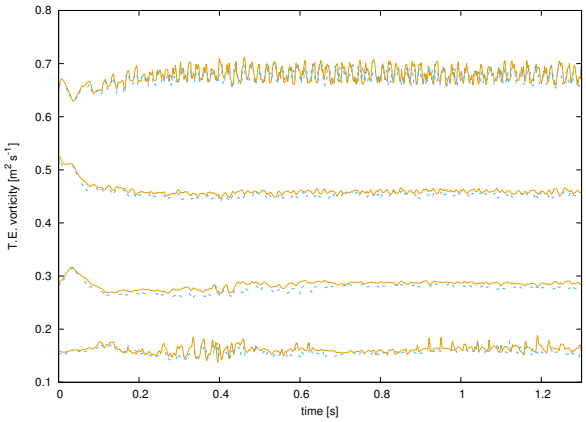

Figure 2.5. $\Delta\Phi$- Time history for four different radial position (from bottom to top: $x/R = 0.17$, $x/R = 0.34$, $x/R = 0.56$ and $x/R = 0.71$), ——— vortex-lattice, ——— vortex-filament.

Then the figures 2.6, 2.7 and 2.8 show, instead, the time history of two generic nodes of the far wake, it is clear how also the wake evolution is almost the same

with respect to the original wake algorithm, figure 2.9 shows a slice of the wake of an hovering rotor reproduced with the here presented wake structure[5]. Concluding, these new algorithm, even if allowing a reduction of about the 30% in the number of calculations needed for the wake evaluation, retains the same accuracy of the original vortex-lattice one.

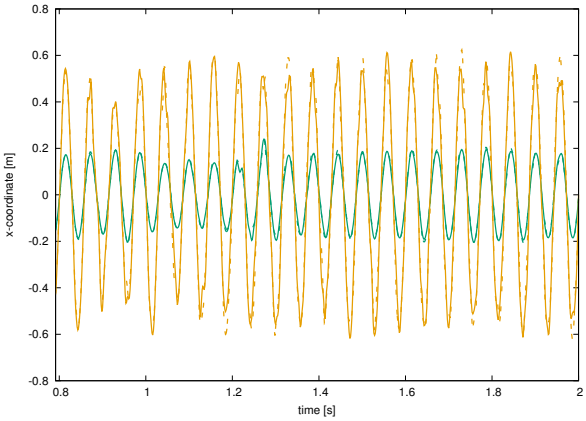

Figure 2.6. X-coordinate - Time history for two different wake nodes (—— node 1, —— node 2), dashed rule represents vortex-lattice results whereas continuous line the vortex-filament ones.

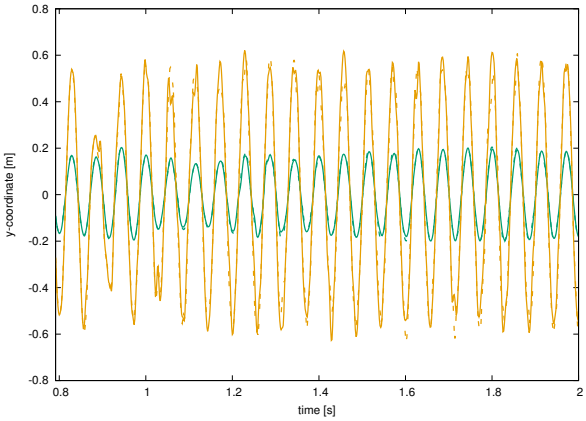

Figure 2.7. Y-coordinate - Time history for two different wake nodes (—— node 1, —— node 2), dashed rule represents vortex-lattice results whereas continuous line the vortex-filament ones.

[5]The wake coloring depends on the blade bound circulation.

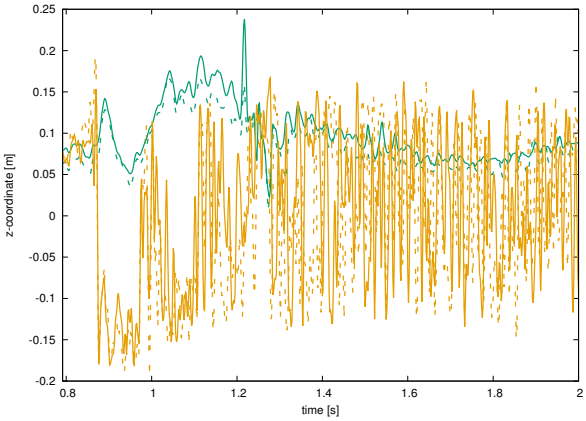

Figure 2.8. Z-coordinate wake - Time history for two different wake nodes (—— node 1, —— node 2), dashed rule represents vortex-lattice results whereas continuous line the vortex-filament ones.

The results shown in the following section could be indifferently obtained with one of the two algorithms, for this reason there will be non more reference to which one of the two is used.

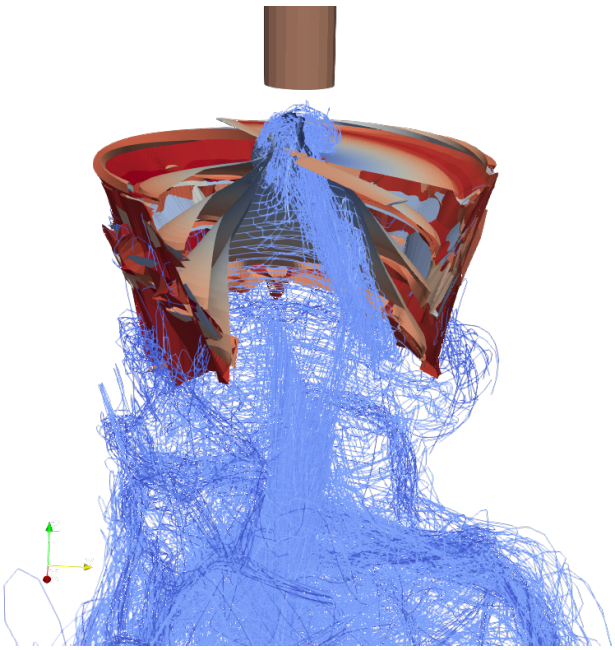

Figure 2.9. 3-D vision of the new wake.

2.3 Numerical-experimental results correlation

The validation of the numerical solvers proposed for IGE rotor aerodynamics analysis based on BDM and MIM techniques is performed by correlation with experimental data, in terms of both rotor performance prediction (thrust and induced power), and capability of simulating flow field and wake shape. Two sets of experimental data are mainly considered: those provided in 1993 by the work of Light [34] concerning a four-bladed rotor both in HIGE and HOGE (hovering-in/out-of-ground effect) conditions, and the results of the recent experimental campaign performed at the U.S. Naval Academy [35] for a two-bladed rotor hovering over parallel and inclined plane ground.
For the four-bladed rotor, whose main characteristics are given in Table 2.2, Light's work provides measurements of rotor thrust and positions of the tip vortex of the first wake spiral as determined through shadow-graph visualization of the wake geometry. These data are given for different fixed collective pitch input and several values of the rotor-ground distance, h_g/R.

Span	1.105	m
Root-Cut-Out	0.425	m
Chord	0.18	m
Solidity	0.207	-
Airfoil	NPL 9165	-
Angular Velocity	172.3	rad/s

Table 2.2. Characteristics of four-bladed rotor of Ref. [34].

In the experimental campaign performed at the U.S. Naval Academy experimental facilities particle image velocimetry (PIV) and performance measurements concerned the two-bladed rotor described in Table 2.3.

Radius	0.408 m
Chord	0.0448 m
Root-Cut-Out	0.05 m
Airfoil	NACA 0012
Collective Pitch	6°
Angular Velocity	219.9 rad/s

Table 2.3. Characteristics of two-bladed rotor examined at the U.S. Naval Academy [35].

The rotor was tested in HOGE and HIGE ($h_g/R = 1$) hovering conditions, for

ground plane both parallel to the rotor disk ($\theta_g = 0°$) and inclined with respect to it ($\theta_g = [6°, 10°, 15°, 20°, 30°]$) [35]. The hub loads were obtained using a six-axis load cell for collective pitch angles in the range $\theta_c = [0° - 12°]$, with 2°-degree increments. Flow field measurements were performed using both a high- and a low-speed PIV system. The high-speed system comprised two 4-megapixel (1280×800 pixel) CMOS camera and the regions of interest were illuminated using a light sheet produced by a 30 mJ/pulse Nd:YLF laser. The low-speed system utilized an Nd:YAG laser capable of producing 380 mJ/pulse when operated below 10 Hz, and two 29-megapixel (6600×4400 pixel) cameras. For each measurement type the cameras were aligned adjacent with a 20% overlap in their fields of view, allowing the temporally correlated images to be stitched together. The high-speed measurements focused on a region of interest in the near field of the rotor that encompassed the entire blade. To examine the whole wake as it convected from the rotor to the ground, the low-speed cameras were focused on a region encompassing the entire rotor, as well as the ground plane. Furthermore, to examine the entire structure of the rotor wake, measurements were taken at azimuthal location range $[0 - 180]$ degrees, in 30degree increments. The numerical predictions presented in the following have been obtained by using a surface discretization of 2000 body panels for each blade and 72000 wake panels, corresponding to 12 turns (200 body panels have been used for describing the cylinder that simulates the motor in the U.S. Naval Academy experiments [35]). The flow-field velocities to be compared with PIV data, have been evaluated over a 120×90 rectangular grid of control points lying on a plane perpendicular to the rotor disk and containing the axis of rotation, with a 180/rev sampling frequency, averaged over 50 rotor revolutions (only the in-plane velocity components have been examined), also rotor performance predictions have been averaged over 50 rotor revolutions.

2.3.1 Wake shape prediction

First, the wake shape simulation capability is examined by comparison with Light's results. For the rotor operating in HOGE conditions with $C_T/\sigma = 0.091$ (where σ is the rotor solidity), Fig. 2.10 shows radial and axial position of the vortex tip as functions of the wake age predicted by the present BDM solver, measured in Ref. [34] and corresponding to the widely-used Landgrebe wake model based on experimental observations [78]. In this HOGE case, these results present good agreement for both near and far wake shape, both in terms of radial and axial tip vortex position.

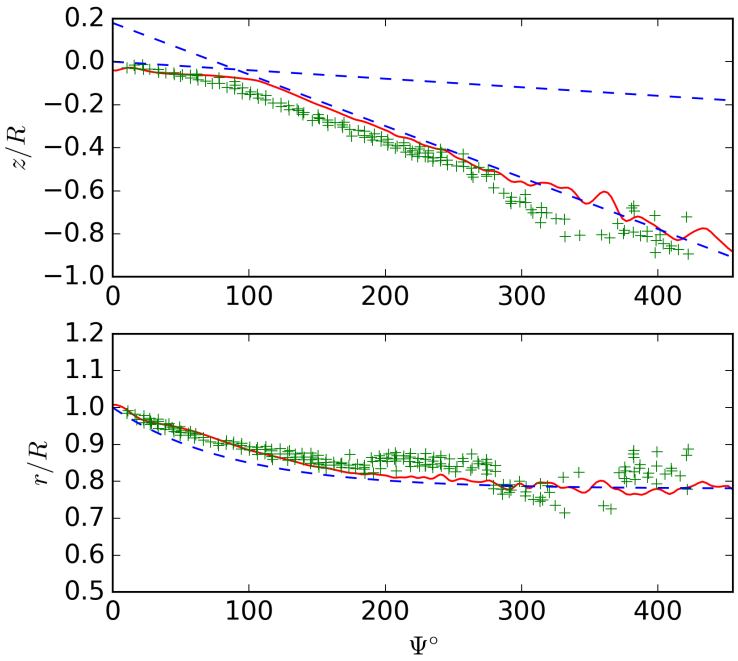

Figure 2.10. Axial and radial position of tip vortex in OGE condition, $C_T/\sigma = 0.091$. present results; Landgrebe; + experiments.

The same comparisons are shown in Figs. 2.11 and 2.12 for two different IGE configurations. In particular, Fig. 2.12 presents the results obtained for rotor loading $C_T/\sigma = 0.071$ and ground distance $h_g/R = 0.84$, whereas the results in Fig. 2.11 concern the configuration with rotor loading $C_T/\sigma = 0.09$ and ground distance $h_g/R = 0.52$. Both figures show good agreement between experimental observations and numerical simulations. The characteristic wake distortion effects of ground seem to be well captured by the numerical predictions.

Indeed, experimental and numerical results show that, after an initial radial contraction similar to that of the HOGE case, the wake starts expanding due to the ground presence, with a rate depending on the distance from the ground.

Instead, concerning the axial position of the tip vortex, for $h_g/R = 0.84$ ground effects are significant only when the wake is in proximity of the ground, where its axial convection rate tends to become negligible, whereas for $h_g/R = 0.52$ the axial convection rate of the tip vortex is significantly reduced by the ground presence since the beginning of the wake spirals [6].

Then the tip vortex position in the whole region between rotor and ground has been examined, starting from the data available from the U.S.N.A. experimental campaign [35] the two proposed strategies (MIM-BDM) are compared. The rotor and the test

[6] youngest wake elements.

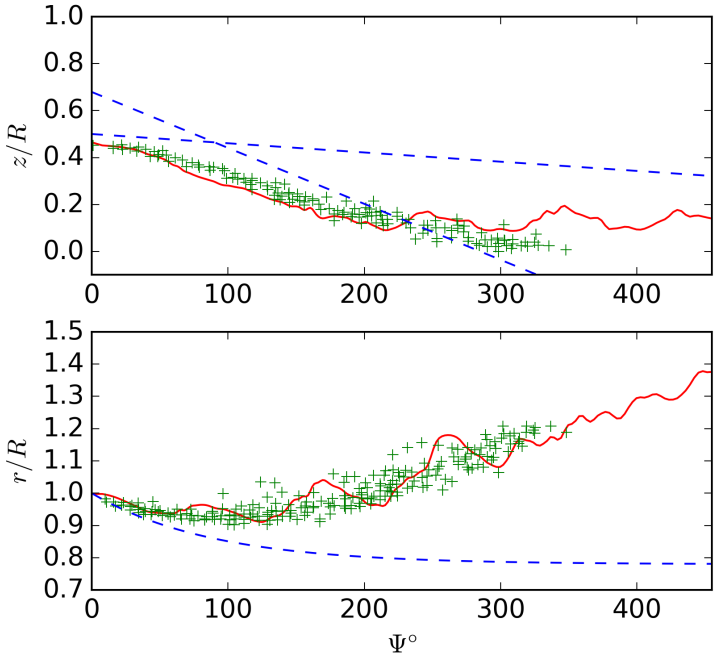

Figure 2.11. Axial and radial position of tip vortex in IGE condition, $h_g = 0.52R$ and$C_T/\sigma = 0.09$. — present results; - - - Landgrebe; + experiments.

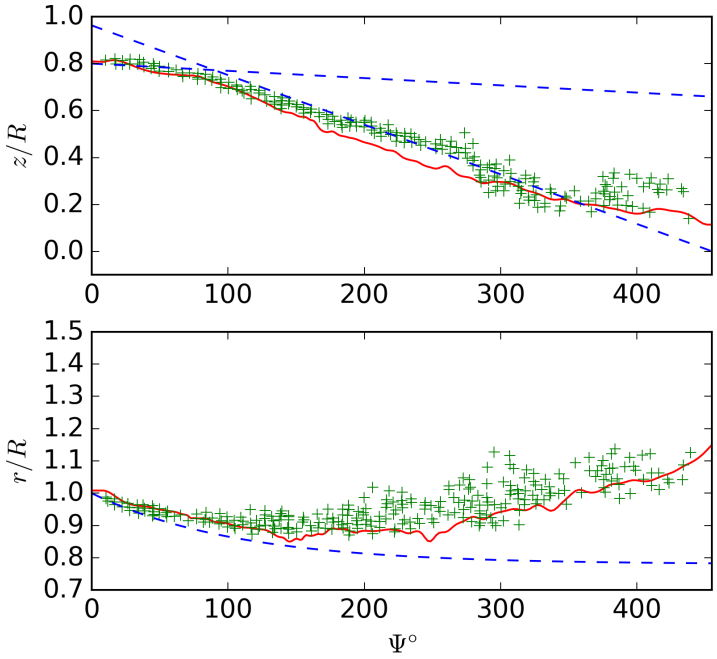

Figure 2.12. Axial and radial position of tip vortex in IGE condition, $h_g = 0.84R$ and$C_T/\sigma = 0.071$. — present results; - - - Landgrebe; + experiments.

conditions measured by Milluzzo (2.3) has been simulated also by Platzer, 2018 [42], in particular considering the different aerodynamic solver used (CFD code), which considers the fluid viscosity, it is worth including in the comparison also this results in order to evaluate the influence of the viscosity in the correct simulation of the ground effect condition.

The figures 2.13 and 2.14 show the vorticity contour plot for parallel and inclined ground effect, from the left-top corner in a clock-wise direction: experimental data, CFD simulation, BEM-MIM and BEM-BDM simulation. First of all, a preliminary comment has to be introduced: the assumption of potential flow implies irrotational velocity field ($\nabla \times \vec{u} = 0$), hence no vorticity can appear in the fluid domain except for the wake surface. However, the introduction of the Rankine finite vortex core, and the corresponding diffusivity modeling, introduces rotational time-variant fluid region representing each of the wake trailed vortices. Thus, these figures identify the tip vortex location in the wake region during its convection as the result of the combined evolution of the wake trailed vortices. Specifically, the vortices trailed in the outer part of the blade, near the tip, roll-up and clump together just after their release causing the blue and red zone of figures 2.13(c), 2.13(d), 2.14(c) and 2.14(d).

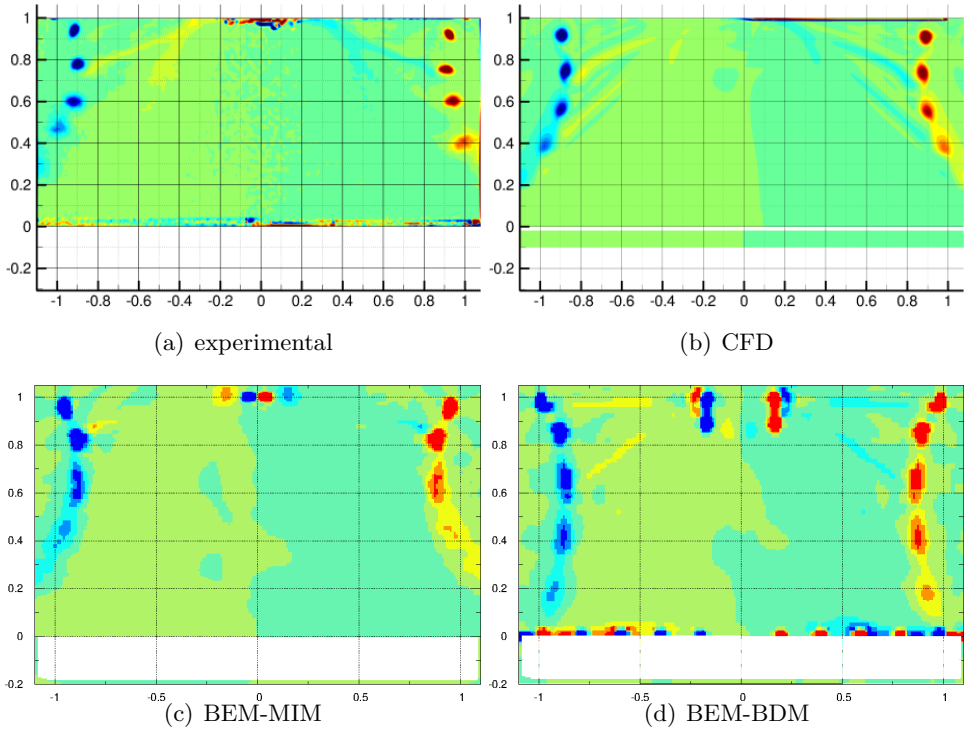

(a) experimental (b) CFD

(c) BEM-MIM (d) BEM-BDM

Figure 2.13. Tip vortex position for parallel ground hovering, $h_g/R = 1$, $\theta_g = 0°$.

However, from figure 2.13, referring to the parallel ground condition, one can

appreciate how the BEM-BDM fails in the evaluation of the wake-ground interaction, the radial expansion is strongly underestimated. Looking instead at the figure 2.14, which depicts the comparison for the inclined ground condition ($\theta_g = 15°$) there is absolutely no agreement between the BEM-BDM prediction and the experimental results, on the other hand the CFD and BEM-MIM simulations are in good agreement with the experimental evidence.

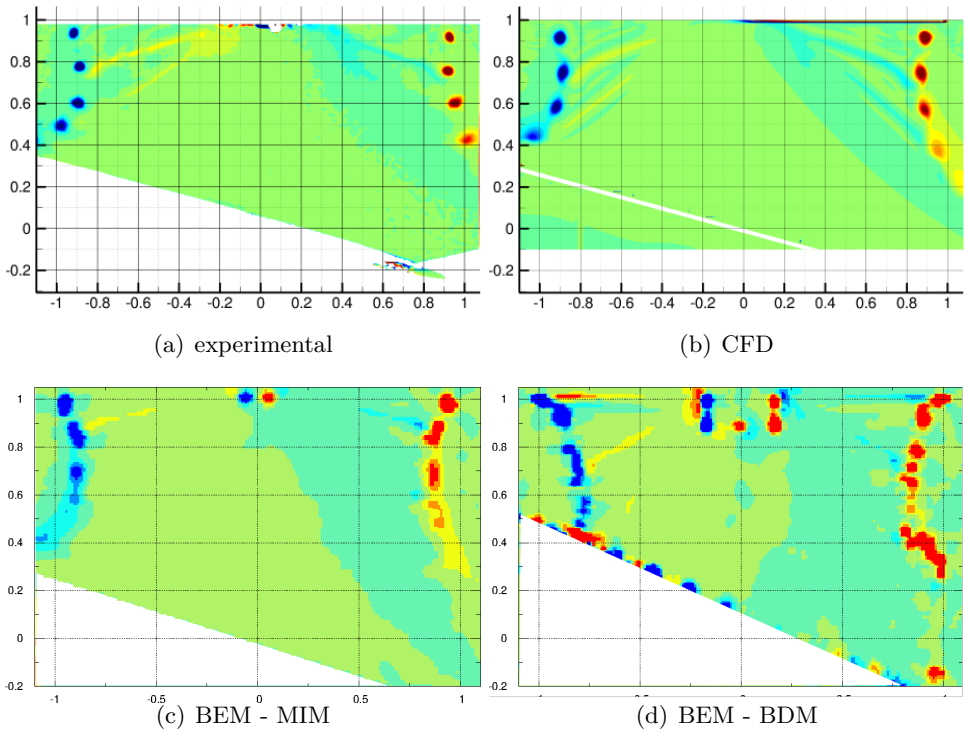

(a) experimental (b) CFD

(c) BEM - MIM (d) BEM - BDM

Figure 2.14. Tip vortex position for parallel ground hovering, $h_g/R = 1$, $\theta_g = 15°$[7].

2.3.2 Velocity profile comparison

The two methods (BDM and MIM) are also compared correlating the axial and radial distribution of the total velocity measured along perpendicular (vertical) and parallel lines (horizontal) related to ground plane. Three positions for the vertical lines are chosen, two in the proximity of the blade tip[8], figure 2.15 and 2.16 and one at $x/R = 1.5$ from the hub center, figure 2.17, discrepancies are evident from the comparison, both in the axial and radial velocity distribution. As the measurement

[7] Differently that for the other figures, referred to $\theta_g = 15°$, the BEM-BDM figure is referred to the case $\theta_g = 20°$, however the figures are just for a qualitative showing of the numerical problems related to the ground effect simulation.

[8] Respectively $r/R = 0.93$ and $r/R = 1.$.

point goes far from the blade the difference becomes higher, in particular it is worth noting that in the ground proximity the BDM method fails in the evaluation of the impermeability condition (see also App. C) evaluating even a negative velocity component, see fig.2.16(a).

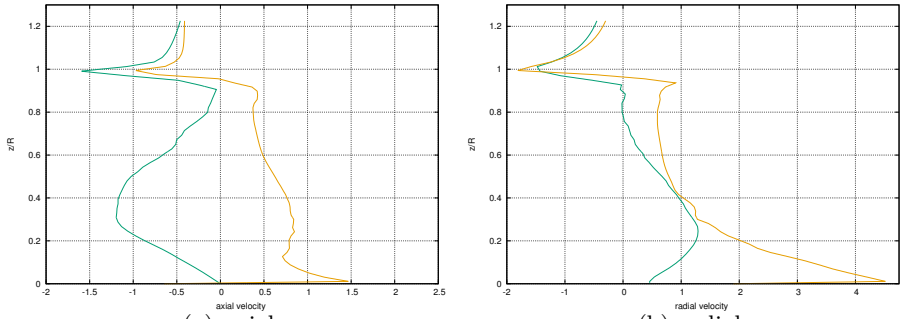

(a) axial (b) radial

Figure 2.15. Axial and radial wake induced velocity (normalized with $\Omega r_{tip}/C_T$) distribution over a vertical line at $x/R = 0.93$. BEM-MIM method, BEM-BDM method.

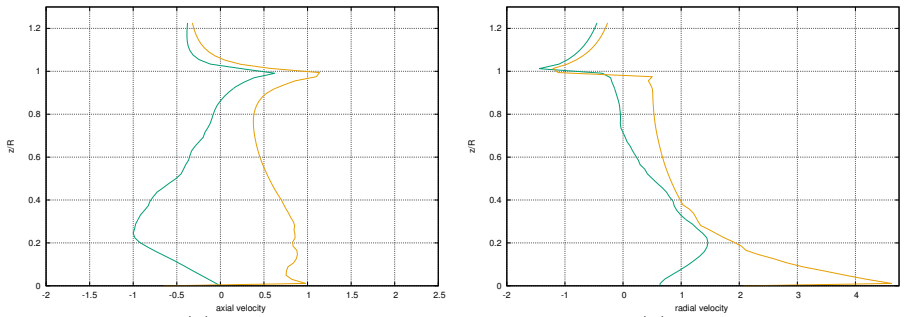

(a) axial (b) radial

Figure 2.16. Axial and radial wake induced velocity (normalized with $v_h = \Omega r_{tip}/C_T$) distribution over a vertical line at $x/R = 1$. BEM-MIM method, BEM-BDM method.

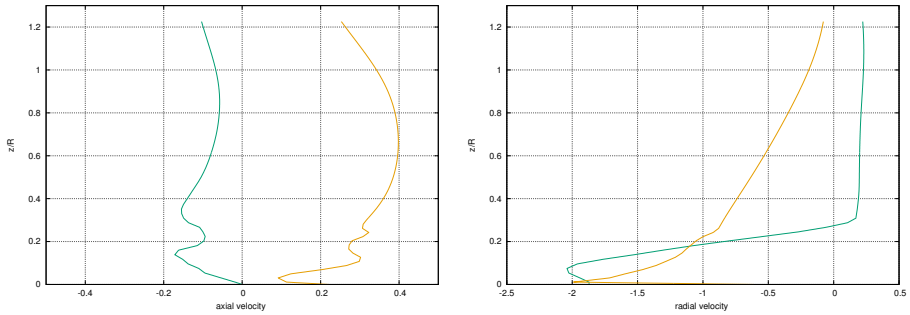

(a) axial (b) radial

Figure 2.17. Axial and radial wake induced velocity (normalized with $v_h = \Omega r_{tip}/C_T$) distribution over a vertical line at $x/R = 1.5$. BEM-MIM method, BEM-BDM method.

Figure 2.18 particularly emphasizes the error one can commit with BDM method in the evaluation of the normal to ground component of the velocity. Even if for the higher ground-to-line examined distance the BDM evaluates a positive component despite the MIM predicts almost a negative contribution, then, as the evaluation line comes closer to the ground, the MIM method predicts a near-zero velocity whereas the BDM one could forecast a negative component which inevitably leads the wake node to cross the ground surface.

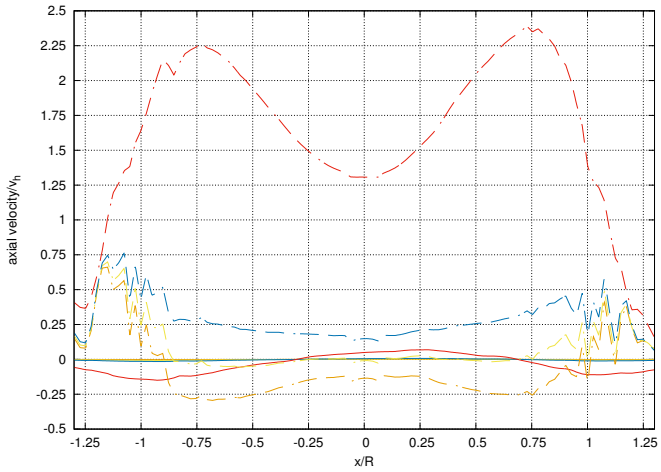

Figure 2.18. Axial wake induced velocity (normalized with $v_h = \Omega r_{tip}/C_T$) distribution over horizontal lines: $z/R = 0.025$; $z/R = 0.0025$; $z/R = 0.0013$ and $z/R = 0.00025$. Continuous lines are for BEM-MIM method, dashed for BEM-BDM.

2.3.3 Flow field prediction

Next, the experimental-numerical correlation is focused on the flow field generated between rotor disk and ground (for parallel and inclined ground configurations),

where strong rotor wake distortion may occur because of IGE phenomena thus, in turn, altering rotor aerodynamics.
In the following results (time-average), for the flow field observed on a vertical plane beneath the rotor orthogonal to the line of rotation of the inclined plane, the numerical simulations are obtained by the MIM approach (for the reasons explained above, 2.3.2), the flow velocity is nondimensionalized by the factor $v_h = \Omega R\sqrt{C_T/2}$, and the observation domain size is represented in terms of rotor radius lengths.

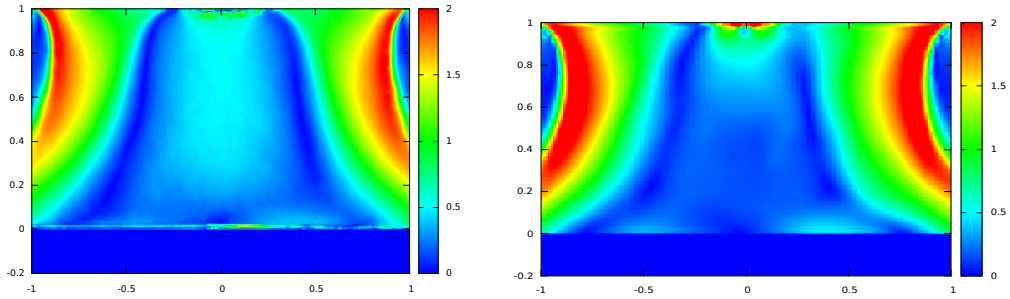

(a) experimental (b) numerical

Figure 2.19. Flow-field velocity magnitude pattern, parallel ground, $\theta_g = 0°$.

Figure 2.19 shows the flow velocity magnitude pattern on a vertical plane beneath the rotor, for the case of ground parallel to the rotor disk $\theta_g = 0°$. Only the in-plane velocity components are considered for the evaluation of the magnitude (as suggested by the PIV experimental measurements). Experimental results and numerical predictions are in good agreement. Both results show a very similar initial contraction of the wake, followed by an expansion in proximity of the ground (the red region is representative of the high-velocity tip-vortex region), and an internal very low velocity field (slightly underestimated, however, by the numerical simulations).

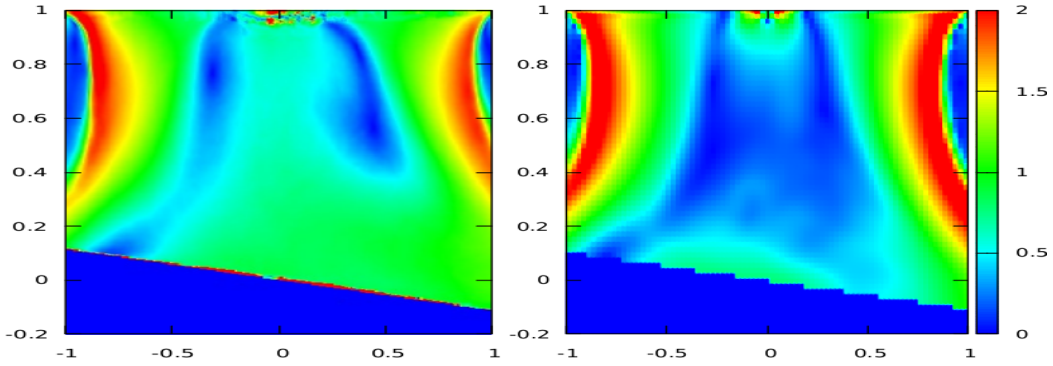

(a) experimental (b) numerical

Figure 2.20. Flow-field velocity magnitude pattern, inclined ground, $\theta_g = 6°$.

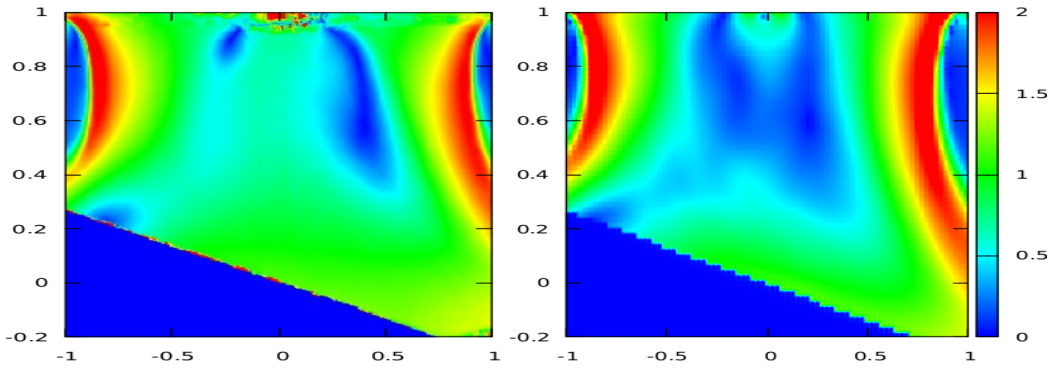

(a) experimental (b) numerical

Figure 2.21. Flow-field velocity magnitude pattern, inclined ground, $\theta_g = 15°$.

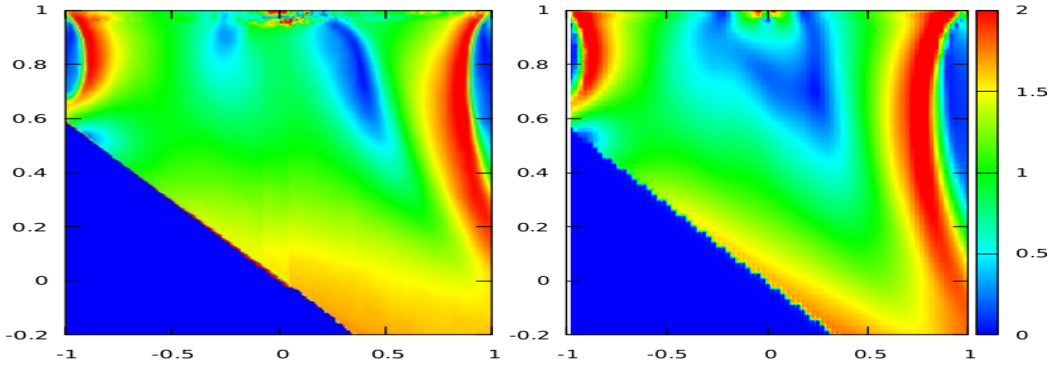

(a) experimental (b) numerical

Figure 2.22. Flow-field velocity magnitude pattern, inclined ground, $\theta_g = 30°$.

Next, Figs. 2.20-2.22 present the experimental-numerical correlations of the flow field beneath the rotor for non-parallel ground. Specifically, they concern ground plane angles equal to $\theta_g = 6°$, $\theta_g = 15°$ and $\theta_g = 30°$, respectively. For all these cases, it is proven that the numerical solver is capable of capturing the main features of the influence of the ground inclination, with the numerical simulations in good agreement with the experimental measurements. With respect to the parallel ground case, in the uphill side the wake is forced to expand more rapidly proportionally to the ground inclination (indeed, the curvature of the tip vortex trace increases with the ground inclination angle). The opposite phenomenon occurs on the downhill side, and both are well reproduced by the computational tool. The fluid in the inner wake region still has a low velocity, although slightly higher that in the parallel ground case, because of the asymmetric flow configuration caused by the ground inclination. This is observed both in the experimental results and in the numerical predictions, although the latter still presents a slight underestimation of the inner flow velocity magnitude.

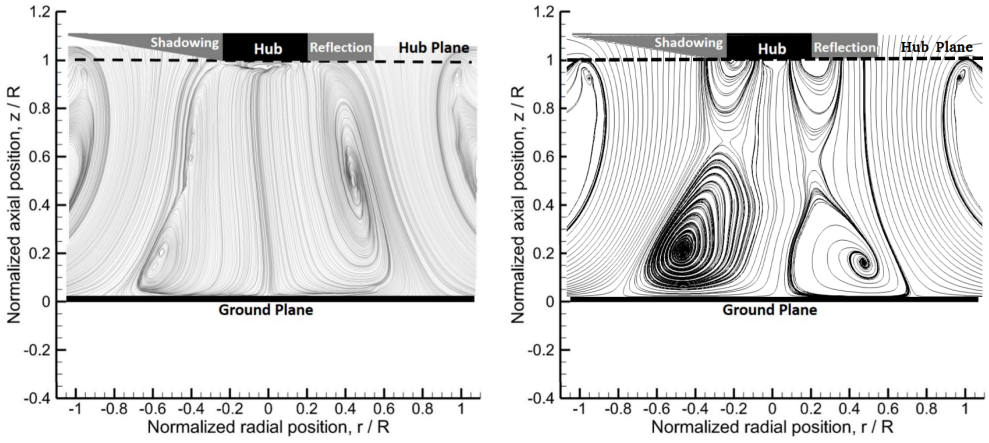

(a) experimental (b) numerical

Figure 2.23. Flow-field streamlines, parallel ground, $\theta_g = 0°$.

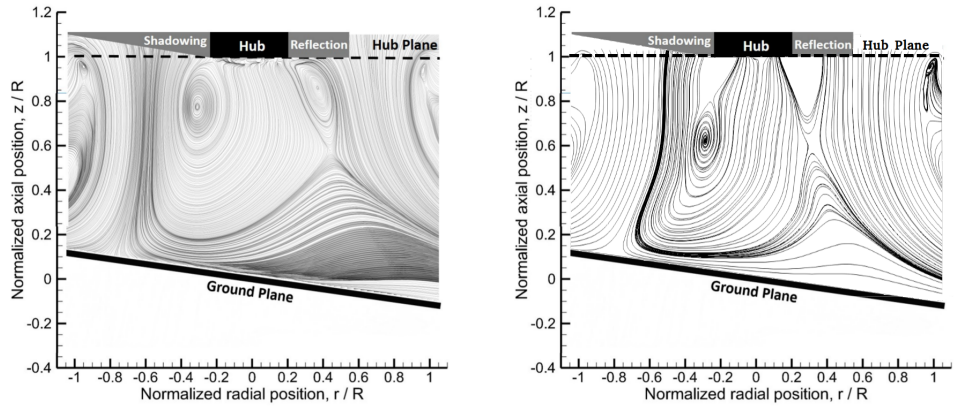

(a) experimental (b) numerical

Figure 2.24. Flow-field streamlines, inclined ground, $\theta_g = 6°$.

In addition, for the same rotor-ground configurations, Figs. 2.23-2.26 present the flow streamlines beneath the rotor observed by experiments and predicted by the MIM approach.

Figure 2.23 shows that, for the parallel ground case, the aerodynamic solver well captures the presence of two almost symmetric regular downwash streams bounding the wake that initially are subject to contraction, while expand in proximity of the ground generating two wall-jet flows. At the same time, two (low-velocity) internal flow recirculation regions are well simulated, although each one presents two recirculation sub-structures not appearing in the experimental observation.

As the ground inclination angle increases the flow field becomes more and more asymmetric, with the transformation of the uphill internal recirculation region into

a third low-velocity downhill oriented wall-jet flow, and the size reduction of the outer uphill downwash stream. For $\theta_g = 30°$, Fig. 2.26 shows that the downhill recirculation flow region has become a small recirculation area next to the hub, with the flow field dominated by a low-velocity wall-jet flow and a high velocity stream, both directed downhill.

The inclined-ground flow configurations are well captured by the numerical tool, with some minor discrepancies with respect to the experimental observation arising in the very-low-velocity internal recirculation flow region. Note also that the aerodynamic solver well predicts the position of the ground stagnation points for all θ_g's considered (three for $\theta_g = 0°$ and one for $\theta_g > 0°$).

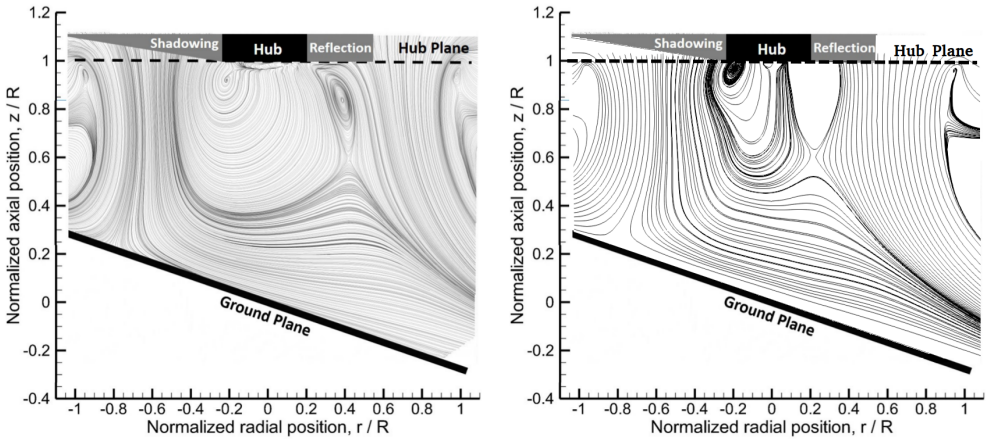

(a) experimental (b) numerical

Figure 2.25. Flow-field streamlines, inclined ground, $\theta_g = 15°$.

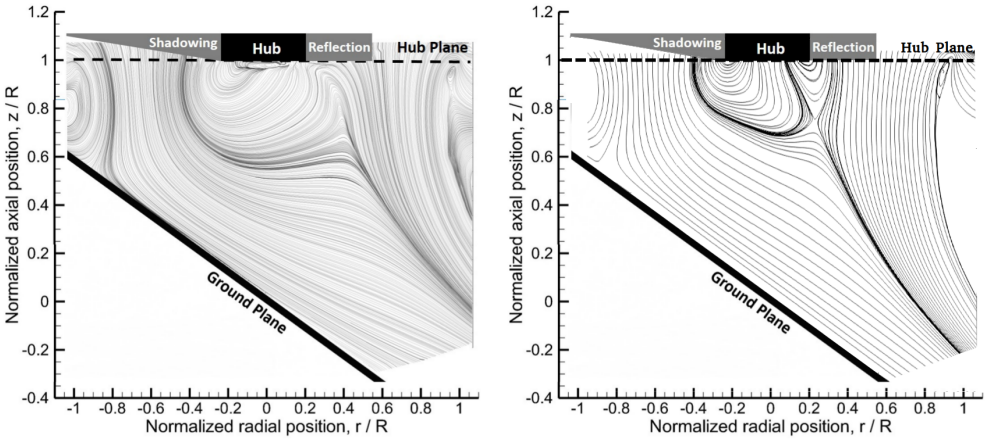

(a) experimental (b) numerical

Figure 2.26. Flow-field streamlines, inclined ground, $\theta_g = 30°$.

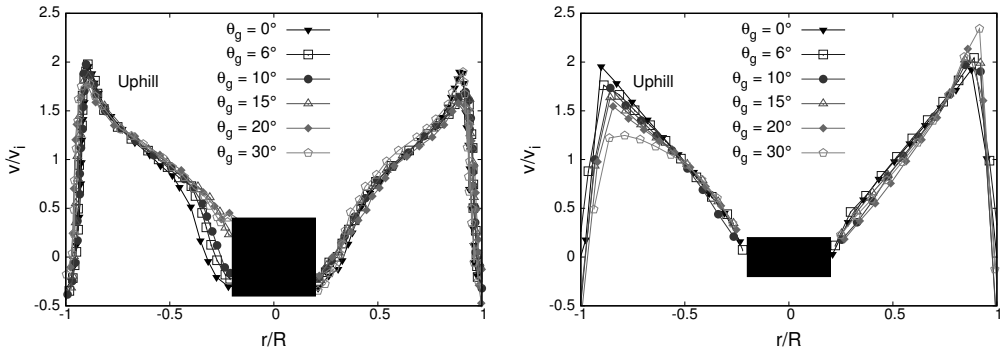

(a) experimental (b) numerical

Figure 2.27. Axial wake inflow on rotor disk for $0° \leq \theta_g \leq 30°$.

Finally, the effect of the ground plane inclination angle on the wake inflow on the rotor disk is examined. Indeed, it plays a crucial role on the rotor loading, in that directly affects the effective angle of attack at which the blade sections operate.

Figure 2.27 presents experimental measurements and numerical evaluations of the radial distribution of nondimensional rotor wake axial inflow, v_i/v_h, for different ground inclination angles. Starting from the parallel ground case, in which the radial distribution is almost symmetric, for increasing ground angle the numerical simulations show a reduction of the axial velocity in the uphill side and an opposite behavior in the downhill side. This seems to confirm the expected effect of flow blockage caused by ground when getting closer to the rotor, like in the uphill side. Although in the average experimental measurements and numerical predictions well correlate, in the experimental data the asymmetry induced by ground inclination is not clearly present: flow turbulence and measurement uncertainty might be causes that make it non visible.

2.3.4 Rotor performance prediction

The effect of close ground on rotor loads is of great interest to helicopter designers and operators. Rotor thrust is typically increased at a constant power in IGE conditions because of the reduced downwash due to the wake inflow. This is confirmed in Fig. 2.28 that shows the ratio between rotor thrust in IGE and OGE conditions for different distances of the ground given by the results of Light's experiments and by the numerical simulations of the BDM method. Numerical and experimental results are in good agreement and lie close to available semi-empirical analytical models developed in the past [44].

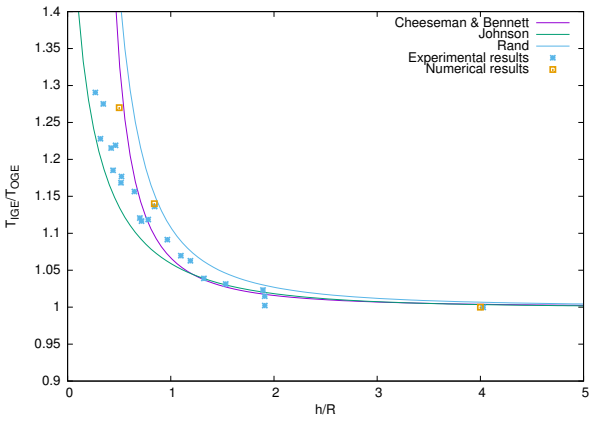

Figure 2.28. Ground effect on rotor thrust.

The influence of ground on required power is also of great interest. However, in this case the proposed solvers are capable of capturing only the component associated to induced drag (namely, due to wake inflow), since it is based on the potential-flow assumption, as stated in Section 2.1, and viscous effects are not taken into account. In addition, it must be noted that, although capable of predicting with good accuracy wake shape near the rotor, because of the difficulty in satisfying the impermeability boundary condition over the ground, the BDM approach is unable to simulate with enough accuracy the wake shape evolution in proximity of it. This negatively affects the evaluation of the velocity induced over the blades by the wake, which is strictly connected to the evaluation of the induced drag and hence of the induced power. Such a drawback does not arise in the MIM approach which, therefore, is that applied for the numerical-experimental correlation of the induced power, C_{P_i}, with the experimental results determined from the figure of merit, FM and the total power, C_P, given in [35] through the relation $C_{P_i} = FM \times C_P$. For the ground plane inclination $\theta_g = 6°$ and a suitable range of variation of the collective pitch, Fig. 2.29 compares the functional relation $C_{P_i}/\sigma \, vs \, C_T/\sigma$ given by the BEM simulations (BEM-MIM approach) and derived by the measurements of Ref. [35] (USNA experiments), with σ denoting the rotor solidity. The numerical-experimental correlation is very good and proves the capability of the computational tool to capture the effect of ground on required power.

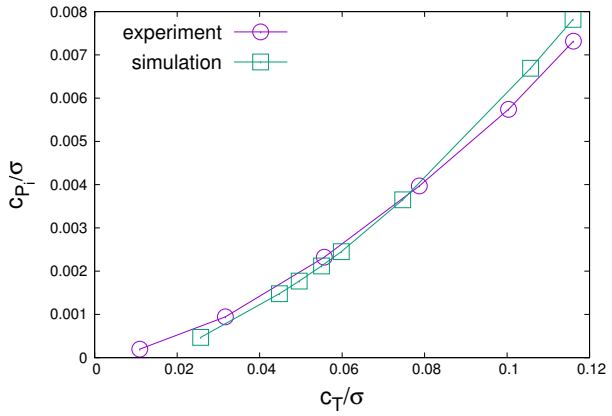

Figure 2.29. C_{P_i}/σ *vs* C_T/σ, for $\theta_g = 6°$.

Chapter 3

Dynamic Wake Inflow Modelling for IGE Rotors

"Il mondo era così recente, che molte cose erano prive di nome e per citarle bisognava indicarle col dito."
G. G. M.

If derived from high-fidelity numerical aerodynamic predictions, [62, 63, 67, 79], a data-based approach may exploit a different way to identify the dynamic inflow models. Furthermore the complex aerodynamic problem, in its whole fully-coupled essence, can be arbitrarily summarized in different low-order finite-state models depending the context in which those models will be adopted.
All the models proposed in this work are linear-time-invariant (LTI), state-space perturbed models and require the preliminary evaluation of the steady reference condition, then the perturbation of the model input variables is performed and the corresponding inflow coefficients evaluated. These models are suited for flight mechanics applications, however it must be recalled that they require the coupling with a static inflow model when implemented within a helicopter flight-dynamics simulation tool. Furthermore, these kinds of approaches (data-based identification) can verify different physics-based simplifying assumption during the identification procedure, allowing a better understand of the behaviour of the wake system. In addition, it is worth noting that in contrast to the analytical approaches, in the case of a low-order model identified from numerical simulation, the ground presence is directly and automatically considered by the aerodynamic simulation. Thus, the proposed identification methodologies will also still be valid in the case of a ground effect helicopter without any procedure modification or mathematical additional operation.
Three different approaches in particular are pointed out in the following, they are completely general and are still valid for each arbitrary high-fidelity aerodynamic solver suited for time-domain perturbation analysis. Those are:

- the first directly relating wake inflow coefficients with rotor degrees of freedom ($\lambda - q$ model) from BEM solver application;

- the second relates, instead, the wake inflow coefficients with rotor air-loads ($\lambda - f$ model) even if the primary inputs of the BEM[1] simulations still are the rotor DOFs;

- the third identifies the wake inflow coefficients to air-loads ($\lambda - \Delta\varphi_{TE}$) relation from the velocity induced over the disk by a vortex lattice representation of the helicopter wake and a 2-D aerodynamic technique is used for the air-loads evaluation.

The last proposed model has been developed to make more computationally efficient the identification process for the ground effect condition, it also allows to decouple and emphasize the role of the vorticity (air-loads) perturbation to the

[1] It is worth reminding in this context the exploiting of Bernoulli's theorem to obtain the pressure distribution over the blade hence the corresponding forces and moments.

blade kinematics in wake inflow dynamic. Specifically, considering the core of the functional dependencies of the wake inflow operator[2], it enables the single and isolated perturbation of each system input variables making it particularly suited for the analysis of the wake-distortion effect on dynamic wake inflow [57].

3.1 Kinematic-based model

The model relates wake inflow coefficients with controls and flight dynamics kinematic degrees of freedom (namely blade pitch controls, hub motion and rigid blade flapping variables). The approximated expression of the wake inflow distribution over the rotor disc, λ_{app}, is expressed by the widely used linear interpolation formula, defined in a non-rotating polar coordinate system, (r_c, ψ).

$$\lambda_{app}(r_c, \psi, t) = \lambda_0(t) + r_c \left(\lambda_s(t)\, \sin\psi + \lambda_c(t)\, cos\psi\right) \tag{3.1}$$

where r_c denotes distance from the disc center, ψ is the azimuth angular distance from the rear blade position, and the coefficients, λ_0, λ_s and λ_c represent, instantaneous mean value, side-to-side gradient and fore-to-aft gradient, respectively.
The identification of the inflow model is a multi-step procedure[62, 63], consisting in:

- application of a high-fidelity aerodynamic solver to evaluate wake inflow corresponding to arbitrary perturbations (*i.e., chirp signal*[3]) of an arbitrary set of DOFs about a steady trimmed flight condition;
- sampling of the transfer functions combining the Z-transform of perturbation and that of inflow coefficients as input and output respectively;
- a rational-matrix approximation, RMA, of the sampled transfer functions in order to obtain the requested state-space model.

Once the wake inflow over the blades corresponding to the performed perturbations about the steady state rotor kinematics variables is determined by the high fidelity aerodynamic solver, input and output signals are windowed and transformed into frequency domain in order to determine the sampled transfer matrix $\mathbf{H}(\omega)$ such that

$$\tilde{\boldsymbol{\lambda}} = \mathbf{H}\tilde{\mathbf{q}} \tag{3.2}$$

[2] $v_i = f_{wake}(\Delta\varphi_{TE}, x_{TE})$ where $\Delta\varphi_{TE}$ in the instantaneous blade vorticity and x_{TE} represents the blade motion.

[3] It is indeed well known how the chirp perturbation, which has the property to explore a wide frequency range with a single time-domain signal, is an efficient way to approach the identification problem [80, 81].

where $\lambda = \{\lambda_0\ \lambda_s\ \lambda_c\}^T$ and $\boldsymbol{q = \{q_v\ q_\Omega\ q_\beta\ q_\theta\}^T}$, with $q_v = \{u\ v\ w\}^T$ and $q_\Omega = \{p\ q\ r\}^T$ collecting, respectively, the hub linear and angular velocities whereas $q_\beta = \{\beta_0\ \beta_s\ \beta_c\}^T$ are the blade flap components, and $q_\theta = \{\theta_0\ \theta_s\ \theta_c\}^T$ the blade pitch controls.
Then, the rational-matrix approximation (RMA) of the following form

$$\mathbf{H}(s) \approx s\,\mathbf{A}_1 + \mathbf{A}_0 + \mathbf{C}\,[s\,\mathbf{I} - \mathbf{A}]^{-1}\,\mathbf{B} \tag{3.3}$$

that provides the best fitting of the sampled **H**-matrix values is determined through a least-square technique [61, 67, 82]. $\mathbf{A}_1, \mathbf{A}_0, \mathbf{B}$ and $\mathbf{C}$ are real, fully populated matrices, whereas $\mathbf{A}$ is a square block-diagonal matrix containing the poles of the approximated transfer functions. Finally transforming back to time domain, the following state-space model is obtained

$$\begin{aligned} \boldsymbol{\lambda} &= \mathbf{A}_1\,\dot{q} + \mathbf{A}_0\,q + \mathbf{C}\,x \\ \dot{x} &= \mathbf{A}\,x + \mathbf{B}\,\mathbf{q} \end{aligned} \tag{3.4}$$

where x is the vector of the additional states representing the wake dynamics effects, whereas matrices $\mathbf{A}_1, \mathbf{A}_0, \mathbf{A}, \mathbf{B}, \mathbf{C}$ are real, fully populated matrices derived from the rational-matrix approximation process. The order of the polynomial part of the transfer function can be evaluated considering the asymptotic behaviour of the system, in a rigorous way at least two high frequencies perturbation input, plus the static gain value, are needed to verify the asymptotic attitude of the system[4].

3.2 Kinematic/loads-based model

Starting from the approach proposed in section 3.19, it is possible to develop an alternative procedure which provides a dynamic inflow model relating the inflow components, λ, to rotor loads perturbations (akin to the well-known Pitt-Peters models). It requires the additional identification of the transfer function matrix, G, between the perturbations of the kinematic input variables, q, and the corresponding rotor loads, f [62, 67]. Let us consider, for instance, blade control pitch perturbations, q_θ, and thrust, roll, and pitch moments, $f = \{C_T, C_L, C_M\}^T$ (note that, for the definition of the $\lambda - f$ inflow model, the number of rotor loads introduced must be at least equal to the number of kinematic variables).
First, akin to the procedure for the $\lambda - f$ model, once wake inflow and rotor loads corresponding to the same chirp-type perturbations of the rotor kinematics variables are determined by the high-fidelity aerodynamic solver, these signals are windowed

[4] In the case of the inflow velocities dependency from the kinematic rotor variable a linear asymptotic behaviour could be found.

and transformed into Z-domain in order to determine frequency samples of the transfer matrices G between the kinematic input variables perturbations and the corresponding rotor loads ($f = \{C_T, C_L, C_M\}^T$).

$$\tilde{f} = \mathbf{G}\tilde{\mathbf{q}} \tag{3.5}$$

Then, by inverting 3.5 and substituting into 3.2 one obtains ([62]):

$$\tilde{\boldsymbol{\lambda}} = \mathbf{H}\mathbf{G}^{-1}\tilde{\boldsymbol{f}} = \hat{\mathbf{H}}^{-1}\tilde{\boldsymbol{f}} \tag{3.6}$$

which is the needed inflow model relating the wake inflow coefficients, λ, to rotor loads perturbations (akin to the well-known Pitt-Peters model). Then, a rational approximation of the resulting transfer matrix $\hat{H}_\theta$ similar to that shown for the $\lambda - q$ model is accomplished, and finally the transformation into time domain yields a LTI, finite-space representation of inflow similar to that in Eq. (3.4), but given in terms of rotor loads, [62, 67], and with the polynomial part removed due to the asymptotic behavior of $\mathbf{G}$:

$$\begin{aligned} \boldsymbol{\lambda} &= \hat{\mathbf{C}}\mathbf{x} \\ \dot{\mathbf{x}} &= \hat{\mathbf{A}}\times + \hat{\mathbf{B}}\mathbf{f} \end{aligned} \tag{3.7}$$

It is worth observing that the imposition $\boldsymbol{A_1} = \boldsymbol{A_0} = \mathbf{0}$ yields a $\lambda - f$ inflow model that is fully equivalent to the Pitt and Peters one. Furthermore, as stated before, starting from it a relation between inflow and rotor thrust, roll and pitching moment coefficients ($\{C_T, C_L, C_M\}$), similarly to the Pitt and Peters' model [16, 52], could be found.

3.3 Vorticity Model

It is worth noting that, by applying the approach presented in section 3.2, equivalent, but different, inflow models relating inflow states and air-loads inputs can be obtained starting from each corresponding different triplet of kinematic DOFs considered in $\lambda - q$ model. As argued by Gennaretti et al. in [67], this is due to the fact that different kinematic perturbations could result in the same vorticity perturbation distribution and, hence, in the same induced velocity. Furthermore in this research has been found that the ground effect simulation is characterized to an high level of numerical noise in the velocity signals which severely affects the coherence of the input-output relation. To avoid the above discussed issues and in order to make less time-consuming each simulation, a different approach is proposed in the following.

In order to create a generic model for dynamic inflow that is independent of a specific set of rotor and control system characteristic, the idea is to directly evaluate the relation between an arbitrary vorticity perturbation and its relative velocity. Indeed, considering what inflow is (see for instance appendix B), recalling the Biot-Savart law which is used to evaluate the velocity field induced by the vortex net representing the wake and considering its functional dependencies, $\vec{v} = f(\Delta\varphi_{TE}, x_{TE})$, it is clear that the vorticity is the main ingredient of the wake inflow.
First, similar to the Pitt-Peters model [16], the proposed modeling approach represents the perturbed wake inflow distribution over the rotor disc through the following expression in a non-rotating polar coordinate system, (r, ψ),

$$\lambda(r, \psi, t) = \lambda_0(t) + r\,[\lambda_s(t)\,\sin\psi + \lambda_c(t)\,cos\psi] \tag{3.8}$$

where r denotes distance from the disc centre, ψ is the azimuth angular distance from the aft position and the coefficients λ_0, λ_s and λ_c, represent respectively, instantaneous mean value, side-to-side and fore-to-aft gradients.
The perturbation inflow coefficients are assumed to be related to perturbation rotor thrust, roll and pitch moments (C_T, C_L, C_M), and to rotor kinematic motion (x_{TE}), through a state-space model, namely,

$$\dot{\boldsymbol{x}} = \boldsymbol{A}\boldsymbol{x} + \boldsymbol{B}\boldsymbol{u} \tag{3.9}$$

where $u = \{C_T, C_L, C_M, x_{TE}\}^T$ and x is such that

$$\boldsymbol{\lambda} = \begin{Bmatrix} \lambda_0 \\ \lambda_s \\ \lambda_c \end{Bmatrix} = \boldsymbol{C}\boldsymbol{x} \tag{3.10}$$

These coefficients are extracted through the following multi-step methodology:

- starting from a trimmed steady-state solution, input perturbations of both vorticity released at the trailing edge of the blades and rotor motion are introduced (*i.e., chirp-type and multi-step input*);
- the corresponding wake inflow on rotor blades is evaluated by free-wake, vortex-lattice simulations;
- the corresponding aerodynamic loads are evaluated[5];
- the transfer functions between rotor loads/motion and inflow coefficients are identified;

[5]The loads evaluation is a crucial issue of this methodologies and it will be treated in the following.

- the rational matrix approximation (RMA) of transfer functions and the transformation back into time-domain yield the state-space dynamic model of the inflow coefficients.

Once determined, the reference condition, arbitrary perturbations of the trailing edge vorticity could be applied to the rotor model in order to obtain the corresponding wake inflow distribution over the blades. This is made possible by an adaptation of the aerodynamic solver of Section 2.2. Mainly, for ground effect condition as well as for out of ground one, the BEM body contribution of equation 2.4 has been neglected. The effects of the body induced velocity field in free-wake solution, that could be restricted to the wake particles which directly interact with the blade, could also be neglected for these applications without losing of accuracy. In figure 3.1 a comparison between the wake induced velocity distribution over the blade evaluated with the BEM aerodynamic code, complete rotor configuration, and for the vortex-lattice-method (VLM) is proposed, a good agreement between the two distributions could be noticed in particular considering the big amount of saved time for the simulation with respect to the BEM solver.

Once the perturbed inflow (difference between actual inflow and reference steady-

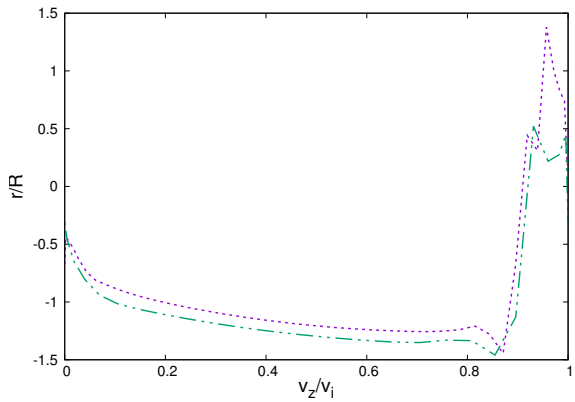

Figure 3.1. Induced velocity distribution over the blade, rotor in hovering out of ground effect. - · - · - vortex-lattice-method, VLM; ··· boundary-element-method, BEM. The inflow distributions are referred to the blade of the rotor of table 4.1 presented in the following chapter.

state one) is evaluated in response to perturbations of bound vorticity and rotor pitch and roll motion, λ_0, λ_s and λ_c perturbation time histories are determined. To this purpose, the distribution of the perturbed bound vortex circulation, $\Delta\varphi$, is modeled through the following first-order approximation

$$\Delta\varphi(r,t) = r[\Delta\varphi^0(t) + \Delta\varphi^s(t)\ \sin\psi + \Delta\varphi^c(t)\, cos\psi] \tag{3.11}$$

where $\Delta\varphi^0$, $\Delta\varphi_s$ and $\Delta\varphi_c$ are the instantaneous mean value, side-to-side and for-to-aft gradients, respectively. In the preceding equation a linear distribution of the perturbed vorticity is considered. As stated at the beginning of this section, different kinematic perturbations may produce the same perturbed vorticity, indeed, this assumption is representative of a blade pitch angle variation (which in a rotating blade corresponds to a linear lift hence vorticity variation) as well as of a blade flapping motion. However, other kind of distributions could be chosen considering combinations of different shape functions. Obviously, this should be followed by a corresponding extension of the coefficient-base representation in order to represent a more general inflow distribution, [63].

A crucial issue of the proposed methodology is the rotor air-loads evaluation. In the $\lambda - f$ model the loads are directly evaluated by applying the Bernoulli theorem (written in terms of velocity potential and wake induced velocity [70]) and they are given as outputs by the BEM solver. Differently, this approach requests the knowledge of a relationship connecting the blade trailing edge vorticity with the forces and moments acting over the rotor hub.

The key point may be better understood considering the following: in the description of the $\lambda - f$ model, in the useful Laplace-domain[6], the relation between the inflow coefficients and the corresponding air-loads is obtained by inverting the function that gives the forces in terms of the kinematic inputs and combining it with the inflow/kinematic-DOFs function (equation 3.6). In a similar way, the development of this vorticity/inflow model requires something that relates the inputs (air-loads) with the outputs (inflow coefficients), in the frequency-domain:

$$\begin{cases} \tilde{\lambda} = & h(s)\Delta\tilde{\varphi}_{TE} \\ \tilde{f} = & g(s)\Delta\tilde{\varphi}_{TE} \end{cases} \tag{3.12}$$

with $g(s)$ such that

$$\hat{h}(s) = h(s)g(s)^{-1} \text{ and } \tilde{\lambda} = \hat{h}(s)\tilde{f} \tag{3.13}$$

Various aerodynamic theories can be exploited to relate the vorticity with the loads hence the function $g(s)$ may consequently assume many forms depending on the desired model accuracy. In appendix D, analogously with the well-know lift deficiency function, the extraction of this vorticity/loads transfer function is proposed starting from Theodorsen's theory.

However, in this work the most simple theory is applied in order to first assess the effective practicability of the model, thus the Glauert section load formula over the span of the blades yields the following one-to-one relation between $\Delta\varphi$ coefficients

[6] Frequency-domain transfer functions that relate the inflow distribution coefficients with the rotor air-loads.

and rotor load components, $\{C_T, C_L, C_M\}$,

$$\begin{aligned} C_T &= \sum_{j=1}^{N} \int_{e_h}^{1} \frac{1}{\pi\Omega R^2}\, \bar{r}\, \Delta\varphi(\bar{r},t)\, d\bar{r} \;=\; \frac{N\Delta\varphi^0(t)}{\pi\Omega R^2} \frac{\bar{r}^3}{3}\Big|_{e_h}^{1} \\ C_L &= \sum_{j=1}^{N} \int_{e_h}^{1} \frac{1}{\pi\Omega R^2}\, \bar{r}^2\, \sin\psi_j\, \Delta\varphi(\bar{r},t) d\bar{r} \;=\; \frac{N\Delta\varphi^s(t)}{2\pi\Omega R} \frac{\bar{r}^4}{4}\Big|_{e_h}^{1} \\ C_M &= \sum_{j=1}^{N} \int_{e_h}^{1} \frac{1}{\pi\Omega R^2}\, \bar{r}^2\, cos\psi_j\, \Delta\varphi(\bar{r},t)\, d\bar{r} \;=\; \frac{N\Delta\varphi^c(t)}{2\pi\Omega R} \frac{\bar{r}^4}{4}\Big|_{e_h}^{1} \end{aligned} \tag{3.14}$$

where e_h is the nondimensional root-cut-off, N is the number of blades and $\bar{r}$ denotes the nondimensional radial coordinate, Ω the rotor angular velocity and R the rotor radius. Namely the $g(s)$ function assumes the role of a static gain $\bar{g}$ which for an hovering rotor is such that

$$\tilde{f} = \begin{vmatrix} g_{C_T} & 0 & 0 \\ 0 & g_{C_L} & 0 \\ 0 & 0 & g_{C_M} \end{vmatrix} \begin{Bmatrix} \Delta\varphi^0 \\ \Delta\varphi^s \\ \Delta\varphi^c \end{Bmatrix} = \begin{Bmatrix} C_T \\ C_L \\ C_M \end{Bmatrix} \tag{3.15}$$

On the contrary, considering the decoupling aim of this model, the rotor kinematic inputs x_{TE} are directly related to the inflow coefficients[7] and the corresponding transfer functions can be identified. The first application of this features of the model will be the identification of the roll and pitch angular rate (p, q) effects on the dynamic inflow indeed, it is well known they play an important role in the off-axis response of a helicopter control inputs and characterized by a first-order behaviour with time, [57, 59].

The last step of the identification process is performed within the framework of the *Matlab system identification toolbox*, [83, 84], which allows the direct identification of the state-space matrix coefficients necessary for the system representation exploiting time-domain-based identification algorithm. At this point, in order to make the process more efficient and accurate, especially when applied to ground effect noisy signals, some considerations are needed to limit as much as possible the number of the variables involved in the identification process. Thus, considering some proven evidences about the physical link between input and output variables in dynamic inflow modeling, and, corroborating such considerations with the analysis of the coherence of each I/O sampled relation (shown in figures 4.13 and 4.15), the approximation has been "guided" by including a number of poles and zeros that is in accordance with the extended Pitt-Peters theory [58, 27], the coherence showed in Section 4.2 confirms this hypothesis.

[7] Their direct effect on blade aerodynamic forces is neglected, the blade motion is perturbed without changing the vorticity reference distribution.

Literally, for hovering out-of-ground-effect and in-parallel-ground-effect conditions, the degrees of numerator and denominator polynomials of the transfer function rational approximations are as indicated in the following table (considering also the (p, q) inputs just for the sake of completeness)

	C_T	C_L	C_M	p	q
λ_0	$0^Z/1^P$	null	null	null	null
λ_s	null	$0^Z/1^P$	null	$0^Z/1^P$	null
λ_c	null	null	$0^Z/1^P$	null	$0^Z/1^P$

Table 3.1. Zeros/Poles for the low-order $\lambda - \mathbf{f}$ dynamic inflow model for hovering rotor out of ground effect and in ground effect over a parallel-to-disc surface.

whereas for in-**inclined**-ground-effect conditions become

	C_T	C_L	C_M	p	q
λ_0	$1^Z/2^P$	null	$0^Z/2^P$	null	$0^Z/2^P$
λ_s	null	$0^Z/1^P$	null	$0^Z/1^P$	null
λ_c	$0^Z/2^P$	null	$1^Z/2^P$	null	$1^Z/2^P$

Table 3.2. Zeros/Poles for the low-order $\lambda - \mathbf{f}$ dynamic inflow model for hovering rotor in ground effect over a non-parallel-to-disc surface.

The different assumption of Tab. 3.2 with respect to the one in Tab. 3.1 derives from the consideration that, differently from the parallel-ground case, the inclined ground induces a fore-aft wake distortion similar to that caused by forward flight[21] which, in turn, causes coupling between λ_0 and λ_c coefficients (e.g. through the L_{13} and L_{31} coefficient of the Pitt-Peters model [52]), instead, the λ_s coefficient remains almost uncoupled from the other two. As a proof of the effect of inclined ground on the inflow longitudinal distribution, figure 2.27 shows the wake induced velocity distribution in the xz-plane ($\psi = 0$, $\psi = 180°$) for the two-bladed rotor, used for the validation of Section 2.3 and for different inclination ground angles (ranging from $\theta_g = 0°$ to $\theta_g = 30°$). It can be easily noted that, as θ_g increases, the wake induced velocity decreases on the uphill-side (left side of the plot) and increases in the downhill-side.

In conclusion it is worth noting that, although the hypotheses made on the transfer functions matrix structure may hide the effects of some high-fidelity aerodynamic phenomena, they make the identification process more effective and robust, main-

taining at the same time a good accuracy of the identified model, as they include the most relevant dynamic behaviours of the wake inflow, in particular for flight dynamic and control design purposes.

Chapter 4

Dynamic Inflow Modelling Applications

"La bellezza sarà convulsa o non sarà"
A. B.

In this chapter the numerical results of the identification techniques outlined in Chapter 3 are presented. First the different dynamic inflow models are extracted from the aerodynamic simulation and the prediction capability verified by comparing the predicted inflow coefficients with the corresponding ones obtained through the high-fidelity simulation (*i.e.:* BEM simulation) after an arbitrary input perturbation. Three different identification techniques are applied and the resulting inflow models are shown and discussed. The different characteristics of the proposed identification procedures, and the corresponding inflow modelling, are exploited to extract the dynamic wake inflow models for various hovering operative conditions. Three heights from the ground and three different ground angle were simulated, the effect of the ground presence successfully considered in the identified wake inflow models. Then the reduced-order models were implemented in the in-house helicopter flight dynamic simulation tool *Helistab*[1]. A typical analysis was performed, the global transfer functions relating the pilot control inputs with the rigid motion of the whole machine are compared for different flight condition and the effect of the ground on both the dynamic behaviour and the stability analysis are briefly discussed.

Figure 4.1. Messerschmitt-Bölkow-Blohm Bo-105 in SAR (Search And Rescue) configuration.

The considered test case is a mid-weight helicopter inspired by the Bo-105 (Fig.4.1), whose main data are reported in 4.1, and the considered flight conditions are:

- hovering out-of-ground-effect, HOGE, baseline results;

[1]The tool was developed in the past inside the ARISTOTEL european research project, ([64]).

- hovering in-of-ground-effect above a parallel-to-disc ground, HIGE, with an inclination angle of $\theta_g = 0°$, for three different height to the ground $h_g/R =$ (0.6, 0.75, 1.0);

- hovering in-of-ground-effect above a inclined-to-disc ground, HIGE, with an inclination angle of $\theta_g = (15°, 30°)$, for two different height to the ground $h_g/R = (0.75, 1.0)$.

$mass$	2200	kg
I_{xx}	1430	$kg\,m^2$
I_{yy}	4975	$kg\,m^2$
I_{zz}	4100	$kg\,m^2$
I_{xz}	650	$kg\,m^2$
MR type	hingeless	-
MR radius	4.91	m
MR chord	0.27	m
MR angular speed	44.4	rad/s
MR blade twist	-8	$\circ/m$
MR number of blades	4	-
TR radius	1	m
TR chord	0.2	m
TR angular speed	230	rad/s
TR number of blades	2	-

Table 4.1. Main helicopter data.

All the following results were obtained for the same rotor configuration.

It is worth noting that the kinematics perturbation of the rotor degrees of freedom are restricted to the principal blade kinematic inputs (θ_0, θ_s, θ_c) for all presented approaches, which directly correspond with the (C_T, C_L, C_M) inputs both the $\lambda - f$ and $\lambda - \Delta\varphi$ models. Specifically, applying the vorticity model, the evaluation of the kinematic inputs (roll and pitch angular rate in particular strongly affect helicopter flight dynamics) has shown unexpected and still unsolved numerical burdens. The assessment of the inflow/roll-pitch rate relation listed as one of the first future development of this work.

4.1 Kinematic-Based Model

The MIM method (Section 2.1.2) is applied to determine the $\lambda - q$ and $\lambda - f$ finite-state dynamic inflow models in ground effect. The two models are identified after chirp-type small perturbations of collective and cyclic pitch controls, $\mathbf{q}_\theta$, about a parallel-to-ground hovering reference flight condition, the frequency range of the analysis is limited to 18.0 rad/s for computational opportunities. It is however beyond the upper limit for the flight dynamics applications.
Transfer functions identification and rational approximation, as well as validation of the finite-state dynamic inflow against BEM predictions for arbitrary time-varying pitch controls are presented in the following.

4.1.1 $\lambda - q$ Transfer functions

First, the sampled values of the direct (and most relevant) transfer functions of the $\lambda - q$ model are compared to the corresponding RMA[2], for the HOGE condition and the HIGE conditions with $h_g/R = 1$ and $h_g/R = 0.6$. Specifically, figure 4.2 depicts the identified and approximated transfer functions λ_0 *Vs.* θ_0, whereas Figure 4.3 shows the transfer functions λ_c *Vs.* θ_c (it is worth noting that, for symmetry reasons, the latter coincides with λ_s *Vs.* θ_s).
For these transfer functions, a quite good accuracy of the rational approximation is achieved by the introduction of 5 poles. Note that, the shape of the cyclic transfer function is not appreciably altered by variation of the distance from the ground, whereas for the collective transfer function the effects of a high-frequency pole grow with the reduction of h_g/R. Furthermore, it is interesting to observe that the effect of the ground on the inflow amplitude does not change monotonically with the distance h_g/R, but it is greater for $h_g/R = 1$ than for $h_g/R = 0.6$ (note that, the collective pitch is kept constant).
Next, the two off-diagonal transfer functions, λ_0 *Vs.* θ_c and λ_c *Vs.* θ_s, of the identified matrix $\mathbf{H}_\theta$ are depicted in figures 4.4 and 4.5, respectively. As expected, these transfer functions are less relevant (much smaller amplitude) than the diagonal (direct) ones of figures 4.2 and 4.3, and this induces less accurate rational form approximations[3]. However, it is interesting to note that, the cross-coupling effects represented by the off-diagonal transfer functions are increased in HIGE conditions, proportionally to the reduction of the rotor-ground distance.

[2] Rational-Matrix-Approximation

[3] Indeed, the most relevant transfer functions are those better captured by the the least-square RMA procedure, when the best compromise between accuracy and low number of introduced additional states is pursued.

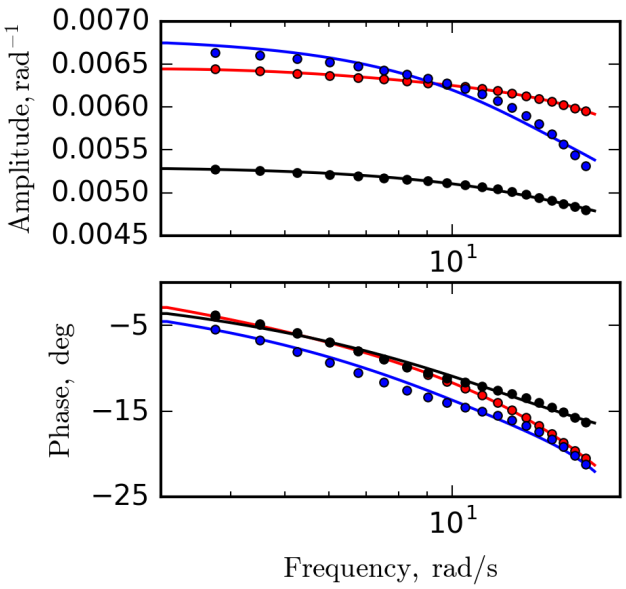

Figure 4.2. Identified transfer function λ_0 *Vs.* θ_0. — RMA HOGE; — RMA $h_g/R = 1$; — RMA $h_g/R = 0.6$; • samples.

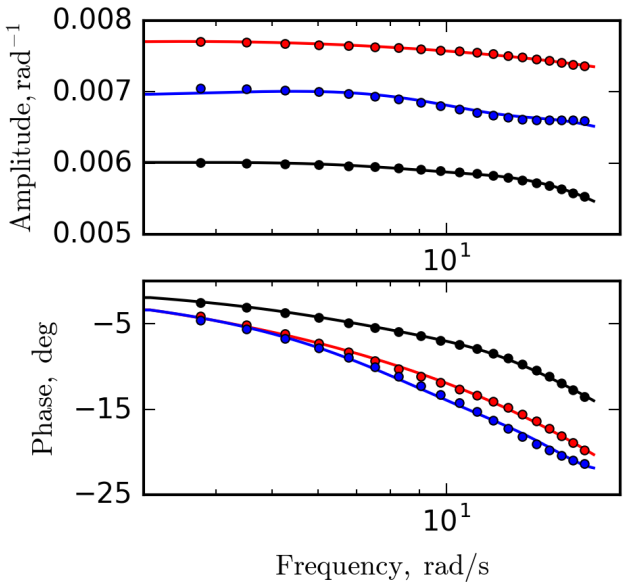

Figure 4.3. Identified transfer function λ_c *Vs.* θ_c. — RMA HOGE; — RMA $h_g/R = 1$; — RMA $h_g/R = 0.6$; • samples.

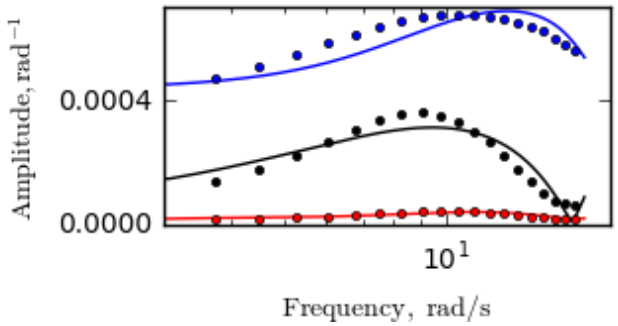

Figure 4.4. Identified transfer function λ_0 *Vs.* θ_c. — RMA HOGE; — RMA $h_g/R = 1$; — RMA $h_g/R = 0.6$; • samples.

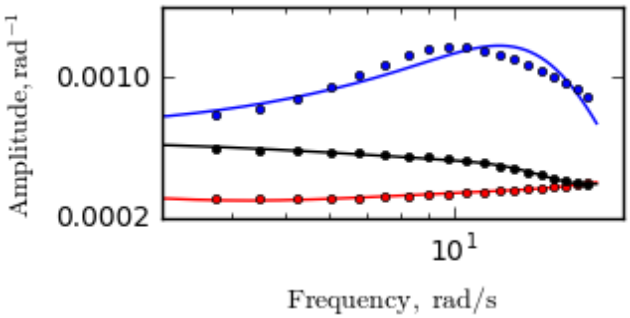

Figure 4.5. Identified transfer function λ_c *Vs.* θ_s. — RMA HOGE; — RMA $h_g/R = 1$; — RMA $h_g/R = 0.6$; • samples.

4.1.2 $\lambda - f$ Transfer functions

Observing the transfer functions of the matrix $\hat{\mathbf{H}}_\theta$, relating the inflow coefficients to the aerodynamic hub load, the first difference appearing with respect to those of the matrix $\mathbf{H}$ is that the diagonal (direct) transfer functions are much more dominant with respect to the off-diagonal ones. Thus confirming the considerations done in Section 3.3 about the dependencies of the inflow coefficients from the rotor air-loads, nevertheless it is confirmed that HIGE produces an increase of the cross-coupling terms.

Figures 4.6 and 4.7, instead, depict respectively identified and approximated transfer functions λ_0 *Vs.* C_T and λ_c *Vs.* C_M (also in this case, for symmetry reasons, the latter coincides with λ_s *Vs.* C_L). For these transfer functions, a quite good accuracy of the rational approximation is obtained by using 3 poles for the HOGE case and for $h_g/R = 0.6$, whereas 4 poles are used for the case $h_g/R = 1$. It is worth noting that for the parallel ground condition, as pointed out in Section 3.3 about the number of poles characterizing the ground-affected dynamic inflow systems (see table 3.2),

the analytical derivation of the inflow models (characterized by only three poles as in HOGE case) is a not so far from the simulated results, [19]. The shape of both collective and cyclic inflow transfer functions is not altered appreciably by variation of the distance from the ground which, however, significantly affects their amplitude, although not monotonically, like for the $\lambda - q$ model direct transfer functions.

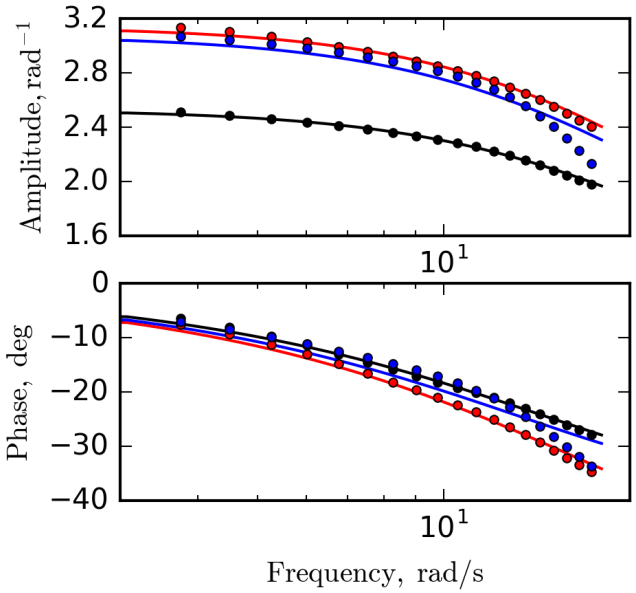

Figure 4.6. Identified transfer function λ_0 *Vs.* C_T. — RMA HOGE; — RMA $h_g/R = 1$; — RMA $h_g/R = 0.6$; • samples.

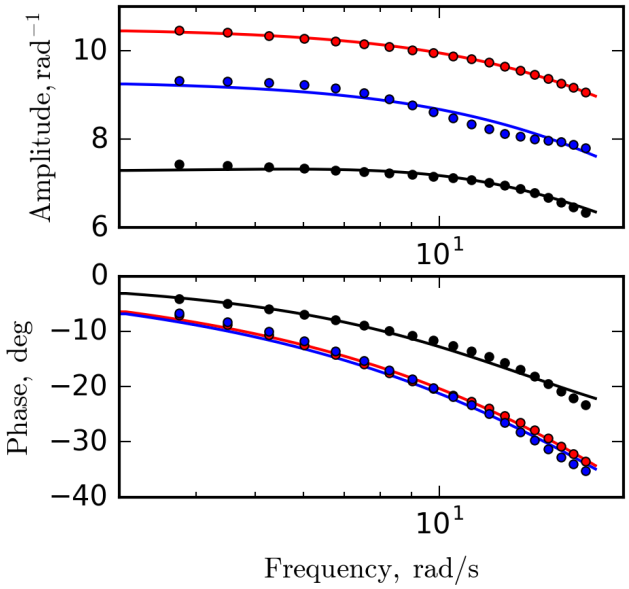

Figure 4.7. Identified transfer function λ_c *Vs.* C_M. — RMA HOGE; — RMA $h_g/R = 1$; — RMA $h_g/R = 0.6$; • samples.

4.1.3 Time response validation

The dynamic inflow models determined from the RMA of $\mathbf{H}_\theta$ and $\hat{\mathbf{H}}_\theta$ are finally validated by comparing their predictions with the data directly provided by the BEM-MIM solver, for the following arbitrary small perturbation of the collective pitch (expressed in degrees).

$$\theta_0(t) = cos(0.1\,\Omega\,t)\sin(0.3\,\Omega\,t)\; e^{-0.25\,t}$$

First, the HOGE case is examined in figures 4.8 and 4.9, which depict the λ_0 responses evaluated through the $\lambda - q$ and $\lambda - f$ models, respectively. Note that, the input to the $\lambda - f$ model is derived from the rotor loads determined by the BEM response to θ_0.

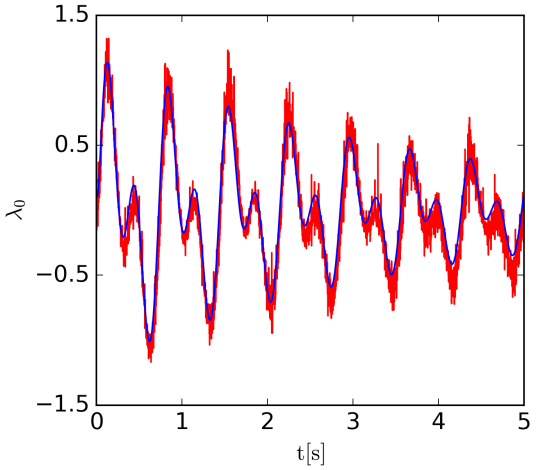

Figure 4.8. λ_0 response to θ_0 in HOGE condition: comparison between BEM and $\lambda - q$ model predictions. BEM; $\lambda - q$ model.

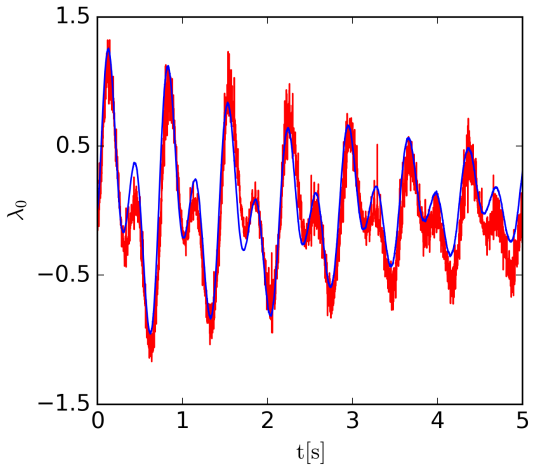

Figure 4.9. λ_0 response to $C_T(\theta_0)$ in HOGE condition: comparison between BEM and $\lambda - f$ model predictions. BEM; $\lambda - f$ model.

BEM-MIM solution and dynamic inflow model results are in good agreement in both cases, with the un-captured irregular very high frequency content observed in the BEM prediction that is due to numerical issues of the free-wake solution emerging when hovering conditions are examined (and whose simulation is not required). Next, the HIGE condition for $h_g/R = 1$ is considered, and the corresponding λ_0 responses are shown in figures 4.10 and 4.11.

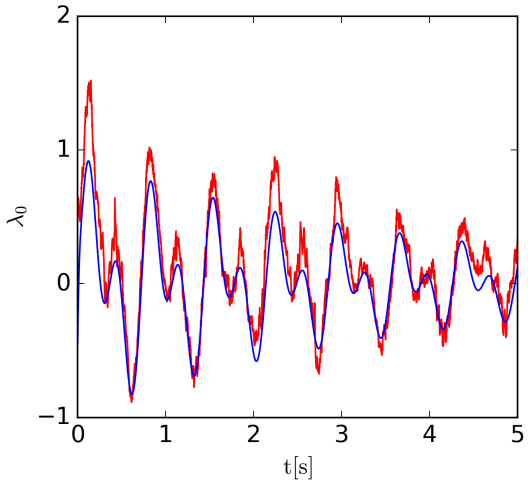

Figure 4.10. λ_0 response to θ_0 in HIGE condition, $h_g/R = 1$: comparison between BEM and $\lambda - q$ model predictions. BEM; $\lambda - q$ model.

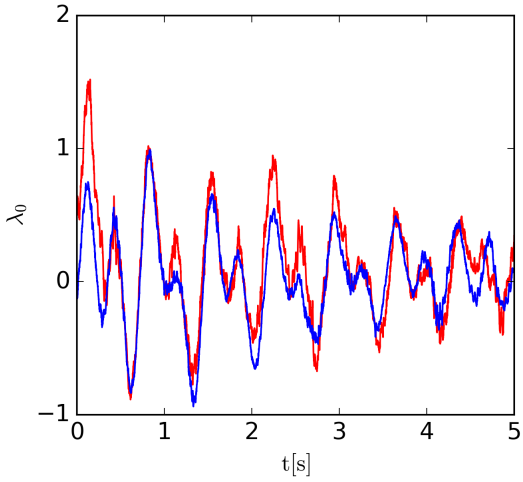

Figure 4.11. λ_0 response to $C_T(\theta_0)$ in HIGE condition, $h_g/R = 1$: comparison between BEM and $\lambda - f$ model predictions. BEM; $\lambda - f$ model.

In these cases, the BEM predictions fairly well correlate with the two dynamic inflow models which are able to capture the main features of the λ_0 response, although the presence of the ground increases irregularities of the numerical solution and degrades the quality of the correlations. Note that, the higher frequency content of the $\lambda - f$ model prediction directly derives from the rotor loads given by the BEM solver and used as inputs to the finite-state representation. The capability of the $\lambda - q$ model to capture the ground effects on the λ_0 response is highlighted in Figure 4.12 which presents the comparison between HOGE and HIGE responses

given by both the BEM solver (upper picture) and the dynamic inflow model (lower picture). Except for the high-frequency irregularities, the differences between HOGE and HIGE predictions by the two simulation tools are very similar.

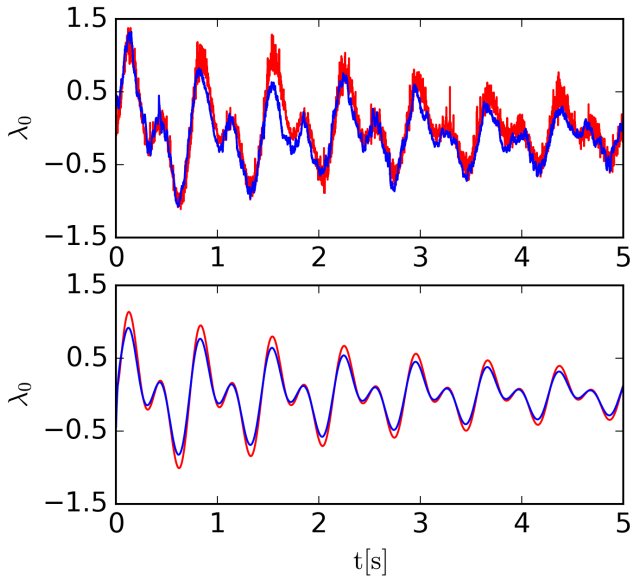

Figure 4.12. λ_0 response to $C_T(\theta_0)$ from BEM (upper) and $\lambda - q$ model (lower) predictions. HOGE; HIGE for $h_g/R = 1$.

4.2 Vorticity-based Model

Due to the more computational efficiency of the vorticity-based model of Section 3.3, in this case, differently from the kinematic-based model, the frequency range of the analysis is extended over the 1st/Rev (44.4 rad/s), which is well beyond the upper limit for flight dynamics applications.

Two different rotor heights from the ground, $h/R = 0.75$ and $h/R = 1$, are analyzed and compared at three different inclination angles $\theta_g = (0°, 15°, 30°)$, arbitrary sequences of unitary step perturb the inputs of system in the time-domain, the identification is carried out within the **Matlab Identification ToolBox** and Bode diagram of the identified transfer functions and time-marching validation analysis are presented.

Figures 4.13 and 4.15 show the mean coherence, averaged also over equal but separate simulations for each configuration, of the output signals for all the corresponding inputs. The mean value in this context has to be sought just like a preliminary indicator of the expected accuracy of the sampled transfer function, the data are

not filtered or pre-processed before the coherence is analyzed. A threshold value for a coherence analysis, if applied to system identification and recalling that is a measure of the only linear part of the signal, is proposed by Remple and Tischler in [80]. Here they stated that the coherence of the frequency response has to be more than 0.6, considering this but looking at the time-marching validation as the only final accuracy-test for the identified model, the following figures are also useful and used to verify the consistency of the hypothesis of tables 3.2 and 3.1.

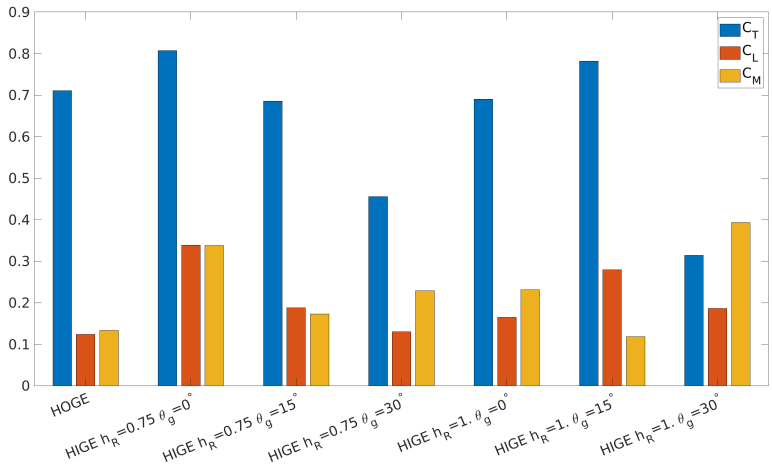

Figure 4.13. Input-output coherence of the output signals, mean inflow coefficient (λ_0) *Vs.* system inputs.

Figure 4.13 depict the coherence for the λ_0 output, one of the main visible effect of the ground is the general lower coherence of the I/O relationship, furthermore as the ground angle becomes bigger the lower is the coherence as well the gap between different inputs/λ_0 bars. This is due to the increasing in the numerical instabilities of the wake structure during the simulation, those instabilities and uncertainties are also the reason of the high-frequency higher content in the in-ground-effect signal in particular for inclined condition, see figure 4.14.

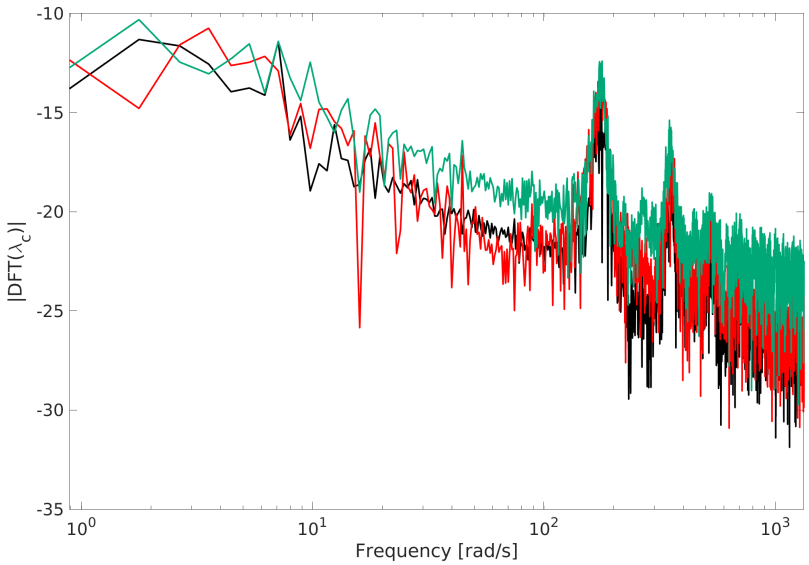

Figure 4.14. Data spectra of λ_c perturbed signal: HOGE ——— ; HIGE: ——— $\theta_g = 0°$; ——— $\theta_g = 30°$.

Looking at the HOGE case and considering also the results of figure 4.15, the simplified assumptions in the I/O dependencies proposed in the literature are totally confirmed and reasonable, hence, even if the ground case generally does not show a clear dominance of one input over the others for the λ_c and λ_s dependencies, in this work, the identification has been forced towards a sort of hybrid model which follows the analytical considerations derived from the conservation law application. This approach could hide some dynamic coupling or cross-coupling of the system, but, it has been experimented with the kinematic-based approach (Sec.4.1) how these effects are strongly affected by numerical uncertainties and, consequently, lead to unphysical transfer functions. In the dearth of public experimental flight data concerning those conditions, the simplifications proposed in Section 3.3 has the great advantage to avoid the identification of numerical misleading coupling transfer function and, moreover, makes the whole procedure very faster. Once again the time-marching validation test will be clarifying of the accuracy of the identified model.

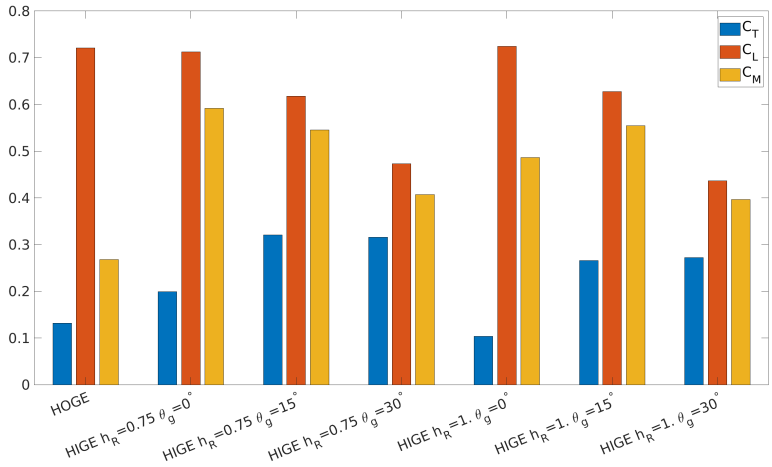

(a) λ_s

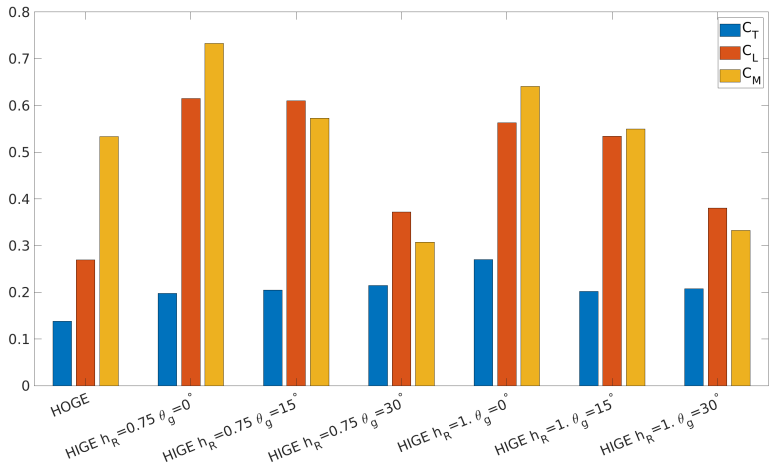

(b) λ_c

Figure 4.15. Input-output coherence of the output signals, lateral and longitudinal inflow coefficients (λ_s, λ_c) *Vs.* system inputs.

In the following, the main elements of the transfer functions matrix are presented and discussed, a comparison is also performed with the well-known Pitt-Peters (PP) model. First in table 4.2 and figure 4.16 the numerical transfer function (HOGE and HIGE) between C_T and λ_0 and the location of its poles and zeros are shown and compared with those predicted by the Pitt-Peters model (PP) in out-of-ground-effect condition. In the left-side of the figure the transfer functions for $h/R = 0.75$ are reported whereas the right-side figure is about $h/R = 1$ simulation.

Case	poles [rad/s]	zeros [rad/s]
PP	-8.3	-
HOGE	-11.1	-
HIGE | $h/R = 0.75$ | $\theta_g = 0°$	-10.1	-
HIGE | $h/R = 0.75$ | $\theta_g = 15°$	-5.7, -21.9	-6.4
HIGE | $h/R = 0.75$ | $\theta_g = 30°$	-0.53 $\pm i$ 8.4	750.
HIGE | $h/R = 1$ | $\theta_g = 0°$	-12.5	-
HIGE | $h/R = 1$ | $\theta_g = 15°$	-4.9, -27.4	-16.4
HIGE | $h/R = 1$ | $\theta_g = 30°$	-0.5, -75.1	17.4

Table 4.2. Poles and zeros location of the C_T *Vs.* λ_0 transfer function: comparison between numerical data and Pitt-Peters analytic model.

With respect to PP, the numerical HOGE transfer function surprisingly presents a more damped pole, and then a significantly shorter time constant. The ground presence seems also to have more damped poles, in particular the parallel $h/R = 1$ case presents a pole which is more damped than the HOGE case, the static gains are quite different. Note that, for this particular transfer function, the Pitt-Peters model is known to be strongly dependent on the loads distribution along the blade span [85].

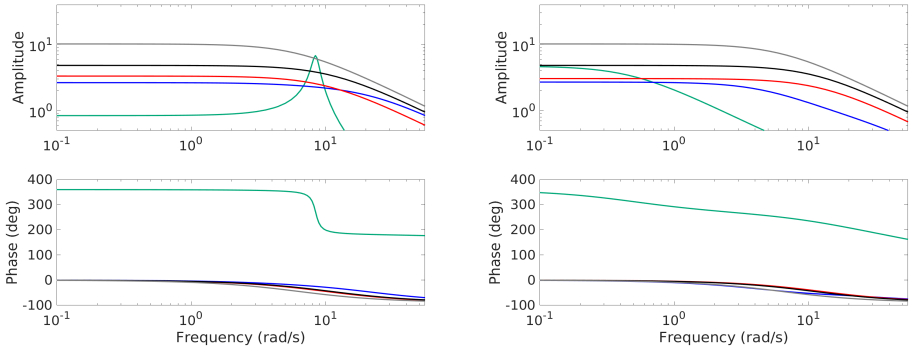

(a) $h/R = 0.75$ (b) $h/R = 1$

Figure 4.16. Magnitude and phase of C_T *Vs.* λ_0 transfer function: comparison between numerical data. Pitt-Peters ——; HOGE ——— ; HIGE: ——— $\theta_g = 0°$; ——— $\theta_g = 15°$; ——— $\theta_g = 30°$.

Concerning the effects of the ground it is evident that the ground increases

the damping of the pole and slightly reduces the static gain (parallel ground in particular). Furthermore, the transfer functions with inclined- ($\theta_g = 15°$) and parallel-ground have very similar behaviour in the frequency range of interest, even if the approximation process gives a quite different polynomial form, due to the different hypotheses on zeros and poles made in 3.1 with respect to 3.2. This result suggests the possibility of using one pole and no zeros to approximate this transfer function also in inclined-ground conditions. Clearly the particular low-coherence of the $\theta_g = 30°$ ($h/R = 1$ the worst) configuration may affect the quality of the identified transfer function and only the subsequent time-marching validation may quantify the prediction capability of the model. Note that the phase difference at the near-zero frequency is of 360° hence no significant differences are in the system phase response.
Then, table 4.3 and figure 4.17 present the results concerning the C_L *Vs.* λ_s relation. Also in this case, the following considerations may be drawn:

- in out-of-ground effect conditions, the numerically identified transfer function show a smaller pole than the analytic Pitt-Peters' model. However, the transfer functions predicted by the two models present a difference in static gains with the PP one higher than the simulation-based one;

- the presence of the ground generally reduces damping but retaining a very similar static gain;

- the inclination angle does not affect too much the λ_s coefficient as expected by the parallelism between the ground rotation axis and the $\Psi_{blade} = 90° - 180°$ rotor oriented direction.

Case	poles	zeros [rad/s]
PP	-19.4	-
HOGE	-11.2	-
HIGE | $h/R = 0.75$ | $\theta_g = 0°$	-16.2	-
HIGE | $h/R = 0.75$ | $\theta_g = 15°$	-26.6	-
HIGE | $h/R = 0.75$ | $\theta_g = 30°$	-9.3	-
HIGE | $h/R = 1$ | $\theta_g = 0°$	-5.5	-
HIGE | $h/R = 1$ | $\theta_g = 15°$	-9.5	-
HIGE | $h/R = 1$ | $\theta_g = 30°$	-3.6	-

Table 4.3. Poles and zeros location of the C_L *Vs.* λ_s transfer function: comparison between numerical data and Pitt-Peters analytic model.

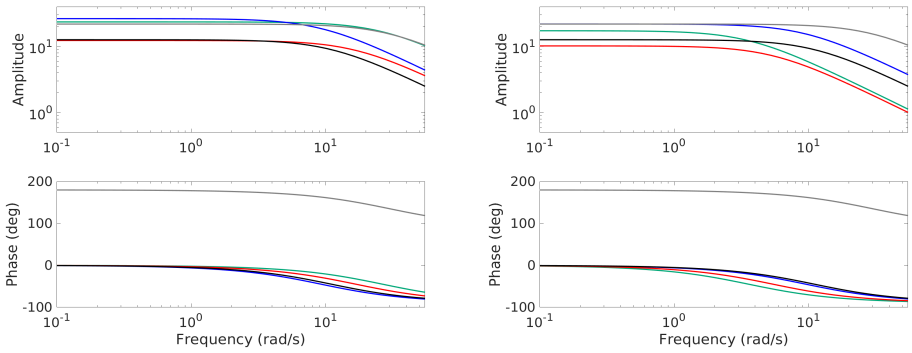

(a) $h/R = 0.75$ (b) $h/R = 1$

Figure 4.17. Magnitude and phase of C_L *Vs.* λ_s transfer function: comparison between numerical data. Pitt-Peters ——; HOGE —— ; HIGE: —— $\theta_g = 0°$; —— $\theta_g = 15°$; —— $\theta_g = 30°$.

Next, table 4.4 and figure 4.18 present the results regarding the C_M *Vs.* λ_c transfer function.

Case	poles	zeros [rad/s]
PP	-19.4	-
HOGE	-12.2	-
HIGE | $h/R = 0.75$ | $\theta_g = 0°$	-17.4	-
HIGE | $h/R = 0.75$ | $\theta_g = 15°$	-2.6 $\pm i$5.8	-2.1
HIGE | $h/R = 0.75$ | $\theta_g = 30°$	-2.1, -9.15	0.6
HIGE | $h/R = 1$ | $\theta_g = 0°$	-6.6	-
HIGE | $h/R = 1$ | $\theta_g = 15°$	-9.4, -38.4	-6.3
HIGE | $h/R = 1$ | $\theta_g = 30°$	-17.5 $\pm i$ 6.4	370.

Table 4.4. Poles and zeros location of the C_M *Vs.* λ_c transfer function: comparison between numerical data and Pitt-Peters analytic model.

As expected, the only remarkable differences with respect to the results presented in figure 4.17 and table 4.3 occur in the inclined-ground case. Generally, the parallel ground affects the C_L *Vs.* λ_s and C_M *Vs.* λ_c transfer functions by shifting their poles to a less damped condition. The same consideration can be done for the effect of inclined ground on C_L *Vs.* λ_s poles. For the C_M *Vs.* λ_c transfer functions instead, in the inclined case, the identified transfer function has at least one of the two (see 3.1) poles significantly less damped than that of the corresponding C_L *Vs.* λ_s transfer functions. Moreover the gain shows a maximum which is quite higher than the corresponding static one.

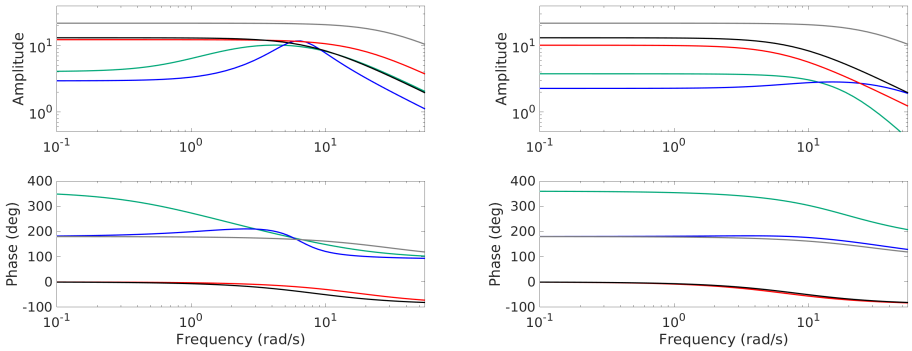

(a) $h/R = 0.75$ (b) $h/R = 1$

Figure 4.18. Magnitude and phase of C_M *Vs.* λ_c transfer function: comparison between numerical data. Pitt-Peters ——; HOGE —— ; HIGE: —— $\theta_g = 0°$; —— $\theta_g = 15°$; —— $\theta_g = 30°$.

In table 4.5 and figures 4.19 and 4.20 the transfer function of the specific inclined coupled transfer function, literally C_T *Vs.* λ_c and C_M *Vs.* λ_0, are shown. The accuracy of the identification is not the best, the coherence low, but the robustness of the identification hypothesis however extract a smooth function that could be verified with the time-marching validation.

Case	C_T *Vs.* λ_c poles	C_M *Vs.* λ_0 poles
HIGE | $h/R = 0.75$ | $\theta_g = 15°$	0, -18.2	-9.7 $\pm i$ 17.1
HIGE | $h/R = 0.75$ | $\theta_g = 30°$	-0.3 $\pm i$ 1.3	-5.8 $\pm i$ 9.2
HIGE | $h/R = 1$ | $\theta_g = 15°$	-7.6, -8.5	-3.9, -17.9
HIGE | $h/R = 1$ | $\theta_g = 30°$	-6.2, -12.8	-14.7 $\pm$ 15.5

Table 4.5. Poles[4]location of the C_T *Vs.* λ_c and C_M *Vs.* λ_0 transfer functions, present only in the inclined-ground case.

[4]According to the hypothesis of Section 3.3 no zeros are present in the coupled transfer function.

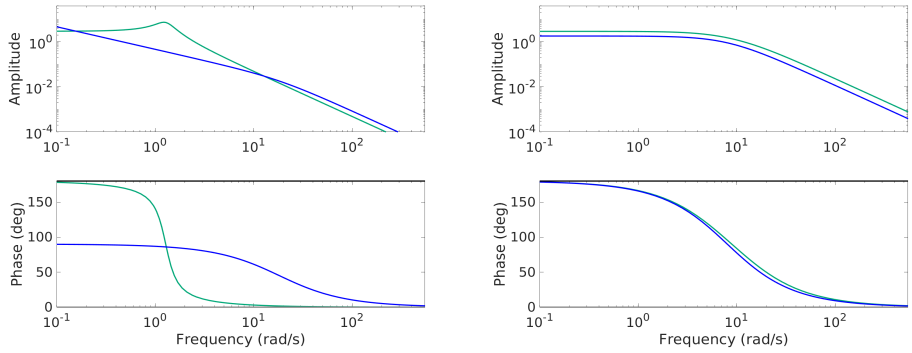

(a) $h/R = 0.75$ (b) $h/R = 1$

Figure 4.19. Magnitude and phase of C_T *Vs.* λ_c transfer function: comparison between numerical data. $\theta_g = 15°$; $\theta_g = 30°$.

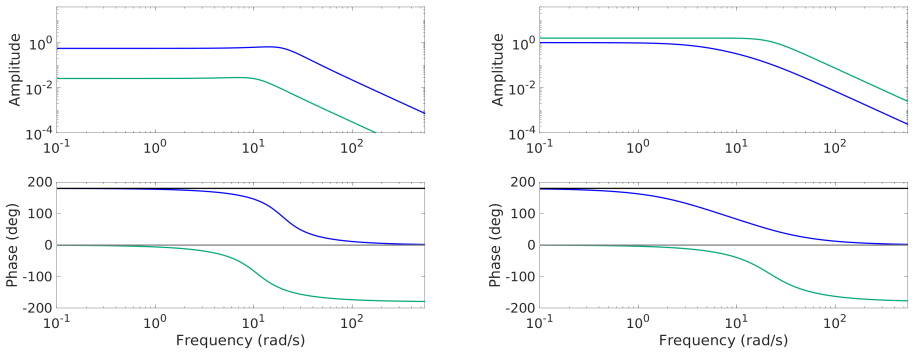

(a) $h/R = 0.75$ (b) $h/R = 1$

Figure 4.20. Magnitude and phase of C_M *Vs.* λ_0 transfer function: comparison between numerical data. $\theta_g = 15°$; $\theta_g = 30°$.

However, looking at the transfer functions Bode representation of figures 4.19 and 4.20 the inclined ground seems to influence the dynamic inflow by introducing a not negligible first order dynamic, which are characterized by a pole-damping in the range of the flight dynamic frequency spectrum.

4.2.1 Time response validation

Finally, the synthesized in-ground-effect perturbed wake inflow model is verified against a validation data-set numerically evaluated by imposing to the vortex-lattice aerodynamic high-fidelity solver a perturbation on $\Delta\phi$ different from that used in the identification process, the following expression are used to generate the perturbed

inputs:

$$\Delta\varphi^0(t) = cos(5t)sin(2t) \tag{4.1}$$

Figures in 4.21 show the response of the vortex-lattice model and the state-space one in terms of non-dimensional inflow coefficients, (λ_0, λ_s, λ_c), for the parallel to ground simulation of the rotor at $h/R = 0.75$, nevertheless high-fidelity results show numerical noise the reduced-order model prediction captures the main feature of the signal for all the three output. The non-perfect periodicity of the vortex-lattice data may be due to the random movement and collapse of the inner part of the wake which is periodically re-ingested by the rotor, on the other side the state-space prediction erases this uncertainty in the signal.

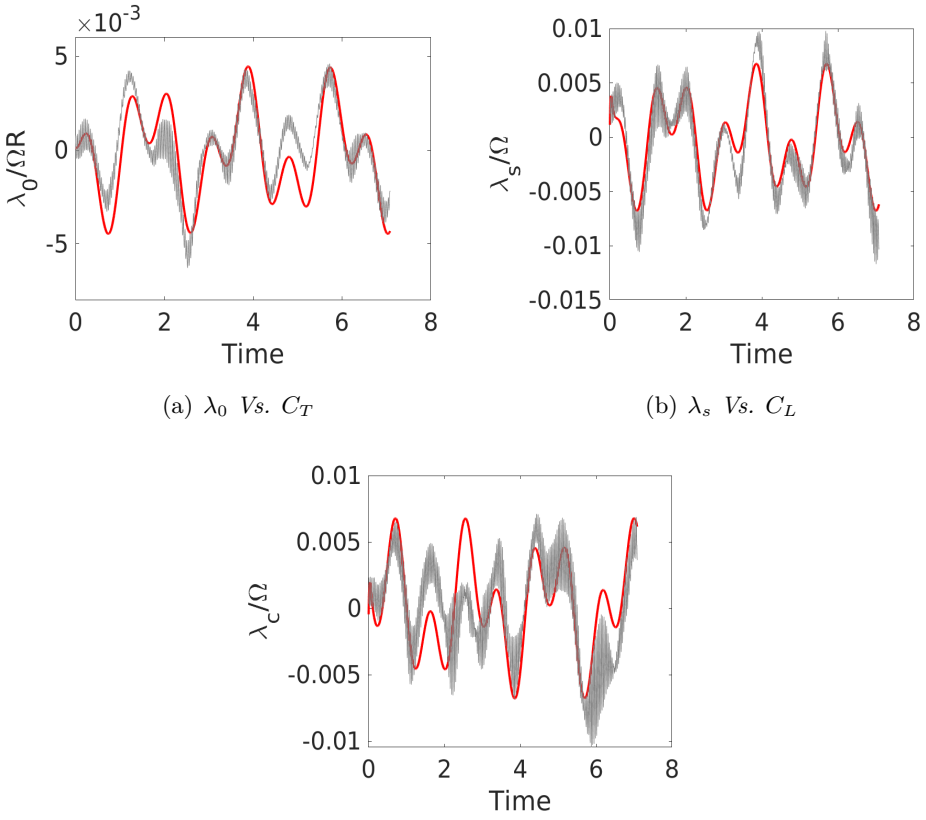

(a) λ_0 *Vs.* C_T

(b) λ_s *Vs.* C_L

(c) λ_c *Vs.* C_M

Figure 4.21. Time-marching validation, $h/R = 0.75$ and $\theta_g = 0°$; —— reduced-order model, —— high-fidelity aerodynamic solver.

Figures in 4.22 are about the HIGE for $h/R = 1$ and $\theta_g = 0°$, analogous considerations can be done for this case but the λ_s *Vs.* C_L shows a worst agreement between numerical data and state-space prediction even if the phase and the general behavior is somehow captured.

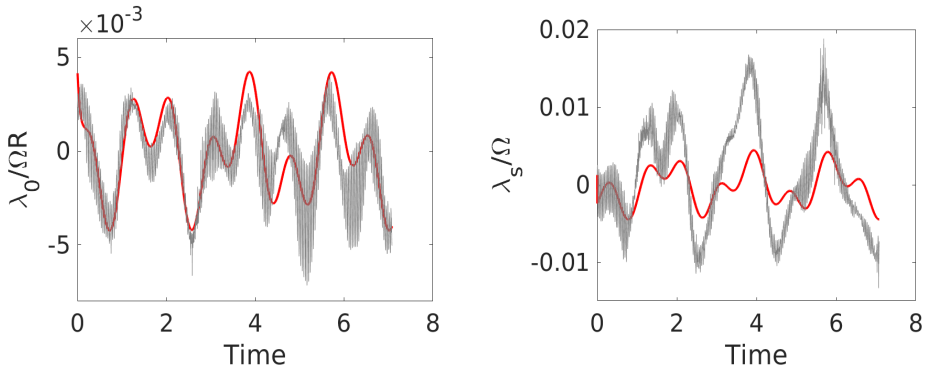

(a) λ_0 *Vs.* C_T (b) λ_s *Vs.* C_L

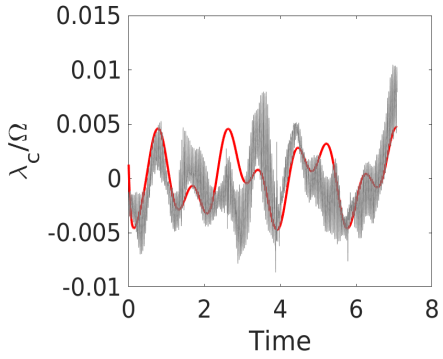

(c) C_M *Vs.* λ_c

Figure 4.22. Time-marching validation, $h/R = 1$ and $\theta_g = 0°$; —— reduced-order model, —— high-fidelity aerodynamic solver.

Figures in 4.23 and 4.24 show the capability in capturing the inflow variations in inclined-ground-effect. The reduced-order model shows a smooth and stable answer which seems to be in good agreement with the numerical direct simulation only when the signal shows a lower noise amplitude (clear notable in 4.23(a)). Figure 4.23(b), instead, proves a non satisfactory accuracy, as expected from the coherence analysis, nevertheless the high-fidelity signal is very disturbed and far from a smooth periodic signal as expected from the linear harmonic being of the state-space model.

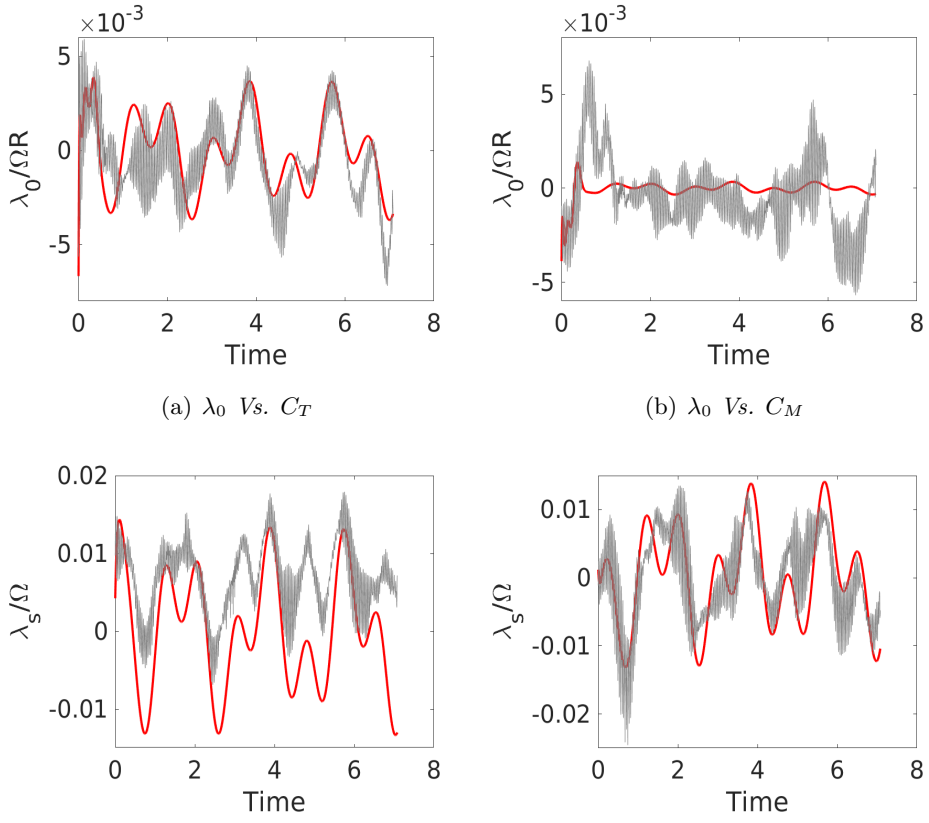

(a) λ_0 *Vs.* C_T

(b) λ_0 *Vs.* C_M

(c) λ_s *Vs.* C_L

(d) λ_s *Vs.* C_L - $\theta_g = 30°$

Figure 4.23. Time-marching validation, $h/R = 0.75$ and $\theta_g = 15°$; — reduced-order model, — high-fidelity aerodynamic solver.

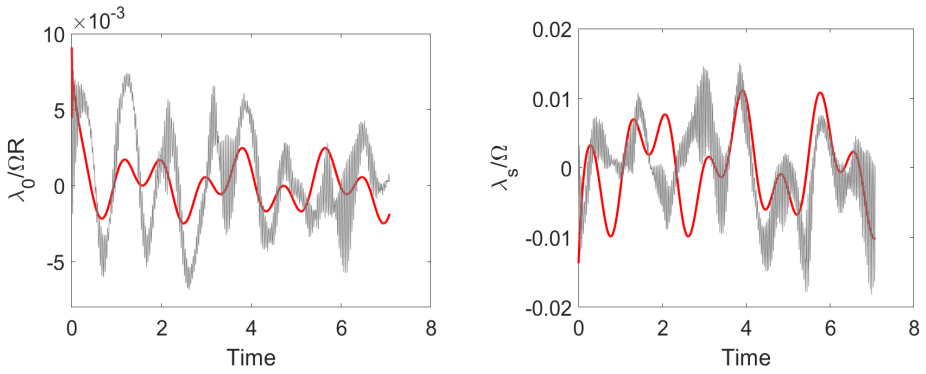

(a) λ_0 *Vs.* C_T

(b) λ_s *Vs.* C_L

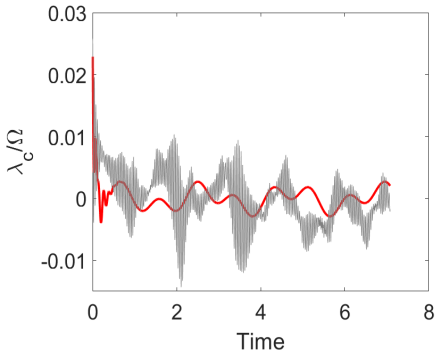

(c) λ_c *Vs.* C_M

Figure 4.24. Time-marching validation, $h/R = 1$ and $\theta_g = 30°$; — reduced-order model, — high-fidelity aerodynamic solver.

These facts suggest that the proposed method is capable to well capture the linear low-frequency part of the dynamic wake inflow even when the aerodynamic simulation output signals are rich of numerical noise. Moreover the low-frequency content of the inflow is the signal content that mostly influences the helicopter flight dynamics behavior. Lastly, figure 4.25 which depicts the spectrum of λ_0, highlights the tonal nature of the signal high-frequency content, which is clearly dominated by peaks around the multiple of the Blade Passing Frequency ($4/\Omega$, $8/\Omega$,...), although two low-frequency peaks, related through Werner's formulas to the frequencies of the trigonometric functions in Eq.4.1, arise. This suggests that, for aeroelasticity purposes, a Linear Time Periodic model is necessary, since a Linear Time Invariant model cannot reproduce an output at a different frequency with respect to that of the input.

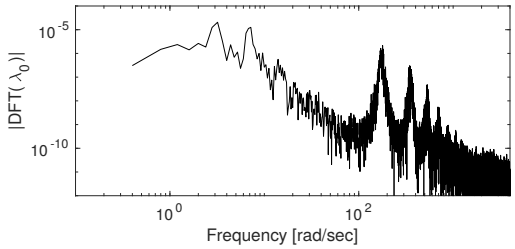

Figure 4.25. Spectrum of the λ_0 VLM time signal for $\theta_g = 30°$ in response to $\Delta\phi_0$.

4.3 Flight dynamics application

The identified reduced-order models of the wake inflow are applied to flight mechanic analysis, in the following section the obtained results are shown. Briefly the *Helistab* code is a comprehensive helicopter code developed in the last decade at **Roma Tre University**. It considers rigid body dynamics, blade aeroelasticity, air-frame elastic motion, as well as effects from actuators dynamics and stability augmentation systems. Passive and active pilot models can be included, and both linear and nonlinear analyses may be performed. The solver has been validated and applied within the activities of the European Project ARISTOTEL, addressed to the study of Rotorcraft-Pilot Couplings (RPC) phenomena [86, 87, 88, 64].
The linearized equations of aeromechanics are written as a first order differential system,

$$\dot{\boldsymbol{z}} = \boldsymbol{A}\boldsymbol{z} + \boldsymbol{B}\boldsymbol{u} \tag{4.2}$$

where z collects Lagrangian coordinates of elastic blade and air-frame deformations and their derivatives, air-frame rigid-body (center-of-mass) linear and angular velocity components, Euler angles and inflow states, x, whereas u collects main and tail rotor controls and their first and second order derivatives, namely, $u = \{\ddot{\theta}_0, \dot{\theta}_0, \theta_0, \ddot{\theta}_s, \ldots, \theta_p\}^T$.
In the following, details concerning the derivation of matrices A and B in Eq.4.2 are provided for aeromechanics formulations using both kinematic-based and loads-based dynamic inflow models.

4.3.1 Kinematic-based inflow

Recasting the vector of state variables as $z = \{y\ x\}^T$, coupling the rotor and airframe dynamics equations with the dynamic inflow model of Eq.3.4 yields the

following aeromechanics model

$$\begin{aligned}\dot{y} &= A_y y + C_\lambda \boldsymbol{\lambda} + B_y u \\ \boldsymbol{\lambda} &= A^{wi}_{1y}\dot{y} + A^{wi}_{0y} y + C^{wi}\boldsymbol{x} + A^{wi}_{0u} u \\ \dot{\boldsymbol{x}} &= B^{wi}_{y} y + A^{wi}\boldsymbol{x} + B^{wi}_{u} u\end{aligned} \tag{4.3}$$

with C_λ collecting the derivatives of the aerodynamic generalized forces of the aeromechanic model with respect to $\boldsymbol{\lambda}$. In addition, the matrices of the wake inflow model Eq.4.3 are obtained by re-organizing those in Eq.3.4, to be consistent with the vectors of variables of the aeromechanic model (for instance, hub linear velocities considered in 3.4 are given as a combination of the air-frame DoFs considered in the vector y).
Then, substituting the inflow model in the rotor/air-frame dynamics equations, the following set of first-order differential equations governing the helicopter dynamics are obtained

$$\begin{aligned}&\dot{y} = (I - C_\lambda A^{wi}_{1y})^{-1}[(A_y + C_\lambda A^{wi}_{0y})y + \\ &+C_\lambda C^{wi}\boldsymbol{x} + (B_y + C_\lambda A^{wi}_{0u})u] \\ &\dot{\boldsymbol{x}} = B^{wi}_{y} y + A^{wi} x + B^{wi}_{u} u\end{aligned} \tag{4.4}$$

from which matrices A and B of Eq. 4.2 may be easily identified.

4.3.2 Load-based inflow

When load-based inflow model is used, the aeromechanics equations may be written as

$$\begin{aligned}\dot{y} &= A_y y + C_\lambda \boldsymbol{\lambda} + B_y u \\ \boldsymbol{\lambda} &= C^{wi} x \\ \dot{x} &= A^{wi} x + B^{wi}_{f} f\end{aligned} \tag{4.5}$$

where the perturbative hub loads appearing in Eq.4.5 are given by the following linearized form

$$\boldsymbol{f} = \boldsymbol{F_y y} + \boldsymbol{F_\lambda \lambda} + \boldsymbol{F_u u} \tag{4.6}$$

Finally, combining Eq.4.5 and Eq.4.6 yields the following set of first-order differential equations governing the helicopter dynamics

$$\begin{aligned}\dot{y} &= A_y y + C_\lambda C^{wi} x + B_y u \\ \dot{x} &= B^{wi}_{f} F_y y + (A^{wi} + B^{wi} F_\lambda C^{wi}) x + B^{wi}_{f} F_u u\end{aligned} \tag{4.7}$$

from which matrices A and B of Eq.4.2 may be readily identified.
It is worth noting that for the vorticity-based model no modifications are needed

to implement inflow state matrix in the flight dynamic solver indeed they are in the same form of the $\lambda - f$ case, in particular A^{wi}, B^{wi} and C^{wi} are the same of equation 3.9.

4.3.3 Transfer function and stability

Here for the sake of conciseness only the vorticity-based inflow are applied to helicopter simulation tool[5]. The data simulate an helicopter hovering at two different heights from the ground and with three different ground inclination angles (the same of Section 4.2). Stability analysis is carried out (root locus plot) and the transfer function of the dominant *pilot-input/helicopter-DOF* frequency response illustrated.

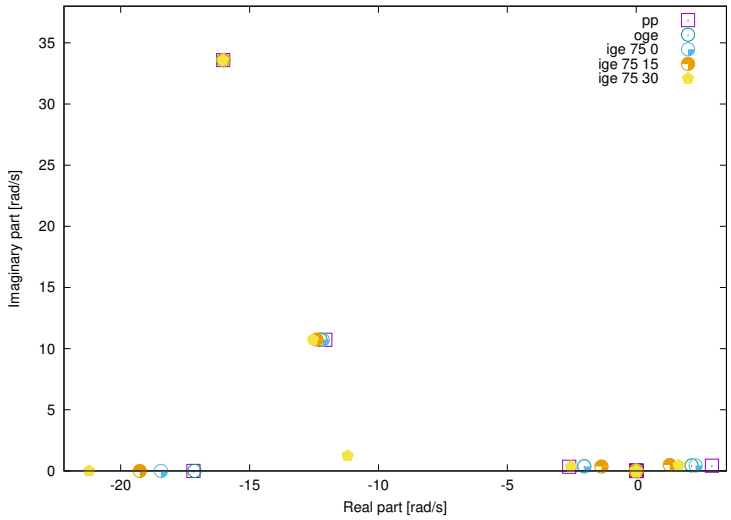

Figure 4.26. Effect of the presence of the ground on root locus. Rotor height from the ground $h/R = 0.75$ and ground angle $\theta_g = (0°, 15°, 30°)$.

[5]For the application of the kinematic-based inflow model to helicopter flight dynamics see [89].

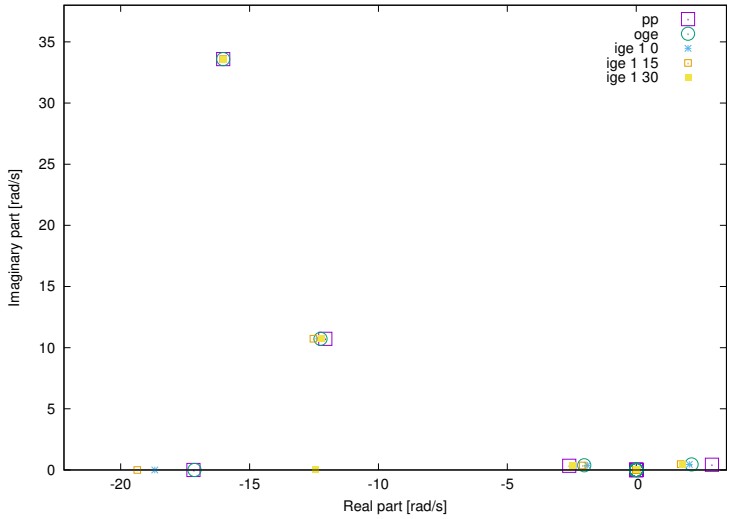

Figure 4.27. Effect of the presence of the ground on root locus. Rotor height from the ground $h/R = 1.$ and ground angle $\theta_g = (0°, 15°, 30°)$.

Figures 4.26 and 4.27 show the root locus, specifically in the flight dynamic frequency range of interest. It is worth noting that the main effect of the ground on the helicopter stability seems to be a general increase of the whole stability, the principal poles experiment an increase in the damping, this is particularly evident for $h/R = 0.75$, the phugoid mode and the dutch roll has a relevant shift. Ground angle also seems to affect the helicopter dynamics by increasing the dumping of the system.

Coherently with the shift of these modes, the helicopter response is significantly modified by the ground presence. A general smoothing in the peak corresponding to the shifted pole is visible in all the considered transfer functions, those regarding the configuration of $h/R = 0.75$ are reported in figures 4.28(a)-4.28(e), whereas figures 4.29(a)-4.29(e) depict the frequency response for $h/R = 1.$. In particular, the peaks of the response associated to the phugoid and dutch roll poles, which are particularly pronounced out of ground effect especially in the transfer functions related to cyclic controls, almost disappears from the Bode plot. The dutch roll mode have a gain reduction of more than $3dB$ for the lower ground effect condition, indeed, as expected the influence of the ground seems to be lower as higher is the distance between the rotor and the ground, figures 4.28(e) and 4.29(e). It is worth nothing that the peak in the w *Vs.* θ_0 response function (figures 4.28(a) and 4.29(a)), on the contrary, seems to be amplified by ground presence as well as q response seems to be affected by an increasing in the gain as the ground becomes more inclined, figures 4.28(b),4.28(f),4.29(b) and 4.29(f).

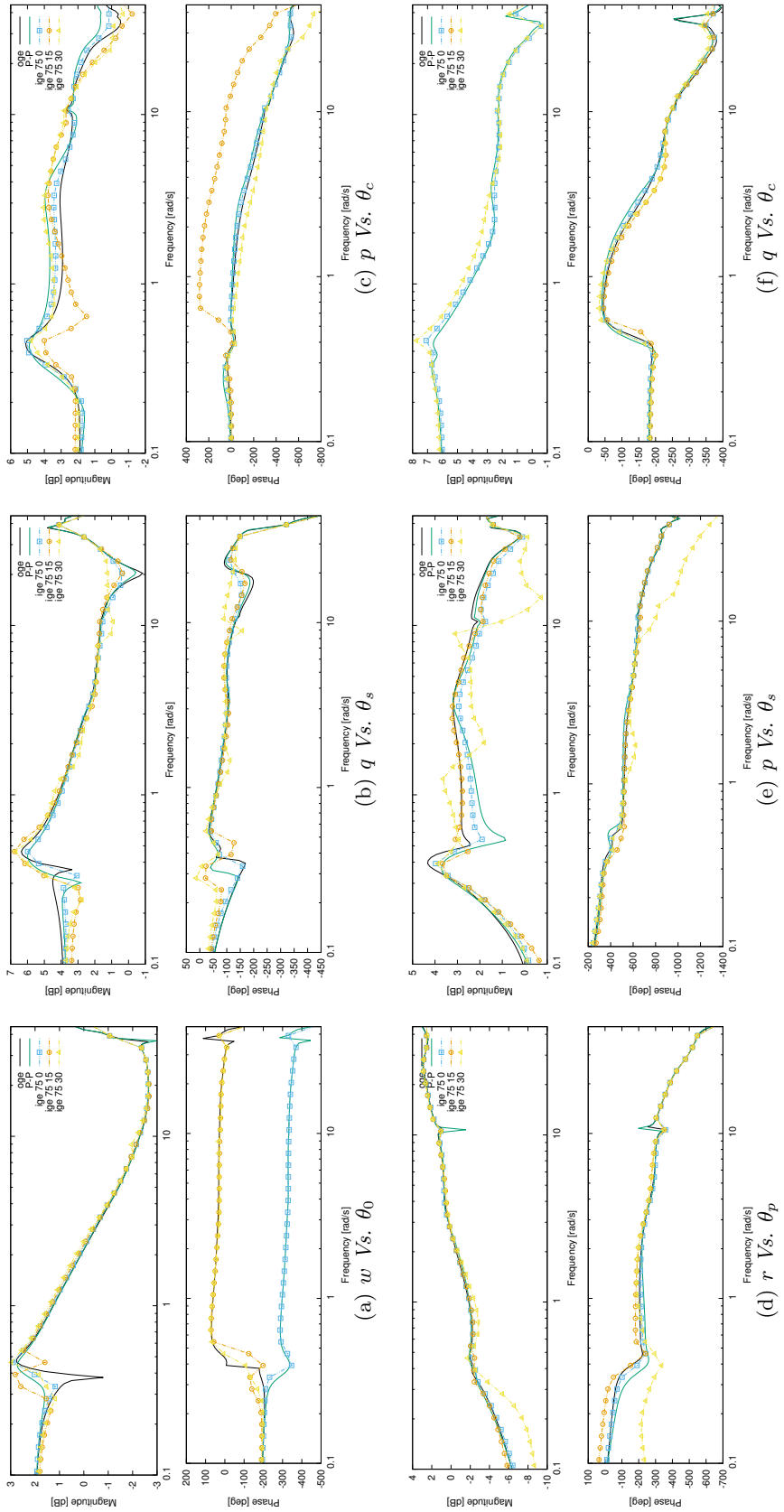

(a) w *Vs.* θ_0 (b) q *Vs.* θ_s (c) p *Vs.* θ_c

(d) r *Vs.* θ_p (e) p *Vs.* θ_s (f) q *Vs.* θ_c

Figure 4.28. Transfer function HOGE and HIGE for $h/R = 0.75$.

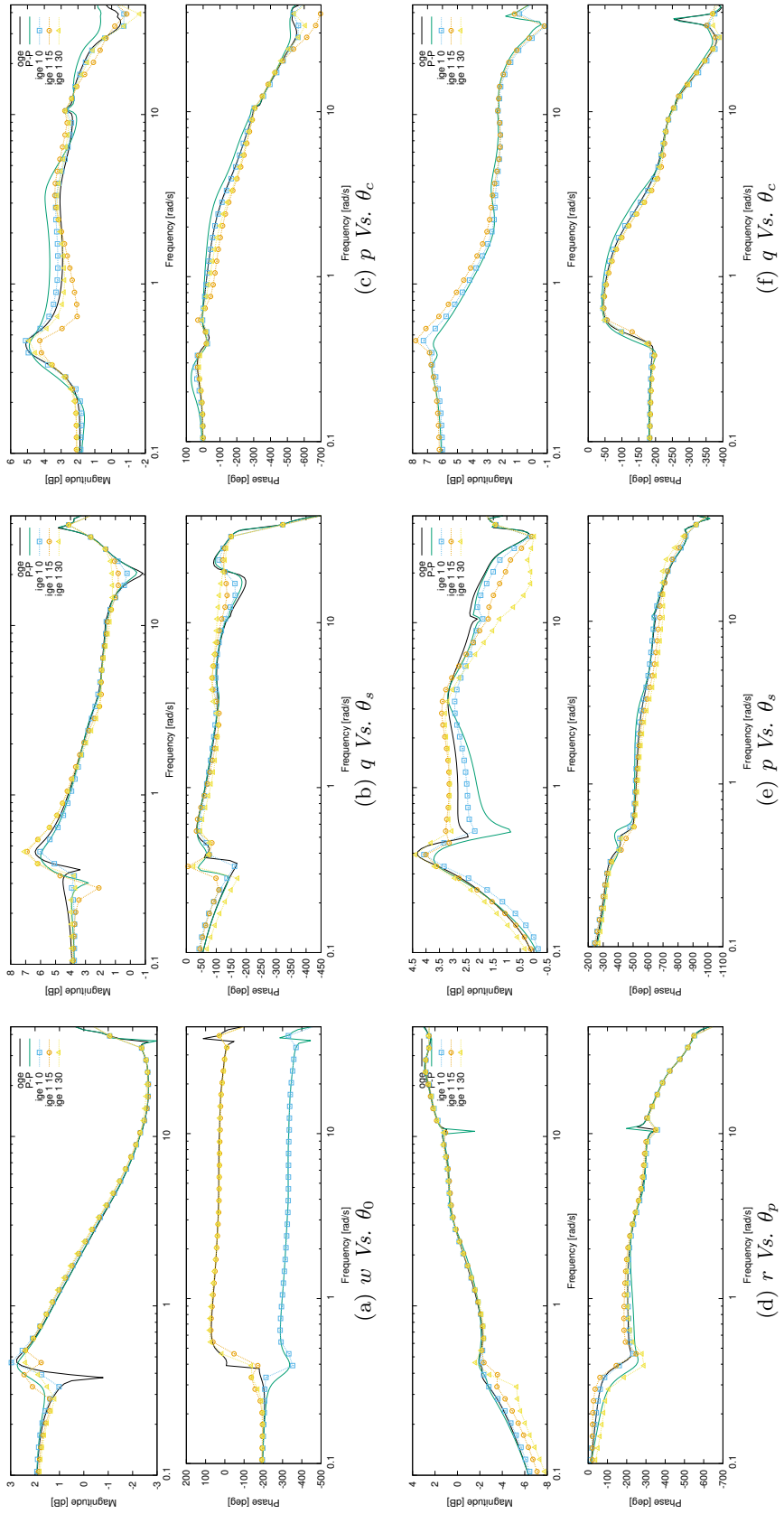

(a) w *Vs.* θ_0 (b) q *Vs.* θ_s (c) p *Vs.* θ_c

(d) r *Vs.* θ_p (e) p *Vs.* θ_s (f) q *Vs.* θ_c

Figure 4.29. Transfer function HOGE and HIGE for $h/R = 1$.

Finally, from these preliminary aeromechanic analyses, the most relevant effect of the ground presence has been noticed in the shift of helicopter poles with a general increasing in the dumping, which primarily affect roll response to cyclic controls and heave mode.

Chapter 5

Conclusions

In this work a study about the helicopter hovering in ground effect has been carried out, it is finalized to the extraction of dynamic wake inflow reduced-order models from high-fidelity aerodynamic simulation. Considering that for a wide range of activities (e.g.: SAR operations) the helicopter is still basically the only machine able to hover close to ground surface (even not parallel to rotor disc) and in presence of obstacles, it becomes evident the risen interest in ground effect simulation within the most used helicopter comprehensive simulation tools.
However, due to the complexity of the problem an accurate aerodynamic high-fidelity solver is necessary before the perturbed wake dynamic inflow could be identified. Thus, in order to assess the capability of the proposed aerodynamic solver to correctly simulate steady ground effect problem, a detailed comparison with experimental data has been performed. Two different approaches to model the ground presence in a Boundary Element Method aerodynamic solver have been developed and compared with experimental data of a rotor operating in different ground effect conditions. The two are:

- the bounded-domain method (BDM) which exploits the inclusion of additional boundary surface modeled with a distribution of sources and doublets;
- the mirror-image method (MIM) that, considering the ground as a reflection plane, includes a specular rotor-wake in the formulation.

Different disk loads and rotor heights from a parallel and inclined ground have been examined, performances and tip vortex position compared with experimental data and analytical prediction. Also the flow-field below the rotor and the wake structure have been analyzed comparing the velocity contour maps and the streamlines obtained over an azimuthal plane perpendicular to the ground rotation axis.

From this work the following conclusions could be drawn:

- BEM aerodynamic solver used in this work captures with good accuracy the behavior of rotors in ground effect, both thrust prediction and tip vortex geometry is good agreement with experimental results;

- because of the difficulty of the BEM-BDM (Bounded Domain Method) approach to satisfy with suitable accuracy the impermeability boundary condition over the ground, it is not enough in the prediction of induced power; this is why the BEM-MIM (Mirror Image Method) has proven to be suited for ground effect simulation, in that the boundary condition is automatically satisfied;

Strictly regarding the Mirror Image Method:

- performances analysis show that the aerodynamic solver well simulates and captures the physics of the phenomenon, the relation between induced power losses coefficient (C_{P_i}) and thrust coefficient (C_T) was coherent with the one experimentally measured;

- flow-field visualizations demonstrate the capability of the aerodynamic solver to well capture the wake deformation due to the presence of the ground. Velocity contour maps show a good agreement between experimental data and numerical simulations. The mean features of the flow-field are well captured except the inner wake region where there is an underestimation of the velocity magnitude;

- streamlines visualization proves that the aerodynamic solver is able to reproduce the presence of the recirculation zones in the inner part of the wake as the stagnation region on the ground plane. Furthermore as the ground becomes more inclined, their behaviour is well simulated as can be seen by the direct comparison between numerical and experimental data. It is worth noting that the analysis of the radial distribution of the axial velocity induced on the rotor disk has shown differences between the experimental data and the simulations. In particular, the numerical evaluation of the velocity has shown a variation of the distribution on the disk consistent with what is expected from the analysis of the velocity maps and the streamlines. Specifically, the inflow has to decrease in the upstream area and to increase in the downstream one while increasing the ground angle. Experimental data, on the other hand, has not shown this trend clearly. This fact, which deserves a detailed study, could be due to phenomena related to the chaotic nature of the turbulent structures present in the wake, which are not captured by potential non-viscous solver,

as well as the uncertainty inherent in the measure.

The identification of the reduced-order wake inflow models has been based on time marching Boundary Element Method simulations of the rotor in presence of the ground and it has been followed by a Rational Matrix Approximation, in order to obtain a state-space inflow model.
Once the BEM-MIM has been proven to be more suited for the ground modeling, two different approaches to dynamic inflow modeling of rotor in ground effect conditions have been applied. In the first, inflow coefficients are directly related to the kinematic degrees of freedom and subsequently to rotor loads involving a complete aerodynamic simulation, whereas the second one considers the relation between inflow coefficients and rotor loads (as in the well known Pitt-Peters' model) in terms of blade bound vorticity perturbations. The first approach is based over complete BEM-MIM solver simulation, both wake and body are discretized. Even if with a better approximation in loads evaluation, it is computationally inefficient for ground-effect simulation, indeed, due to the wake evolution complexity, the ground-effect simulation has been demonstrated to require a considerable computational effort. The computational burden is related to: i) the long wake needed to well capture the phenomena, hence a lot of elements in the computation; ii) a considerable number of time-steps are required to reach the equilibrium, and also an high number of tests is necessary to average the results and smooth the wake uncertainties. The second methodology, applied for the identification of a state-space dynamic wake inflow model, is based on inflow responses to arbitrary perturbations of blade bound vortex circulation distribution. Which, in turn, can be easily connected through the Glauert theory to the blade and hence rotor air-loads.
This approach requires only the simulation of the wake which, moreover, if treated as a vortex-lattice surface and exploiting the Biot-Savart law for the inflow evaluation, results in a very efficient computational tool for dynamic wake inflow model identification. Furthermore, the input/output coherence is higher than the kinematic-based model, thus allowing an easier identification of the wake inflow transfer function. The numerical investigation has concerned the application of the proposed methodologies for the wake inflow state-state model synthesis of rotors both out-of-ground-effect and in-ground-effect conditions, above parallel and inclined grounds. Considering the differences between the two dynamic inflow models presented in this work, the following conclusions simply try to outline the main physical and methodological relevance derived from this work. The physical considerations are averaged from the results obtained with the three different approaches. The main methodological observations are:

- both the presented methodologies have shown their capability in dynamic wake inflow identification even for ground effect condition. Nevertheless, the kinematic-based inflow model extraction has shown a limitation in its application due to the high numerical noise content of the BEM aerodynamic signal;

- kinematic-based model seems to be more suited to consider the fully-coupled dynamic system whereas the vorticity-based requires the statement of appropriate hypothesis before the model could be identified. On the contrary the vorticity-based model shows an higher signal coherence and a consequently more stable and efficient system identification;

- the identification process requires long simulations, due to the presence of significant numerical noise;

On the other hand the main physical evidences of this work, regarding the ground effect on wake dynamic inflow, are the following:

- the presence of the ground noticeably affects the wake inflow dynamic response;

- the ground presence affects remarkably the transfer functions dynamic inflow models identified from the high-fidelity BEM aerodynamic solver, depending on the distance from the rotor plane in a non-monotonic way;

- the ground presence increases the cross-coupling effects described by the off-diagonal terms of the transfer functions matrices of the dynamic inflow models, in particular the inclined ground condition show a coupling analogous to the one characterizing the forward flight condition;

- the proposed finite-state models predict with satisfactory accuracy dynamic wake inflow perturbations both in HOGE and HIGE conditions, as demonstrated by correlation with the simulations directly provided by the BEM solver for arbitrary perturbations system input;

- these models are not capable of simulating the higher-frequency inflow content, but capture the main features of the ground influence on the dynamic inflow and are particularly suited for flight dynamics applications;

- the validation tests show that the state-space model is capable of accurately reproduce the linear time invariant part of the low-frequency inflow content which is that significantly affecting flight dynamics. However, the wake inflow is also characterized by time-periodic phenomena, which cannot be reproduced by the proposed model, but would require the introduction of a time-periodic modeling approach;

- the identification process of the transfer functions involving axisymmetric components has been significantly more difficult, requiring further regularization of numerical free-wake algorithm to take into account the presence of the ground.

Finally the identified transfer function have been implemented within an helicopter comprehensive simulation tool, Helistab, stability and response analysis performed assessing the effect of the ground presence in helicopter simulation. The analysis has pointed out that the main effect of the ground on the helicopter dynamics is the augmented damping of the poles and the corresponding lower gain in the frequency response. The phugoid mode seems to be generally stabilized by the ground presence as confirmed by helicopter the roll and pitch response to cyclic perturbation low frequency region. However, these last results should be confirmed by flight data and are to be intended just as qualitative consideration.

Future work

The main open issues of these work, which need to be addressed in the future are the following:

- the extension of the BEM-MIM method to taking into account a moving ground (*i.e., ship deck moving in rough sea*). The capability to reproduce the flow-field and to evaluate the aerodynamic forces acting on the rotor will be first validated with experimental data, then the corresponding wake inflow model identified;

- the effect of the kinematic inputs, in particular roll and pitch angular rate, will be deeper investigated and the vorticity-based inflow model will be extended to these hub kinematic perturbations. Moreover, different blade vorticity distribution could be considered by expanding both the inflow and vorticity distribution over a set of different and more complete blade shape-function;

- the $\lambda - \Delta\varphi$ model will be completed with novel and more accurated vorticity/airloads relations. In particular like the one proposed in Appendix D in order to obtain a model suitable also for aero-elastic response prediction of a rotor operating in ground effect

Appendix A

Zero-*th* order Boundary Element Method discretization

For unsteady, incompressible, quasi-potential flows (*i.e., potential everywhere except on the wake surface*) around lifting bodies in arbitrary motion with respect to the undisturbed air, the velocity potential field may be expressed by the following boundary integral representation, [50]:

$$\varphi(\vec{x},t) = \int_{S_B} \left[G\frac{\partial \varphi}{\partial n} - \varphi \frac{\partial G}{\partial n} \right] \mathrm{d}S(\vec{y}) - \int_{S_W} \Delta\varphi \, \frac{\partial G}{\partial n} \, \mathrm{d}S(\vec{y}) \tag{A.1}$$

where S_B and S_W are body and wake surfaces, respectively. The impermeability boundary condition on S_B yields $\dfrac{\partial \varphi}{\partial n} = v_n = \vec{v}_B \cdot \hat{n}$, where $\vec{v}_B$ denotes the velocity of body points and $\hat{n}$ is on S_B, whereas $G = -1/4\pi||y-x||$ is the free-space fundamental solution of the three-dimensional Laplace equation. In addition, $\Delta\varphi$ is the potential jump across the wake surface that is given by the Kutta–Joukowski condition, [73], followed by convection of the trailing-edge potential discontinuity, that is,

$$\Delta\varphi(x_W,t) = \Delta\varphi(x_W^{TE}, t-\tau) \tag{A.2}$$

with τ denoting the time taken by a wake material point to move from the trailing-edge position $\times_W^{TE}$ to its current position x_W (see [69] for details).
Equation A.1 may be solved numerically by boundary elements (i.e., by discretizing S_B and S_W into quadrilateral panels), assuming φ, $\partial\varphi/\partial n$ and $\Delta\varphi$ to be piecewise constant, and imposing that the equation be satisfied at the center of each body element (collocation method). Specifically, dividing the blade surface into M panels S_{B_i} the wake surface into N panels S_{W_j}, and for $\chi = v_n$, equation A.1 yields

$$\varphi_k(t) = \sum_{i_1}^{M} B_{ki}\chi_i(t) + \sum_{i_1}^{M} C_{ki}\varphi_i(t) + \sum_{j_1}^{N} F_{kj}\Delta\varphi_j(t) \tag{A.3}$$

where $\varphi_i(t) = \varphi(x_i, t)$, $\chi_i(t) = \chi(x_i, t)$ and $\Delta\varphi_j = \Delta\varphi(x_{W_j}, t)$ and the source/sink and doublet coefficients representing the body surface are given by

$$\begin{aligned} B_{ki} &= -\frac{1}{4\pi} \int_{S_{B_i}} \left(\frac{1}{|y - x_k|} \right) dS \\ C_{ki} &= -\frac{1}{4\pi} \int_{S_{B_i}} \frac{\partial}{\partial n} \left(\frac{1}{|y - x_k|} \right) dS \end{aligned} \tag{A.4}$$

whereas the wake doublet contribution is

$$F_{kj} = -\frac{1}{4\pi} \int_{S_{W_j}} \left(\frac{1}{|y - x_k|} \right) dS \tag{A.5}$$

The shape of the wake is a part of the solution (free-wake procedure), it is achieved by a time-marching integration scheme in which the vertices of the wake panels are moved according to the velocity field computed from the potential solution; thus, the wake coefficients F_{kj} are recomputed at each time step [90].

Appendix B

On The Ontology of Wake Inflow

This Appendix deals with the experimental evaluation effectiveness of wake induced velocities over a wing, more specifically over a rotor blade. A numerical investigations is performed exploiting that the aerodynamics formulation [51] applied in this research work, (section 2.1), allows the evaluation of the velocity contributions due to each body or wake that is present in the examined configuration problem. This provides a unique tool suitable to make an estimation of the effect of the body contribution in the (total) inflow measured (or computed) in any field point. In particular, observing that dynamic inflow models are required to provide predictions of the inflow on the rotor blades only from the wake vorticity, it may help in assessing the suitability of the measured (total) inflow for dynamic inflow identification purposes.
The examined rotor is composed of two untwisted and untapered blades, with main characteristics reported in Tab. B.1, note that, this is the rotor considered by Milluzzo for the experimental activities of [35] (*see also section 2.3*).

Radius	0.408 [m]
Chord	0.04445 [m]
Airfoil	NACA 0012
Collective Pitch	6°
Rotation Velocity	2100 rpm

Table B.1. Two-bladed rotor main characteristics.

Simulating the experimental measurements, a sort of numerical Laser Doppler

Velocimetry (LDV) has been carried out on both wake inflow (only from wake vorticity) and total inflow (including body contribution) velocity components for the rotor operating in hovering with a collective pitch angle, $\theta = 6°$. A static perturbation of the collective pitch angle, $\theta_{pert} = 0.5°$ is considered. The measure grid extends $0.5R$ above and below the rotor disk and the data are acquired over an 80×80 equally spaced points. Figure B.1 depicts a sketch of the blade and of measurement points used for the analyses of inflow axial velocity component.

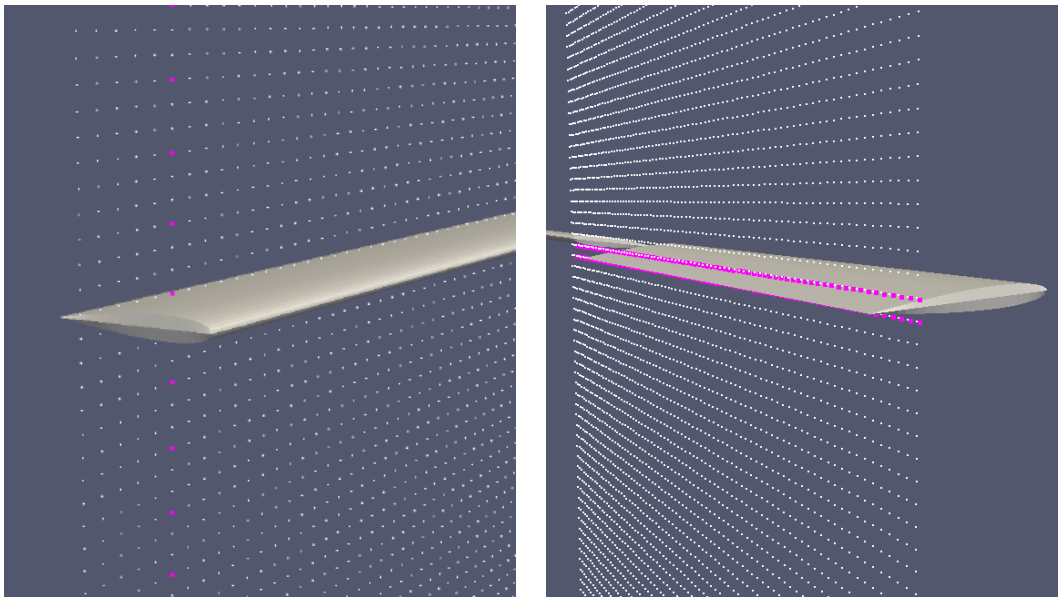

(a) Axial points of measurement (b) Span-wise points of measurement

Figure B.1. Grid and blade visualization; magenta dots represent points of measurement.

Figure B.2 concerns the induced velocities axial component at 3/4 chord line for the steady condition of $\theta = 6°$, the averaged value obtained from the span distribution over two equally spaced lines from the blade, one line below and one line above the rotor disk, is shown. Three different distances, $z/chord$, are considered and the total and the wake inflow are presented. Looking at the figure the following consideration can be drawn:

- moving away from the blade both inflow velocity decreases;
- total inflow and wake inflow are different;
- as the measuring lines approach the blade, the difference between two the computed inflows rapidly increases;
- body contribution strongly affects the total inflow (and hence that experimentally measured).

In Figure B.3 the time history of perturbation inflow for $\theta_{pert} = 0.5°$ (namely, the difference between the inflow evaluated for the perturbed collective pitch and that evaluated for the reference collective pitch) is depicted. In particular, this is a static estimation of the inflow involved in dynamic inflow modeling, the represented velocities are measured over four radial station $(0.125R, 0.375R, 0.625R, 0.875R)$ for a rotor revolution. For each radial station three (non-rotating) points of measure at different distances below the rotor disk are taken.

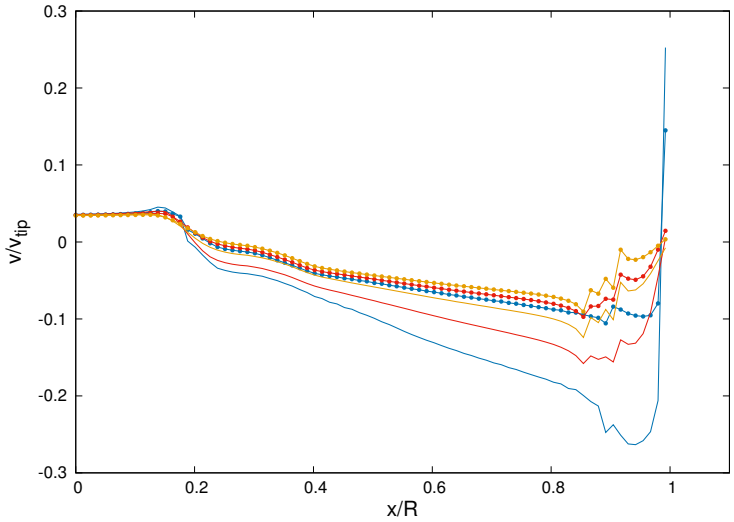

Figure B.2. Span distribution of axial inflow; solid line: total inflow; diamond markers: wake inflow. $z/chord = 0.11$, $z/chord = 0.33$, $z/chord = 0.56$.

The following consideration starting from B.3 can be derived:

- close to the blade root, total and wake inflows are very similar at any distance form the rotor disk;
- as the measurement points move towards the blade, the difference between two inflows significantly increases;
- body contribution strongly affects the blade measured inflow.

Figure B.4, instead, shows the time history of perturbation inflow for $\theta_{pert} = 0.5°$ for the same radial station of Fig.B.3 but for three different distances above the rotor disk, (0.05 $z/chord$, 1.6 $z/chord$, 3.2 $z/chord$). Analogous findings to figure B.3 can be seen, however it is worth nothing that since measuring points are outside wake region all curves in the figure are smoothed with respect to the ones in Fig.B.3.

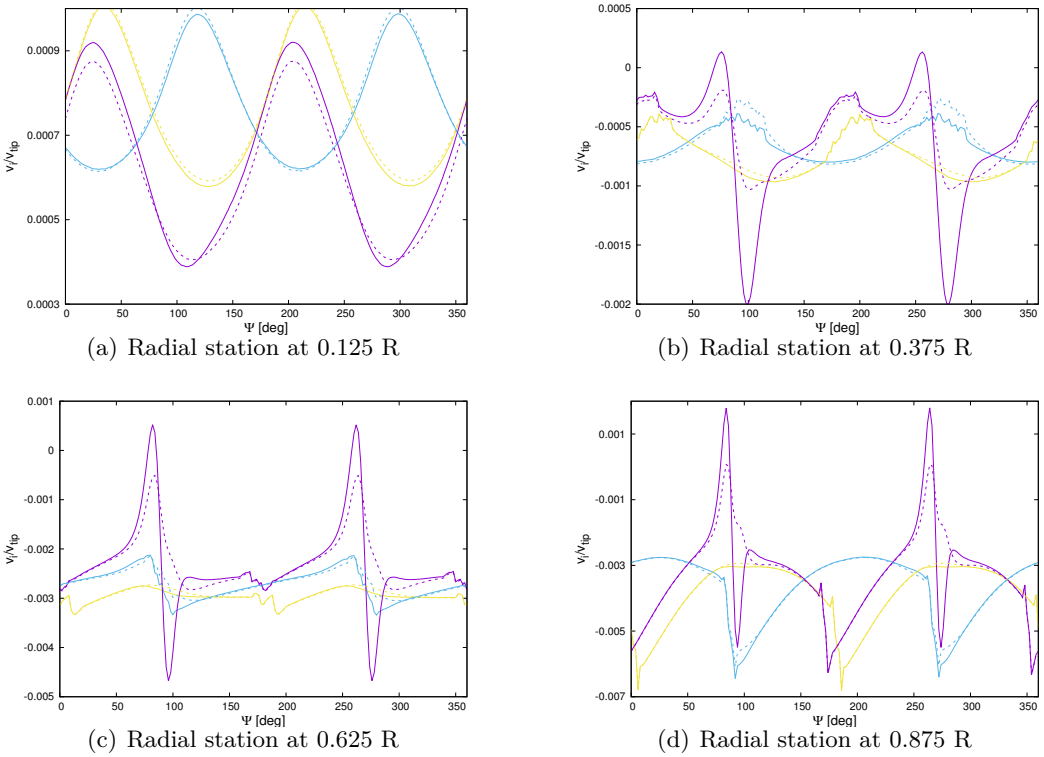

(a) Radial station at 0.125 R

(b) Radial station at 0.375 R

(c) Radial station at 0.625 R

(d) Radial station at 0.875 R

Figure B.3. Inflow time histories; solid lines: total inflow; dashed lines: wake inflow. $z/chord = -0.05$, $z/chord = -1.6$, $z/chord = -3.2$.

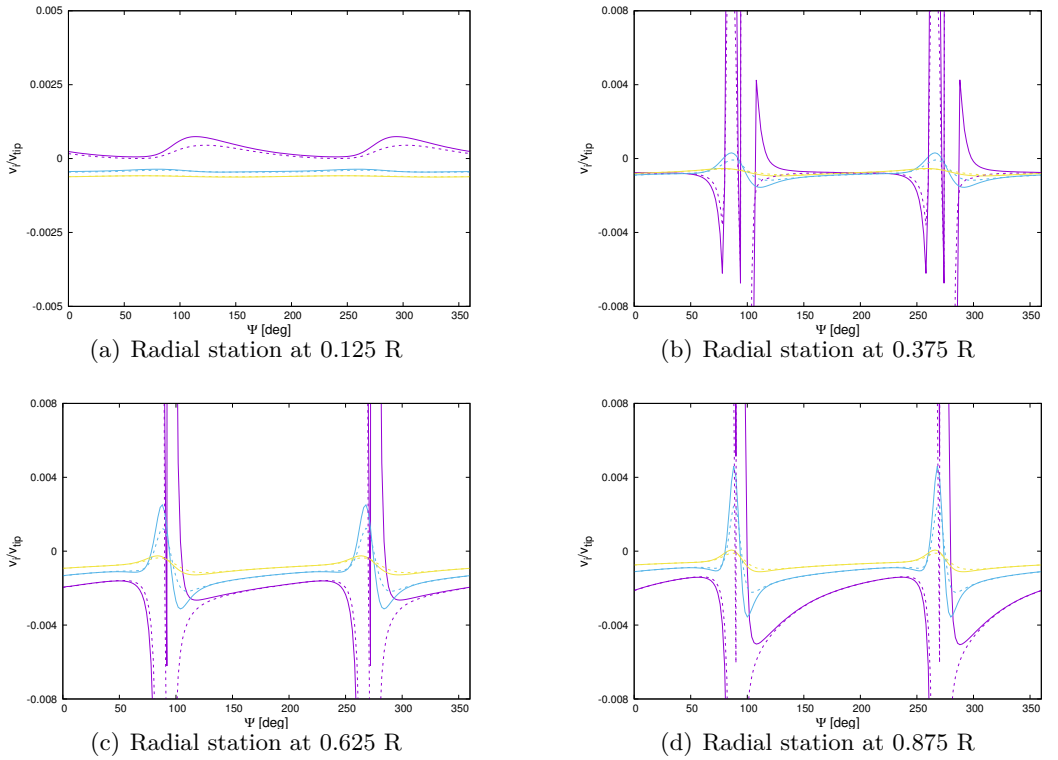

(a) Radial station at 0.125 R

(b) Radial station at 0.375 R

(c) Radial station at 0.625 R

(d) Radial station at 0.875 R

Figure B.4. Inflow time histories; solid lines: total inflow; dashed lines: wake inflow. —— $z/chord = 0.05$, —— $z/chord = 1.6$, —— $z/chord = 3.2$.

Concluding, the numerical investigation has shown that the inflow on the blade that might be measured experimentally (total inflow) is strongly affected by the body whereas far from the blade the inflow is dominated by the wake vorticity contribution. It is worth noting that the wanted inflow needs to be exactly the one that is over the blade in each azimuthal position, the 2-D aerodynamic theories request the knowledge of the instantaneous value of the induced velocity and thus a measured inflow seems to be unsuitable for dynamic inflow identification purposes, at least for the magnitude evaluation.

Appendix C

The issue of the ground impermeability condition in the BDM approach

In this appendix a semi-empirical strategy to taking into account the ground boundary layer is presented. It consists in the implementation of an algorithm capable to enforce the impermeability condition for those wake nodes which are closer to the ground. The main idea is to model the jet-flow transition of the wake flow through an artificial viscosity that brakes the normal-to-surface component of the wake node velocity. The change of the value of the normal to surface component of the velocity (*e.g.: vertical component in the case of parallel ground effect*), obtained by modulating its magnitude according to a quadratic function of the distance between the node and the surface, is applied only to the wake nodes ($\mathbf{x_{wake}}$) which are below a threshold arbitrary value, δ^* but over the ground surface. Under the assumption of a flat or at most concave surfaces, the threshold condition for a generic planar panel element of the ground is simply evaluated looking at the z-coordinate of the node, if it is below δ^* the vertical velocity is modulated as follows:

$$v_z^{new} = v_z^{old} f(node_z/\delta^*) \tag{C.1}$$

where

$$f(node_z/\delta^*) = (node_z/\delta^*)^2 \tag{C.2}$$

Figure C.1 is about the comparison between the phase-averaged tip vortex position obtained with the BEM-BDM with and without the numerical enforcement. It is clear how the imposition of the impermeability condition has an impact on the tip vortex position, a little radial expansion is obtained but is not enough if compared with the simulation performed by using the BEM-MIM method.

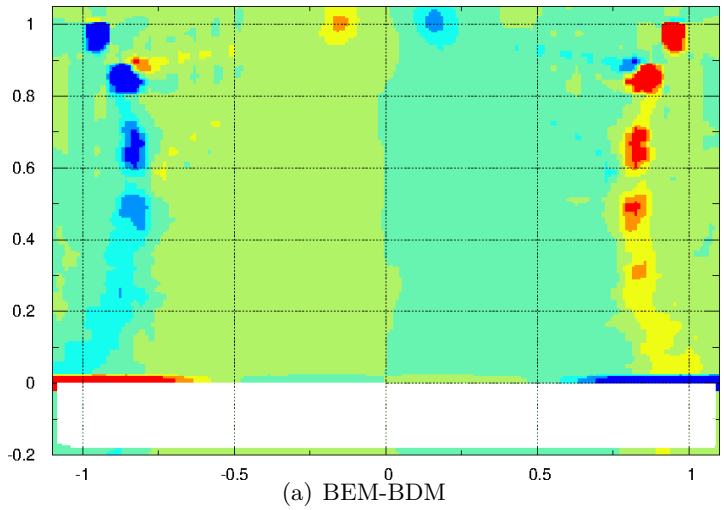

(a) BEM-BDM

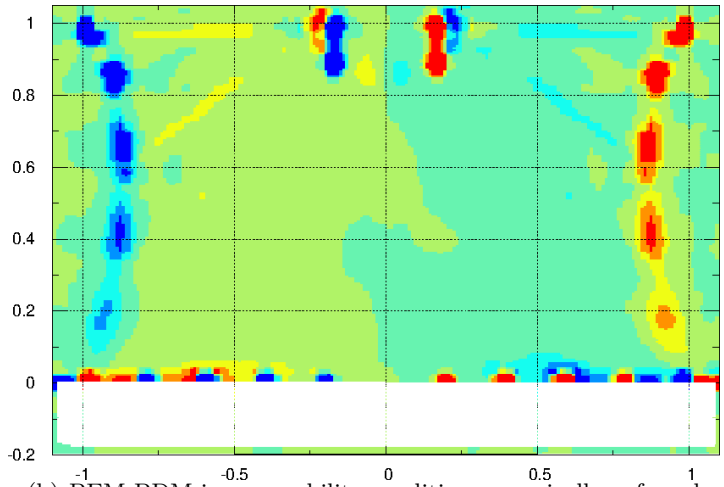

(b) BEM-BDM impermeability condition numerically enforced

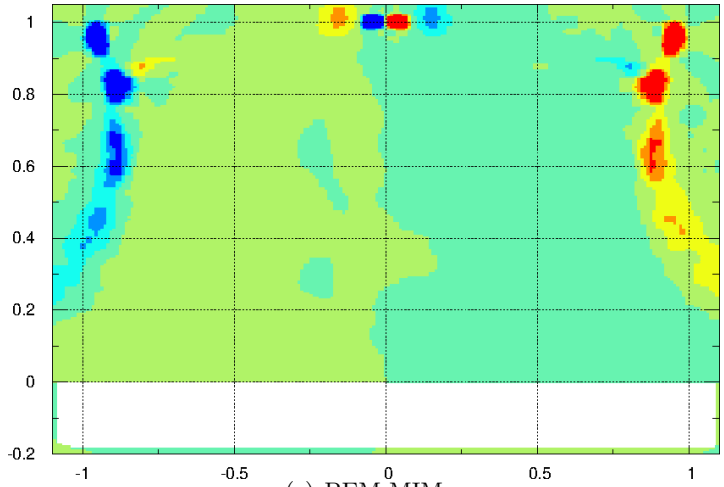

(c) BEM-MIM

Figure C.1. Tip vortex position for parallel ground hovering, $h_g/R = 1$, $\theta_g = 0°$.

In particular figure C.2 shows a visualization of a phase-averaged wake structure over more than 15 laps, the numerical enforcement of the impermeability condition effectively blocks the wake nodes at the ground surface, nevertheless the whole wake geometry is far from the right deformation as the comparison with the BEM-MIM solution.

Looking instead at the performance evaluation the is an error (underestimate)

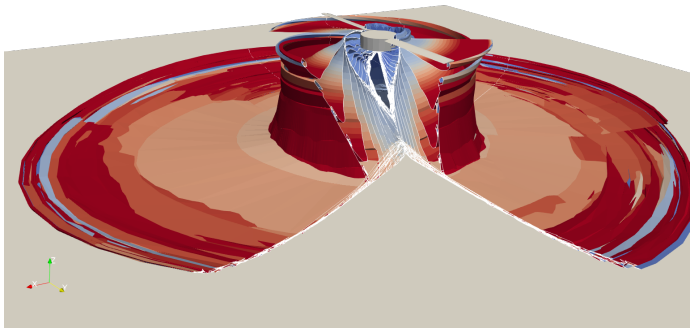

(a) BEM-BDM impermeability condition numerically enforced

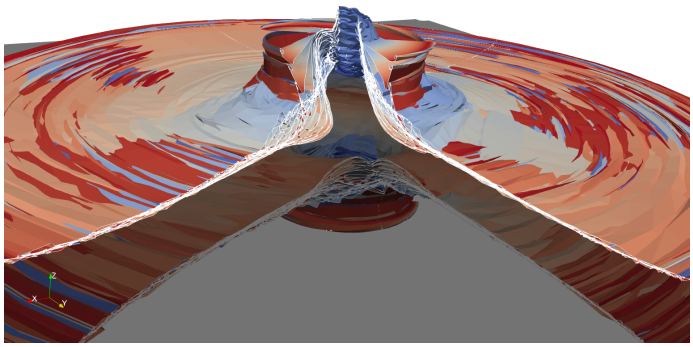

(b) BEM-MIM

Figure C.2. 3-D phase-averaged wake visualization for hovering rotor, comparison betweem MIM method and BDM method with enforced impermeability condition.

of the induced power losses of about 25% due to the wrong solution of the wake shape as it can be understood observing the induced inflow of figure C.3 where a comparison between the BDM corrected solution and the MIM solution for the inflow velocity over the blade.

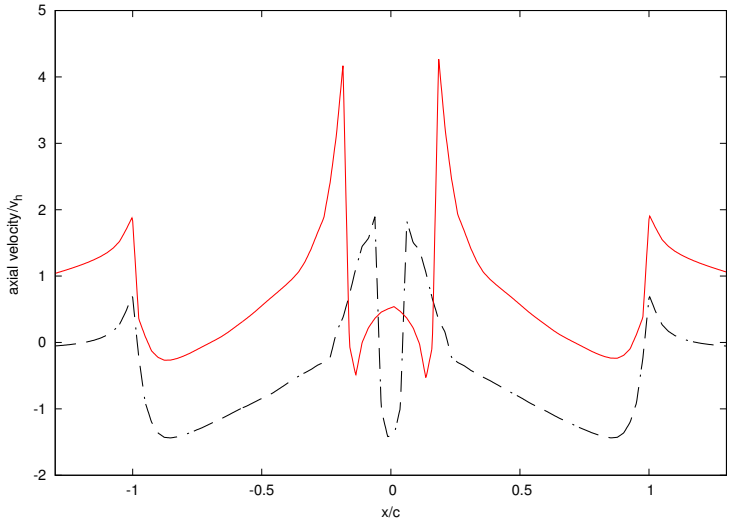

Figure C.3. Averaged inflow, - - - BEM-MIM, —— BEM-BDM modified (impermeability condition numerically enforced).

Appendix D

Potential discontinuity at trailing edge and vortex lattice method

Starting from Theodorsen's theory[91], a function relating the potential discontinuity at trailing edge and the aerodynamic loads acting on the airfoil is carried out, for the sake of conciseness the following steps are related only to the lift evaluation. The relation proposed by Theodorsen for the force acting over a 2-D airfoil in term of vorticity is

$$P = -\rho v b \int_1^\infty \frac{x_0}{\sqrt{x_0^2 - 1}} U dx_0 \tag{D.1}$$

where $U = \gamma_{shed}$, $b = c/2$ is the half chord, $v = u_\infty$ is the body velocity, x_0 is the coordinate describing the airfoil in its conformal-mapping transformation. The shed vorticity can be writen as

$$\gamma_{shed}(x_0, t) = \gamma_0 e^{i\omega t} e^{-i\frac{\omega b}{v} x_0} \tag{D.2}$$

then, rewriting the equation D.2 in terms of the vorticity trailed from the trailing edge, ($x_0 = 1$):

$$\begin{aligned} &\gamma_{TE}(t) = \gamma_0 e^{i\omega t} e^{-i\frac{\omega b}{v}} \; with\, k = \frac{\omega b}{v} \\ &\tilde{\gamma}_{TE} = \tilde{\gamma}_0 e^{-ik} \end{aligned} \tag{D.3}$$

and combining equations D.1 and D.3 one can obtain:

$$\begin{aligned} P =& -\rho v b \int_1^\infty \frac{x_0}{\sqrt{x_0^2-1}} \gamma_0 e^{i\omega t} e^{-i\frac{\omega b}{v} x_0} dx_0 = \\ =& -\rho v b \int_1^\infty \frac{x_0}{\sqrt{x_0^2-1}} e^{-ikx_0} dx_0 \gamma_0 e^{i\omega t} = \\ =& -\rho v b \int_1^\infty \frac{x_0}{\sqrt{x_0^2-1}} e^{-ikx_0} dx_0 \tilde{\gamma}_{TE} e^{ik} = \tilde{L} \end{aligned} \tag{D.4}$$

From the other hand the shed-vorticity trailed by the trailing edge could be expressed in terms of potential discontinuity $\Delta\varphi$ as follows:

$$\gamma_{TE} = -\frac{1}{v}\frac{\partial \Delta\varphi_{TE}}{\partial t} = -\frac{b}{b}\frac{1}{v}\frac{\partial \Delta\varphi_{TE}}{\partial t} = -\frac{1}{b}\frac{\partial \Delta\varphi_{TE}}{\partial \tau} \tag{D.5}$$

with

$$\tau = \frac{tv}{b} \tag{D.6}$$

and then

$$\tilde{\gamma}_{TE} = -\frac{1}{b} ik \Delta\tilde{\varphi}_{TE} \tag{D.7}$$

substituting D.7 into D.4 one obtains:

$$\begin{aligned} \tilde{L} =& -\rho v b \int_1^\infty \frac{x_0}{\sqrt{x_0^2-1}} e^{-ikx_0} dx_0 \tilde{\gamma}_{TE} e^{ik} = \\ =& \rho v \Delta\tilde{\varphi}_{TE} (ike^{ik} \int_1^\infty \frac{x_0}{\sqrt{x_0^2-1}} e^{-ikx_0} dx_0) \end{aligned} \tag{D.8}$$

where

$$h(k) = ike^{ik} \int_1^\infty \frac{x_0}{\sqrt{x_0^2-1}} e^{-ikx_0} dx_0 \tag{D.9}$$

is the transfer function that relates the sectional aerodynamic circulatory load and the potential discontinuity at the trailing edge. This expression could be integrated through the Bessel's functions of first and second order obtaining:

$$h(k) = e^{ik} ik \frac{\Pi}{2} (-J_1(k) + iY_1(k)) \tag{D.10}$$

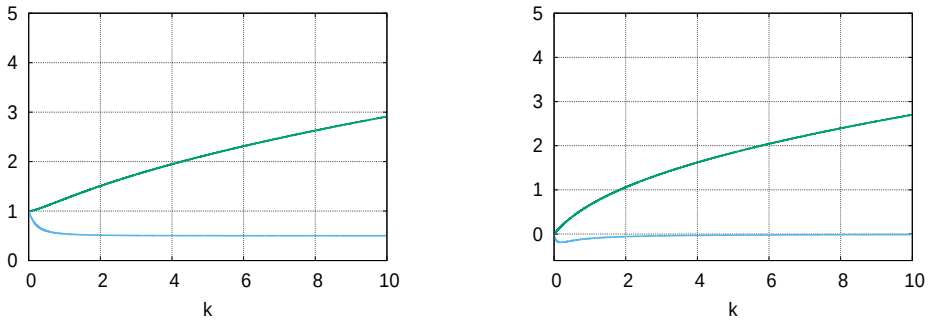

(a) Real (b) Imaginary

Figure D.1. Comparison between $c(k)$, Theodorsen's function, and $h(k)$.

Figure D.1 shows the comparison of the real and imaginary part of the Theodorsen function with this vorticity/lift one, figure D.2 instead, shows the comparison in terms of module and phase of the transfer function.

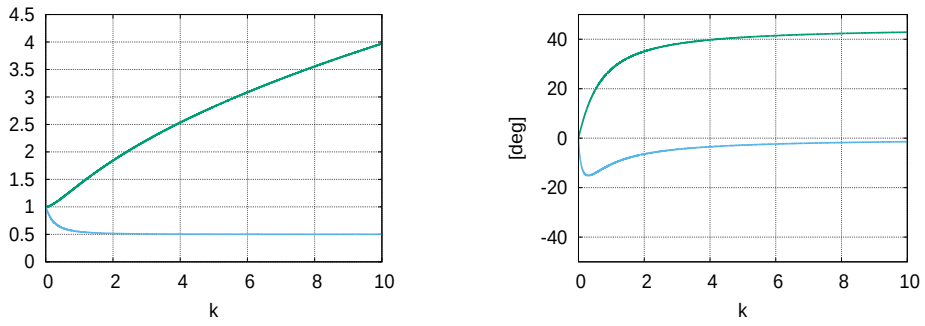

(a) Module (b) Phase

Figure D.2. Comparison between $c(k)$, Theodorsen's function, and $h(k)$.

From the figure D.2 in particular, the following observations can be drawn:

- $k \to 0$ the module of $h(k)$ tends to one and the phase to zero, analogously to the lift deficiency function, this means that in the steady case the well-known Glauert theory is still valid;

- $k \to \infty$ the phase shows an anomalous behaviour for a real physical system suggesting that the vorticity/lift relationship could be isolated only in a

mathematical point of view.

This result yet needs further studies and analyses in order to be extended to three dimensional finite wing as well for rotor application, however, it promise to be a powerful tool for Vortex-Lattice-Method since the exact derivation of the correct vorticity to be convected by the wake is still an open question, [92].

Bibliography

[1] G. Morrison, *Helicopter safety offshore*. HSE Books, 2001.

[2] AAIB, "Report no: 7/2008 - report on the accident to aerospatiale sa365n, registration g-blun, near the north morecambe gas platform, morecambe bay on 27 december 2006," tech. rep., October 2008.

[3] AAIB, "Report no: 1/2011 - report on the accident to eurocopter ec225 lp super puma, g-redu near the eastern trough area project (etap) central production facility platform in the north sea on 18 february 2009," tech. rep., September 2011.

[4] J. Smith and W. Mitchell, "Aircraft/ship interface problems - the u.s. navy's program," in *AIAA/SNAME Advanced Marine Vehicles Conference*, no. AIAA-PAPER 74-305, February 1974.

[5] R. M. Tuttle, "A study of helicopter landing behavior on small ships," *Journal of the American Helicopter Society*, vol. 21, no. 2, pp. 2–11, 1976.

[6] C. Kääriä, Y. Wang, J. Curran, J. Forrest, and I. Owen, "Airdyn: An airwake dynamometer for measuring the impact of ship geometry on helicopter operations," in *36th European Rotorcraft Forum, Paris*, pp. 7–9, 2010.

[7] C. H. Kääriä, Y. Wang, G. D. Padfield, J. S. Forrest, and I. Owen, "Aerodynamic loading characteristics of a model-scale helicopter in a ship's airwake," *Journal of Aircraft*, vol. 49, no. 5, pp. 1271–1278, 2012.

[8] S. J. Hodge, J. S. Forrest, G. D. Padfield, and I. Owen, "Simulating the environment at the helicopter-ship dynamic interface: research, development and application," *Aeronautical Journal*, vol. 116, no. 1185, p. 1155, 2012.

[9] S.-R. Oh, K. Pathak, S. K. Agrawal, H. R. Pota, and M. Garrett, "Autonomous helicopter landing on a moving platform using a tether," in *Proceedings of the 2005 IEEE International Conference on Robotics and Automation*, pp. 3960–3965, IEEE, 2005.

[10] K. Zeilstra, "Improving the offshore helicopter pilot's situation awareness," in *40th European Rotorcraft Forum*, 2014.

[11] C. Kääriä, J. Forrest, and I. Owen, "Assessing the suitability of ship designs for helicopter operations using piloted flight simulation," in *37th European Rotorcraft Forum, Vergiate and Gallarate, Italy*, pp. 13–15, 2011.

[12] J. A. Lusardi, M. B. Tischler, C. L. Blanken, and S. J. Labows, "Empirically derived helicopter response model and control system requirements for flight in turbulence," *Journal of the American Helicopter Society*, vol. 49, no. 3, pp. 340–349, 2004.

[13] G. H. Gaonkar, "Review of turbulence modeling and related applications to some problems of helicopter flight dynamics," *Journal of the AAmerican Helicpter Society*, vol. 53, no. 1, pp. 87–107, 2008.

[14] K. Schau, "Developing interpretive turbulence models from a database with applications to wind farms and shipboard operations," Master's thesis, M. Sc. Thesis, Department of Ocean and Mechanical Engineering, Florida Atlantic University, 2013.

[15] K. Schau, G. Gaonkar, and S. Polsky, "Rotorcraft downwash impact on ship airwake: statistics, modelling, and simulation," *The Aeronautical Journal*, vol. 120, no. 1229, pp. 1025–1048, 2016.

[16] D. M. Pitt and D. A. Peters, "Theoretical Predictions of Dynamic Inflow Derivatives," *Vertica*, vol. 5, pp. 21–34, 1981.

[17] D. A. Peters and C. J. He, "Correlation of measured induced velocities with a finite-state wake model," *Journal of the American Helicopter Society*, vol. 36, no. 3, pp. 59–70, 1991.

[18] H. Xin, J. Prasad, D. Peters, T. Nagashima, and N. Iboshi, "A finite state inflow model for simulation of helicopter hovering in ground effect," in *ANNUAL FORUM PROCEEDINGS-AMERICAN HELICOPTER SOCIETY*, vol. 54, pp. 777–784, AMERICAN HELICOPTER SOCIETY, 1998.

[19] H. Xin, J. Prasad, and D. Peters, "Dynamic inflow modeling for simulation of a helicopter operating in ground effect," in *Modeling and Simulation Technologies Conference and Exhibit*, p. 4114, 1999.

[20] H. Xin, J. Prasad, and D. Peters, "Dynamic inflow modeling for simulation of a helicopter operating in ground effect," in *Modeling and Simulation Technologies Conference and Exhibit*, p. 4114, 1999.

[21] H. Xin, J. Prasad, D. Peters, N. Itoga, N. Iboshi, and T. Nagashima, "Ground effect aerodynamics of lifting rotors hovering above inclined ground plane," in *17th Applied Aerodynamics Conference*, p. 3223, 1999.

[22] J. A. Morillo, "A fully three-dimensional unsteady rotor inflow model from a galerkin approach.," 2001.

[23] F. Cardito, R. Gori, G. Bernardini, J. Serafini, and M. Gennaretti, "Finite-state dynamic wake inflow modelling for coaxial rotors," in 41^{st} *European Rotorcraft Forum*, (Munich, D), September 2015.

[24] Y. Kong, J. Prasad, L. Sankar, and J. Kim, "Finite state coaxial rotor inflow model improvements via system identification," in *American Helicopter Society 72th Annual Form*, 2016.

[25] D. W. Hone, R. Ketzmerick, and W. Kohn, "Time Dependent Floquet Theory and Absence of an Adiabatic Limit," p. 13, 1997.

[26] O. Rand and V. Khromov, "Free-wake–based dynamic inflow model for hover, forward, and maneuvering flight," *Journal of the American Helicopter Society*, vol. 63, no. 1, pp. 1–16, 2018.

[27] Keller, Jeffrey D.; McKillip, Robert M.; Wachspres, Daniel A.; Tischler, Mark B.; Juhasz, Ondrej, "A free wake linear inflow model extraction procedure for rotorcraft analysis," in *73rd AHS Annual Forum & Technology Display*, (Fort Worth, Texas, USA), May 9-11 2017.

[28] W. Wiesner and G. Kohler, "Tail rotor performance in presence of main rotor, ground, and winds," *Journal of the American Helicopter Society*, vol. 19, no. 3, pp. 2–9, 1974.

[29] W. T. Yeager Jr, W. H. Young Jr, and W. R. Mantay, "A wind-tunnel investigation of parameters affecting helicopter directional control at low speeds in ground effect," Tech. Rep. TN D-7694, NASA, 1974.

[30] R. Empey and R. Ormiston, "Tail-rotor thrust on a 5.5-foot helicopter model in ground effect," in *American Helicopter Society Annual National Forum, Washington, DC*, 1974.

[31] H. Curtiss, M. Sun, W. Putman, and E. Hanker, "Rotor aerodynamics in ground effect at low advance ratios," *Journal of the American Helicopter Society*, vol. 29, no. 1, pp. 48–55, 1984.

[32] E. J. Hanker and R. P. Smith, "Parameters affecting helicopter interactional aerodynamics in ground effect," *Journal of the American Helicopter Society*, vol. 30, no. 1, pp. 52–61, 1985.

[33] J. Cimbala, M. Billet, D. Gaublomme, and J. Oefelein, "Experiments on the unsteadiness associated with a ground vortex," *Journal of Aircraft*, vol. 28, no. 4, pp. 261–267, 1991.

[34] J. S. Light, "Tip vortex geometry of a hovering helicopter rotor in ground effect," *Journal of the American helicopter society*, vol. 38, no. 2, pp. 34–42, 1993.

[35] J. Milluzzo, S. Drayton, A. Martinez, and S. Davids, "Piv and performance measurements on rotors hovering above inclined surfaces," in *AHS 74nd Annual Forum & Technology Display*, 2018.

[36] T. R. Quackenbush, D. B. Bliss, D. A. Wachspress, A. H. Boschitsch, and K. Chua, "Computation of rotor aerodynamic loads in forward flight using a full-span free wake analysis," 1990.

[37] D. A. Griffiths, S. Ananthan, and J. G. Leishman, "Predictions of rotor performance in ground effect using a free-vortex wake model," *Journal of the American Helicopter Society*, vol. 50, no. 4, pp. 302–314, 2005.

[38] M. Schmid, "Simulation of helicopter aerodynamics in the vicinity of an obstacle using a free wake panel method," in *43rd European Rotorcraft Forum (ERF 2017)*, 2017.

[39] J. Kucab, M. Moulton, M. Fan, and J. Steinhoff, "The prediction of rotor flows in ground-effect with a new hybrid method," in *17th Applied Aerodynamics Conference*, no. 99-3222, (Norfolk, VA), p. 3222, June 1999.

[40] N. Kang and M. Sun, "Simulated flowfields in near-ground operation of single- and twin-rotor configurations," *Journal of Aircraft*, vol. 37, pp. 214–220, Mar 2000.

[41] A. Filippone, R. Bakker, P. Basset, B. Rodriguez, R. Green, F. Bensing, and A. Visingardi, "Rotor wake modeling in ground effect conditions," *37th ERF, Sept*, 2011.

[42] S. Platzer, J. Milluzzo, and J. Rauleder, "Investigation on hovering rotors over inclined ground planes–a computational and experimental study," in *44th European Rotorcraft Forum*, (Delft, The Netherlands), September, 18-20 2018.

[43] AHS International - The Vertical Flight Technical Society, "University Research Report - New VLRCOE Teams Announced," December, 14 2016.

[44] V. Khromov and O. Rand, "Ground effect modeling for rotary-wing simulation," in *ICAS 2008- International Congress of The Aeronautical Sciences*, 2008.

[45] R. W. Prouty, *Helicopter performance, stability, and control*. Malabar, Fla : Krieger, 2005., 1995.

[46] E. A. Fradenburgh, "The helicopter and the ground effect machine," *Journal of the American Helicopter Society*, vol. 5, no. 4, pp. 24–33, 1960.

[47] B. M. Kutz, M. Keßler, and E. Krämer, "Experimental and numerical examination of a helicopter hovering in ground effect," *CEAS Aeronautical Journal*, vol. 4, no. 4, pp. 397–408, 2013.

[48] J. F. Tan, Y. M. Sun, T. Y. Zhou, G. N. Barakos, and R. B. Green, "Simulation of the aerodynamic interaction between rotor and ground obstacle using vortex method," *CEAS Aeronautical Journal*, vol. 10, no. 3, pp. 733–753, 2019.

[49] P. Ploumhans and G. Winckelmans, "Vortex methods for high-resolution simulations of viscous flow past bluff bodies of general geometry," *Journal of Computational Physics*, vol. 165, no. 2, pp. 354–406, 2000.

[50] L. Morino and M. Gennaretti, *Computational Nonlinear Mechanics in Aerospace Engineering*, vol. 146 of *Aeronautics & Astronautics AIAA Series*, ch. Boundary integral equation methods for aerodynamics, pp. 279–320. S.N. Atluri, 1992.

[51] M. Gennaretti and G. Bernardini, "Novel boundary integral formulation for blade-vortex interaction aerodynamics of helicopter rotors," *AIAA Journal*, vol. 45, no. 6, pp. 1169–1176, 2007.

[52] D. M. Pitt and D. A. Peters, "Rotor dynamic inflow derivatives and time constants from various inflow models," in *15th European Rotorcraft Forum: September 13-15, 1983, Stresa, Italy*, 1983.

[53] K. Yu and D. A. Peters, "Nonlinear state-space modeling of dynamic ground effect," *Journal of the American Helicopter Society*, vol. 50, no. 3, pp. 259–268, 2005.

[54] C.-J. He, *Development and application of a generalized dynamic wake theory for lifting rotors*. Ph.D. Thesis, Georgia Tech, July 1989.

[55] D. A. Peters, J. A. Morillo, and A. M. Nelson, "New developments in dynamic wake modeling for dynamics applications," *Journal of the American Helicopter Society*, vol. 48, no. 2, pp. 120–127, 2003.

[56] D. A. Peters, D. D. Boyd, and C. J. He, "Finite-state induced-flow model for rotors in hover and forward flight," *Journal of the American Helicopter Society*, vol. 34, no. 4, pp. 5–17, 1989.

[57] J. D. Keller, "An investigation of helicopter dynamic coupling using an analytical model," *Journal of the American Helicopter Society*, vol. 41, no. 4, pp. 322–330, 1996.

[58] U. T. Arnold, J. D. Keller, H. Curtiss, G. Reichert, *et al.*, "The effect of inflow models on the predicted response of helicopters," *Journal of the American Helicopter Society*, vol. 43, no. 1, pp. 25–36, 1998.

[59] J. Prasad, J. Zhao, and D. A. Peters, "Helicopter rotor wake distortion models for maneuvering flight," in *28th European Rotorcraft Forum*, (Bristol, UK), September 17-20 2002.

[60] O. Rand, V. Khromov, S. Hersey, R. Celi, O. Juhasz, and M. Tischler, "Linear inflow model extraction from high-fidelity aerodynamic models for flight dynamics applications," in *AHS 71st Internationl Annual Forum*, American Helicopter Society, INC, 2015.

[61] R. Gori, J. Serafini, M. Molica Colella, and M. Gennaretti, "Assessment of a state-space aeroelastic rotor model for rotorcraft flight dynamics," *CEAS Aeronautical Journal*, vol. 7, no. 3, pp. 405–418, 2016.

[62] M. Gennaretti, R. Gori, J. Serafini, G. Bernardini, and F. Cardito, "Rotor Dynamic Wake Inflow Finite-State Modelling," *33rd AIAA Applied Aerodynamics Conference*, June 2015.

[63] M. Gennaretti, R. Gori, F. Cardito, J. Serafini, and G. Bernardini, "A space-time accurate finite-state inflow model for aeroelastic applications," in *American Helicopter Society International 72nd Annual Forum*, West Palm Beach, Florida, 2016.

[64] J. Serafini, M. M. Colella, and M. Gennaretti, "A finite-state aeroelastic model for rotorcraft–pilot coupling analysis," *CEAS Aeronautical Journal*, vol. 5, no. 1, pp. 1–11, 2014.

[65] G. Bernardini, J. Serafini, M. Molica Colella, and M. Gennaretti, "Analysis of a structural-aerodynamic fully-coupled formulation for aeroelastic response of rotorcraft," *Aerospace Science and Technology*, vol. 29, no. 1, pp. 175–184, 2013.

[66] G. Bernardini, J. Serafini, S. Ianniello, and M. Gennaretti, "Assessment of computational models for the effect of aeroelasticity on bvi noise prediction," *International Journal of Aeroacoustics*, vol. 6, no. 3, pp. 199–222, 2007.

[67] M. Gennaretti, R. Gori, J. Serafini, F. Cardito, and G. Bernardini, "Identification of rotor wake inflow finite-state models for flight dynamics simulations," *CEAS Aeronautical Journal*, vol. 8, no. 1, pp. 209–230, 2017.

[68] M. Gennaretti, G. Bernardini, J. Serafini, and G. Romani, "Rotorcraft comprehensive code assessment for blade–vortex interaction conditions," *Aerospace Science and Technology*, vol. 80, pp. 232–246, 2018.

[69] L. Morino, "A General Theory of Unsteady Compressible Potential Aerodynamics," *NASA CR-2464*, Dicembre 1974.

[70] G. Bernardini, J. Serafini, M. M. Colella, and M. Gennaretti, "Analysis of a structural-aerodynamic fully-coupled formulation for aeroelastic response of rotorcraft," *Aerospace Science and Technology*, vol. 29, no. 1, pp. 175–184, 2013.

[71] L. Morino, "Boundary Integral Equations in Aerodynamics," *Applied Mechanics Reviews*, vol. 46, no. 8, pp. 445–466, 1993.

[72] M. Gennaretti, L. Luceri, and L. Morino, "A unified boundary integral methodology for aerodynamics and aeroacoustics of rotors," *Journal of Sound and Vibration*, vol. 200, no. 4, pp. 467–489, 1997.

[73] L. Morino and G. Bernardini, "Singularities in BIEs for the Laplace equation; Joukowski trailing-edge conjecture revisited," *Engineering analysis with boundary elements*, vol. 25, no. 9, pp. 805–818, 2001.

[74] W. R. M. Van Hoydonck, "Computation of rotorcraft wake geometry using nurbs," Master's thesis, Deft University of Technology, 2013.

[75] Y. Young and S. Kinnas, "Analysis of supercavitating and surface-piercing propeller flows via bem," *Computational Mechanics*, vol. 32, no. 4-6, pp. 269–280, 2003.

[76] S. A. Kinnas, W. B. Coney, *et al.*, "The generalized image model—an application to the design of ducted propellers," *Journal of Ship Research*, vol. 36, no. 03, pp. 197–209, 1992.

[77] W. Hooper, "The vibratory airloading of helicopter rotors," 1983.

[78] A. J. Landgrebe, "An analytical model for predicting rotor wake geometry," *Journal of American Helicopter Society*, vol. 14, no. 4, pp. 20–32, 1969.

[79] J. Serafini, F. Cardito, G. Bernardini, and M. Gennaretti, "Application of low-order wake inflow models to rotorcraft aeromechanics," in *International Forum on Aeroelasticity and Structural Dynamics*, (Como, Italy), June 2017.

[80] M. B. Tischler and R. K. Remple, *Aircraft and rotorcraft system identification*. 2006.

[81] P. C. Schulze, J. Miller, D. H. Klyde, C. D. Regan, and N. Alexandrov, "System identification of a small uas in support of handling qualities evaluations," in *AIAA Scitech 2019 Forum*, p. 0826, 2019.

[82] R. Gori, F. Pausilli, M. D. Pavel, and G. M, "State-space rotor aeroelastic modeling for real-time helicopter flight simulation," *Advanced Material Research*, vol. 1016, pp. 451–459, 2014.

[83] L. Ljung and R. Singh, "Version 8 of the matlab system identification toolbox," *IFAC Proceedings Volumes*, vol. 45, no. 16, pp. 1826–1831, 2012.

[84] H. Garnier and M. Mensler, "The contsid toolbox: a matlab toolbox for continuous-time system identification," *IFAC Proceedings Volumes*, vol. 33, no. 15, pp. 851–856, 2000.

[85] G. H. Gaonkar and D. A. Peters, "Effectiveness of current dynamic-inflow models in hover and forward flight," *Journal of the American Helicopter Society*, vol. 31, no. 2, pp. 47–57, 1986.

[86] M. Gennaretti, J. Serafini, P. Masarati, and G. Quaranta, "Effects of Biodynamic Feedthrough in Rotorcraft/Pilot Coupling: Collective Bounce Case," *Journal of Guidance, Control, and Dynamics*, vol. 36, no. 6, pp. 1709–1721, 2013.

[87] M. D. Pavel, M. Jump, B. Dang-Vu, P. Masarati, M. Gennaretti, A. Ionita, L. Zaichik, H. Smaili, G. Quaranta, D. Yilmaz, *et al.*, "Adverse rotorcraft pilot couplings—past, present and future challenges," *Progress in Aerospace Sciences*, vol. 62, pp. 1–51, 2013.

[88] M. D. Pavel, P. Masarati, M. Gennaretti, M. Jump, L. Zaichik, B. Dang-Vu, L. Lu, D. Yilmaz, G. Quaranta, A. Ionita, and Others, "Practices to identify and preclude adverse Aircraft-and-Rotorcraft-Pilot Couplings–A design perspective," *Progress in Aerospace Sciences*, vol. 76, pp. 55–89, 2015.

[89] F. Cardito, J. Serafini, C. Pasquali, G. Bernardini, M. Gennaretti, and R. Celi, "Finite-state wake inflow models for rotorcraft flight dynamics in ground effect," in *43rd European Rotorcraft Forum*, (Milan, Italy), September, 12-15 2017.

[90] L. Morino and B. Bharadvaj, "A unified approach for potential and viscous free-wake analysis of," in *12th European Rotorcraft Forum*, (Garmisch-Partenkirchen, Federal Republic of Germany), September, 22-25 1986.

[91] T. Theodorsen, "General theory of aerodynamic instability and the mechanism of flutter," Tech. Rep. Report 496, NACA, 1935.

[92] J. Boutet and G. Dimitriadis, "Unsteady lifting line theory using the wagner function for the aerodynamic and aeroelastic modeling of 3d wings," *Aerospace*, vol. 5, p. 92, 09 2018.